



Università degli Studi di Torino

Dipartimento di Scienze della Terra

Dottorato di Ricerca in Scienze della Terra – XXXIII Ciclo

**CALCAREOUS NANNOFOSSIL BIOEVENTS TO TRACE
AND DECIPHER THE MESSINIAN SALINITY CRISIS**

Candidate

Alan Maria Mancini

Tutor

Prof. Francesca Lozar

Co-tutor

Prof. Rocco Gennari

Prof. Francesco Dela Pierre

Coordinatore del corso di Dottorato

Prof. Anna Maria Ferrero

Anno accademico 2020-2021

Settore scientifico di appartenenza: GEO/01

SUMMARY

1- Introduction

1.1 Calcareous nannofossil as a tool for the paleoenvironmental reconstruction

1.2 The Messinian and its crisis

1.3 The Sorbas Basin

2 - Geological setting

2.1 Stratigraphic framework

2.2 Pre-MSC deposits in the Sorbas Basin

2.3 Studied section

2.3.1 Perales section

2.3.2 Los Molinos section

2.3.3 Rio de Aguas section

3 – Previous studies

3.1 Sorbas basin paleoecological response to orbital variability

3.2 The conceptual model for the deposition of the quadripartite cycle

4 – Aims

Chapter 1 – Calcareous nannofossil and foraminiferal trace element records in the Sorbas Basin: a new piece of the Messinian Salinity Crisis onset puzzle

Chapter 2 – Calcareous nannofossil size and abundance response to the Messinian Salinity Crisis onset and paleoenvironmental dynamics

Chapter 3 – Taphonomic bias and paleoenvironmental conditions across the first phase of the Messinian Salinity Crisis in the Sorbas Basin (SE Spain)

5- Future research and perspective

6- References

7- Acknowledgements

INTRODUCTION

1.1 Calcareous nannofossil as a tool for the paleoenvironmental reconstruction

Calcareous nannofossils (CN) are the remaining of calcifying marine algae (coccolithophores) and incertae sedis species producing small calcite platelets that are usually well preserved in the fossil record. The coccolithophores remains represent a powerful tool to document past environmental variability through the study of their assemblages (e.g.: Negri et al., 1999), their morphologic features (e.g.: Grelaud et al., 2012; Faucher et al., 2020), or the stable isotope/trace elements of their calcite (e.g.: Dedert et al., 2014; Bolton et al., 2016; Stoll et al., 2019). Sea temperature, salinity, nutrient content, light intensity, trace metals or carbonate chemistry (e.g. pCO₂) changes are proven to impact the coccolithophore assemblages, the size of their cells and their calcitic platelets across geologic time (Watabe and Wilbur, 1966; Paasche, 2002; Ziveri et al., 2004; Zondervan, 2007; Bollman and Herrle, 2007; Triantaphyllou et al., 2010; Beaufort et al., 2011; Triantaphyllou et al., 2018; Faucher et al., 2019). During the Messinian, strong paleoceanographic changes affected the Mediterranean basin culminating in the Messinian salinity crisis (MSC; see following chapter). Calcareous nannofossil were responsive to environmental change also during the Messinian, as supported by previous results showing CN abundance peaks approximating the MSC onset in several Mediterranean successions (Gennari et al., 2018; Lozar et al., 2018; Manzi et al., 2018; Lozar and Negri, 2019). This succession of CN peaks of abundance of the taxa *Sphenolithus abies*, followed or accompanied by *Helicosphaera carteri*, *Umbilicosphaera rotula* and *Rhabdosphaera clavigera* (Lozar et al., 2018; Lozar and Negri, 2019; Mancini et al., 2020) is described as the MSC onset bioevent. To decipher this peculiar CN signal is of paramount importance in order to constrain the paleoenvironmental perturbation that triggered the MSC onset.

1.2 The Messinian and its crisis

The Messinian is a geological stage characterized by rapid and extreme environmental changes affecting the whole Mediterranean region, mostly related to the ongoing restriction of the Atlantic

gateways (Flecker et al., 2015). The progressive restriction is suggested to be one of the main triggers of the onset of the MSC, which started synchronously in the whole Mediterranean at 5.97 Ma (Manzi et al., 2013). The ongoing restriction amplified the sedimentary and ecological response to orbitally induced climatic variation (Hilgen and Krijgsman, 1999). Several steps marking the paleoceanographic evolution before the MSC onset are recognised in the fossil record in many sections across the Mediterranean region (Seidenkrantz et al., 2000, Bellanca et al., 2001; Sierro et al., 2001; 2003; Blanc-Valleron et al., 2002; Kouwenhoven et al., 2003; Kouwenhoven et al., 2006; Iaccarino et al., 2008; Orszag-Sperber et al., 2009; Di Stefano et al., 2010; Gennari et al., 2018; Corbí et al., 2020). These major steps in the Mediterranean paleoceanographic evolution are dated at 7.19, 6.7, 6.4- 6.29, and 6.1-6.0 Ma (Kouwenhoven et al., 2006 and references therein). The second restriction at 6.7 Ma amplified the sensitivity of the Mediterranean basin to the precessional forcing, which drove the rhythmic deposition of sapropels at each insolation maximum (Sierro et al., 2003). These restriction steps were recently recognized in the Western Mediterranean (Bajo Segura Basin) and described as “start phase”, “amplification phase”, “consolidation phase” and “climax phase”, occurring at 6.72, 6.35, 6.03 and 5.97 Ma, respectively (Corbí et al., 2020). The climax phase at 5.97 coincides with the MSC onset; the crisis terminates at 5.33 Ma, in coincidence with the Messinian/Zanclean boundary (Roveri et al., 2014). The MSC event is characterised by three distinct stages, which were characterised by distinct deposits (for detail, see Roveri et al., 2014 and reference therein). Lithological cycles of the first stage of the MSC (5.97-5.60 Ma; Manzi et al., 2013) are characterized by shales or marls/sulphate evaporites or carbonates couplets (the Primary Lower Gypsum unit, PLG; Roveri et al., 2014); evaporites are only present in the marginal basin (DeLange and Krijgsman, 2010; Dela Pierre et al., 2011; Roveri et al., 2020), where up to 16 PLG cycles are recognized (Krijgsman et al., 2001; Lugli et al., 2010; Roveri et al., 2014; Roveri et al., 2020). Gypsum and carbonates are thought to reflect relatively more arid climate at precession maxima, whereas marls were deposited during more humid phase at precession minima (Krijgsman et al., 2001; Natalicchio et al., 2019). The increasing seawater salinity was thought to be responsible for both gypsum deposition and for the establishment of a biotic

crisis, with consequent disappearance of most eukaryote marine organisms from the fossil record (Blanc-Valleron et al., 2002; Rouchy and Caruso, 2006). Indeed, the MSC onset is approximated by the foraminifers and CN disappearance (Manzi et al., 2007), which was frequently assumed to be the result of hostile water column conditions related to an increase in water salinity (Blanc-Valleron et al., 2002; Rouchy and Caruso, 2006).

Successively, this view was challenged by the evidences that the gypsum of the PLG unit was deposited in a subaqueous setting up to 200m deep (Manzi et al., 2007; Lugli et al., 2010; Dela Pierre et al., 2014) and led to the review of the MSC scenario. This allowed to better explain the numerous occurrences of body (calcareous nannofossil, foraminifers, diatoms, fishes; Carnevale et al., 2019) and molecular fossils (Natalicchio et al., 2017; Sabino et al., 2020a) in the PLG unit. During the last decades, much attention was paid to the evaporitic deposits of the PLG unit, as they represent the most outstanding product of the MSC perturbation; on the contrary, the marl intercalations were overlooked in paleoenvironmental studies. These lithologies were addressed by relatively fewer studies, which investigated the microfossil (Van de Poel, 1992; Riding et al., 1998; Bertini et al., 1998; Goubert et al., 2001; Dela Pierre et al., 2014; Lozar et al., 2018; Manzi et al., 2007; Manzi et al., 2018), fish and other vertebrate (e.g. decapods, echinoids, bivalve and bryozoans; Landini and Sorbini, 1989; Vand de Poel, 1992; Montenat, 1990; Saint Martin et al., 2000; Lacour and Néraudeau, 2000; Néraudeau et al., 2002; Carnevale et al., 2008) and molecular fossil contents (Gelin et al., 1995; Kenig et al., 1995; Damstè et al., 1995; Vasiliev et al., 2017; Natalicchio et al., 2019; Isaji et al., 2019; Sabino et al., 2020a; Sabino et al., 2020b). The marly interbeds of the PLG unit or the shale and carbonate beds representing the deep water equivalent of the PLG unit are characterised by authigenic carbonate minerals like calcite, aragonite and dolomite, inferred to be the result of intense bacterial activity (Dela Pierre et al., 2012; Caruso et al., 2015; Natalicchio et al., 2017; Perri et al., 2017; Natalicchio et al., 2019; Sabino et al., 2020b). To date, the environmental and ecological dynamics occurred during the PLG deposition are far to be fully constrained. However, emerging evidence suggests that the surface waters were still inhabited by marine organism during the PLG

deposition, leaving open the question whether the calcifier disappearance was due to an environmental perturbation or a taphonomic bias or a combination of both. These evidence are:

1- In the shale hemicouplets of the PLG in the Piedmont Basin no calcite skeleton was recorded, either autochthonous or reworked. In contrast, only diatoms were recorded in both gypsum and shale (Fourtanier et al., 1991; Dela Pierre et al., 2015; Carnevale et al., 2019), indicating the presence of brackish to marine water conditions. Such condition could have promoted at least the CN proliferation.

2- In the Piedmont and Sicily basins CN and foraminifers disappearance is not a synchronous event (Violanti et al., 2013; Dela Pierre et al., 2014; Catalano et al., 2016; Lozar et al., 2018; Sabino et al., 2020a; Gennari et al., 2020)

3- fossil marine fishes were found in the shale of the PLG in the Piedmont Basin, Vena del Gesso Basin and Sorbas Basin (Sturani, 1967; Landini and Sorbini, 1989; Néraudeau et al., 2002; Carnevale et al., 2018). In some cases, these fossils were attributed to lagoonal taxa capable to thrive in brackish water (Carnevale et al., 2008; Carnevale et al., 2019).

4-The analysis of molecular fossils analysed in the shale hemicouplets of the Vena del Gesso Basin reveals the contribution of Haptophyte to the primary productivity (Kenig et al., 1995); 673 of the 762 described Haptophyte species are Coccolithophores. Organic by-products synthesized by Haptophyte (i.e. alkenones) were found both in the PLG and halite units (Vasiliev et al., 2017).

1.3 The Sorbas Basin

The Sorbas Basin represents one of the most intensively studied Messinian basins (Troelstra et al., 1980; Martín and Braga, 1994; Baggley, 2000; Fortuin et al., 2000; Sierro et al., 2001; Sierro et al., 2003; Pérez-Folgado et al., 2003; Filippelli et al., 2003; Flores et al., 2005; Braga et al., 2006; Rodríguez-Tovar et al., 2013; Clauzon et al., 2015; Modestu et al., 2017; Reghizzi et al., 2017; among

others). However, most of the high resolution micropaleontological studies focused only on the lower part of the Upper Abad Member (UA; from cycle UA5 to UA8, i.e. from ~6.6 Ma to ~6.55 Ma) with the long-term trend toward the MSC onset being documented with foraminiferal and isotopic (oxygen, carbon and strontium) datasets only (Sierro et al., 2003; Reghizzi et al., 2017). The Sorbas Basin offers the possibility to investigate the transition from the pre-evaporitic sediments to the PLG unit in great detail due to the high-resolution stratigraphic framework previously reconstructed for both intervals (Krijgsman et al., 1999; Sierro et al., 2001; Krijgsman et al., 2001; Manzi et al., 2013).

2 - Geological setting

2.1 Stratigraphic framework

The Sorbas Basin is a small and narrow Neogene Basin surrounded by elongated basement ridges forming the Sierra de Los Filabres, Sierra Alhamilla and Sierra Cabrera (fig. 1B). The Messinian stage in the Sorbas Basin is recorded by the Caños Formation, which is subdivided into four members: the Abad, Yesares, Sorbas and Zorreras Members (Ruegg, 1964; Volk, 1967). The Abad Member was deposited in the basin depocenter and records the Tortonian/Messinian boundary at its base (Sierro et al., 2001); toward the northern and southern basin margin the sediments of the Abad Mb. make transition to reefal limestones (Roveri et al. 2009). Based on the different lithologies, the Abad Member can be subdivided into two units showing a precessionally-driven cyclical stacking pattern: the Lower Abad (LA), characterised by the alternation of white and grey marls, and the Upper Abad (UA), characterized by the alternation of sapropel and diatomite layers sandwiched between white massive marls (Sierro et al., 2001; 2003). The Abad Member is overlain by the Yesares Member through a sharp but stratigraphically continuous boundary (Manzi et al., 2013; Mancini et al., 2020); although interpreted by some authors as an erosional surface (Braga et al., 2006; Bourillot et al., 2010). The Yesares Member corresponds to the local equivalent of the PLG unit (Roveri et al., 2014) and is characterized by up to 16 laminated marl and gypsum or carbonate couplets (Dronkert et al., 1976; Krijgsman et al., 2001; Lugli et al., 2010; Roveri et al., 2020), in which

the first cycle marks the MSC onset at 5.971 Ma (Manzi et al., 2013). A palaeodepth of ~ 150 - 240 m at the base of the Yesares gypsum has been estimated based on benthic foraminifera (BF) and considering the difference of elevation between the top of the last pre-MSC reef layer and the first gypsum bed (Dronkert, 1976; Troelstra et al., 1980; van de Poel, 1992; Riding et al., 1998; Baggley, 2000; Clauzon et al., 2015; Modestou et al., 2017). Oolite and microbialite dominated carbonate platforms, referred to as the Terminal Carbonate Complex (TCC, Fortuin and Krijgsman, 2003; Roveri et al., 2009; Clauzon et al., 2015), represent the shallow water marginal equivalent of the Yesares Member (Roveri et al., 2020). The transition between the Yesares and Sorbas members reflects a shallowing upward trend responsible for the establishment of coastal environments in large parts of the Sorbas basin (Krijgsman et al., 2001) and records the eastward progradation of deltaic and coastal wedges along the basin axis with lagoon and beach deposits at the top (Roep et al., 1998). The palaeodepth of the basin at the Yesares/Sorbas Member transition can be estimated at 75 to 100 m (Krijgsman et al., 2001; Roveri et al., 2020). The Sorbas Member underlies the continental deposits of the Zorreras Member, which consists of reddish silts and interbedded lacustrine limestones. Finally, the Zorreras Member records the Messinian/Zanclean boundary (Roveri et al., 2018).

2.2 Pre-MSC deposits in the Sorbas Basin

The Abad Member were deposited in the central part of the Sorbas Basin from the base of the Messinian and are overlain by the PLG of the Yesares Formation. The transition from the Abad Member to the PLG evaporitic sediments was interpreted as continuous by several authors (Krijgsman et al., 1999; Sierró et al., 2001; Roveri et al., 2009; Clauzon et al., 2015), while other authors suggest the presence of an erosional surface between the two units (Riding et al., 1998; Braga et al., 2006; Bourillot et al., 2009). Based on the different lithologies, the Abad Member can be subdivided into two units: the Lower Abad, which base is dated at 7.2 Ma and contains the Tortonian/Messinian boundary, and the Upper Abad, starting at 6.7 Ma (LA and UA units,

respectively; Sierro et al., 2001). Both units record the precessional signal, but differ in their lithological expression: the LA are characterized by an alternation of massive whitish marls and massive grey marls rich in planktic foraminifers (Sierro et al., 2001); the UA deposits are characterized by a quadripartite cycles (sapropel - marl – diatomite - marl). As outlined by Sierro et al. (2001), exceptions to this rule, such as thickness of the sapropelitic interval or presence/absence of the diatomite, coincide with peculiar orbital curve configurations, corresponding to eccentricity minima or precession/obliquity interference giving rise to low or high insolation amplitude. The sapropels in the Sorbas Basin are sandwiched between homogeneous white marl beds and consist of brownish laminated marls, sometimes with upward graded silty to sandy layers, interpreted as thin turbidite bed intercalations (Sierro et al., 2003). Generally, the lamination is well developed in the upper part of the sapropels, whereas it is weakly developed in the lower parts, where bioturbation is slightly more intense (Sierro et al., 2001; Flores et al., 2005). The diatomites are white, usually laminated and with a high abundance of diatom frustules.

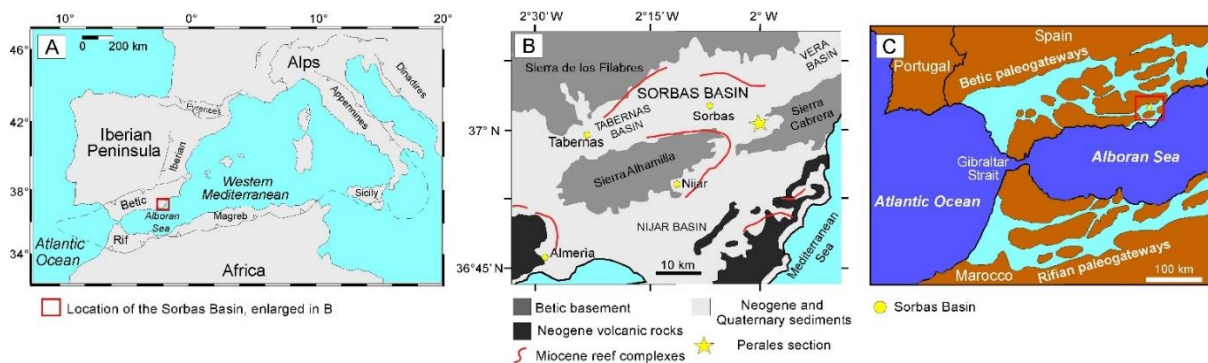


Fig. 1: A: Location of the Sorbas Basin in the western Mediterranean Sea (Modified from Corbi and Soria, 2016). B: Geological map of South-East Spain showing the Sorbas Basin and the Perales section (modified from Cuevas Castell et al., 2007 and Bourillot et al., 2009). C: Sorbas Basin paleogeography in the context of the Betic and Rifian paleogateways (marked in light blue). The Sorbas Basin configuration spans approximately from 8 to 6 Ma (modified from Modestou et al., 2017).

2.3 Studied section

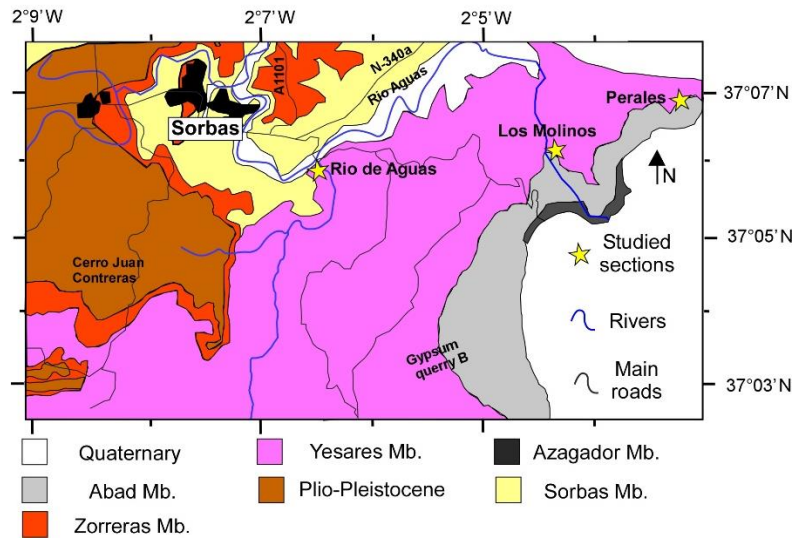


Fig. 2: Enlargement of the Sorbas Basin with the outcropping Messinian Member and the location of the studied sections (modified from Roveri et al., 2020)

2.3.1 Peralas section

The Peralas section (37° 05' 49" N 2° 03' 19" W) records the complete succession of events from the base of the Messinian (Sierro et al., 2001) to the firsts 2 PLG beds (Yesares Member, Manzi et al., 2013). The Peralas C subsection of Sierro et al. (2001) was re-sampled from UA23 to PLG2 obtaining 135 samples, including the transitional interval detailed in Sierro et al. (2001, 2003) and reinterpreted in Manzi et al. (2013). Regarding the UA cycles, some subtle differences emerged during the field work, like the occurrence of poorly laminated sapropel (Fig. 3). Taking advantage of the very good outcrop condition, we were able to produce a detailed log of the transitional interval ("transition to the gypsum interval" in Sierro et al., 2003; upper UA34 cycle in Manzi et al., 2013), which introduces new and important features which are detailed in Section 2.3.

A substantial deviation from the "regular" quadripartite cycle is represented by the cycle UA34, which, from bottom to top, is composed of sapropel – siliceous spiculite – from weak to well laminated sapropel – limestone – from weak to well laminated sapropel – limestone – clay

(Fig. 3). This deviation is different from the usual variance recorded in older UA cycles, which are explained by variation in orbital configuration (Sierro et al., 2001). The lack of the diatomitic

layer and the weak differences, in terms of colour and lamination, between sapropel and marls compared to the underlying cycles, complicate the recognition of the precessional forcing. The clay at the top of cycle UA34 is located just below the base of the poorly laminated to laminated sapropel below the base of the first gypsum layer. In line with previous interpretations (Manzi et al., 2013), our field observations confirm that the irregular surface corresponding to the UA/PLG transition is not indicative of an erosional unconformity, but due to the irregular lateral lithologic transitions that characterizes cycle PLG1, characterized by a limestone bed which laterally grades to variable thick gypsum deposits.

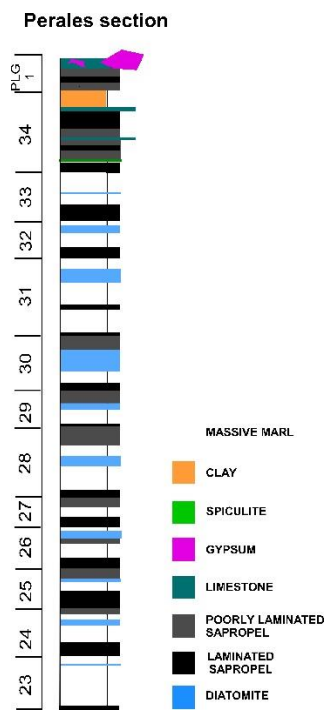


Fig. 3: Stratigraphic column of the Perales section from cycle UA23 to PLG1

2.3.2 Los Molinos section

The Los Molinos section (37° 5' 53" N 2° 4' 39" W) is located to the North of the Los Molinos de Rio Aguas village (La Casita; Fig. 2) along a canyon cut into the gypsum beds of the Yesares Member, that are composed by different gypsum facies, (i.e. massive selenite, banded and branching selenite; Lugli et al., 2010). The thickness of the gypsum beds of the Yesares Member decreases upward, as observed in the PLG unit of other Mediterranean sub-basins (Lugli et al. 2010).

The section starts from the second gypsum cycle of the PLG unit but the total numbers of cycles is controversial, ranging from 13 (Dronkert et al., 1976), 15 (Krijgsman et al., 2001) or 16 (Roveri et al., 2009). The inconsistency raises from the different interpretation of the upper part of the section, in which the recognition of the lithological cyclicity is not straightforward. This holds true in particular for cycle PLG 11, where the laminated marls are replaced by micritic limestone with unusual thickness (5 meters) compared to the other marly PLG hemicycles (1.5 – 2 meters on average) (Fig.2). Krijgsman et al. (2001) subdivided such thick micritic limestone interval into 3 precessional cycles; Roveri et al. (2009) confirmed this interpretation on the basis on the presence of discontinuous gypsum layers within the micritic limestone interval. Since we did not recognise either any significant lithological, colour pattern or gypsum layers in the micritic limestone interval, we considered this interval as representing a single lithological hemicycle. The counting of the PLG cycles in the upper part of the section was also hampered by the increasing vegetation coverage and by the thinning of the gypsum beds, often present as isolated outcropping blocks. In this section we collected 66 samples in the marl/limestone hemicycles. Unfortunately, we were not able to sample cycle PLG10 because the outcrop was not accessible.

2.3.3 Rio Aguas section

The Rio Aguas section is located S-W of the Sorbas village (37° 5' 25'' N 2° 6' 50'' W); according to Krijgsman et al. (2001) it starts from cycle PLG2 and continues up to the Yesares/Sorbas member transition. In the upper PLG cycles the recognition of the lithological cyclicity was hampered due to gypsum transition to limestones of the Hueli member, representing the marginal equivalent of the Yesares member (Roveri et al., 2020). A total of 14 samples were collected in the marly interval of PLG7 and PLG8.

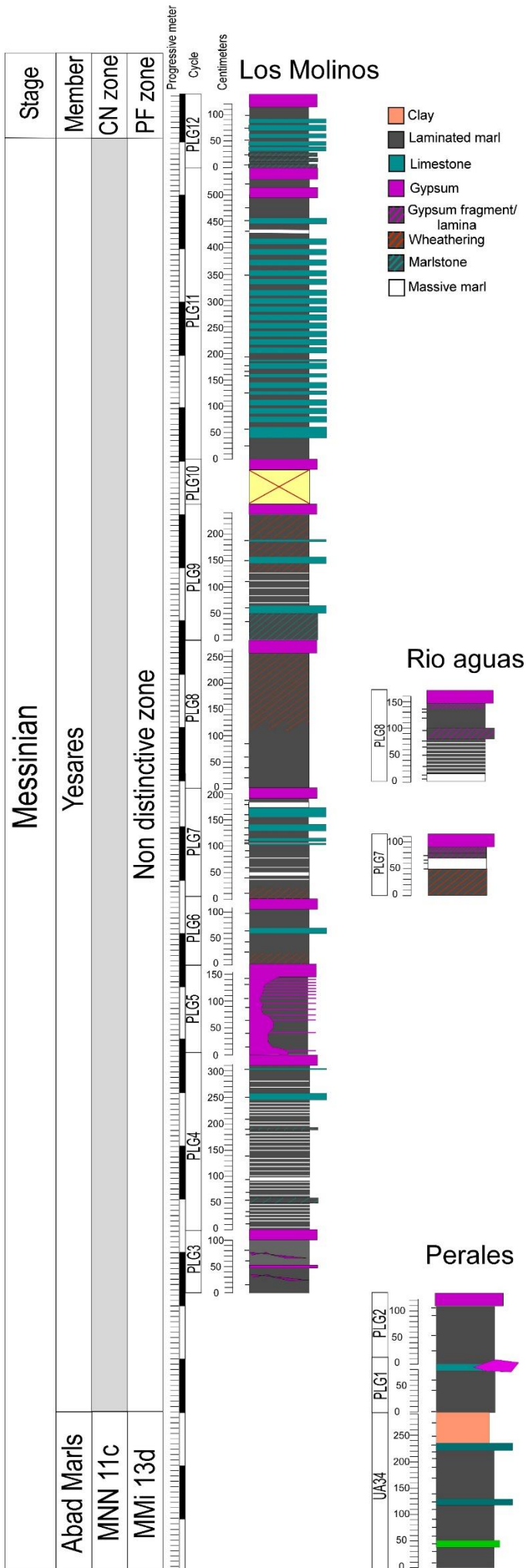


Fig. 4: Stratigraphic column of the studied sections. The cycle PLG10 was not sampled and measured. Gypsum layers are not to scale.

3 - PREVIOUS STUDIES

3.1 Sorbas basin paleoecological response to orbital variability

The LA to UA transition took place between 6.7 and 6.8 Ma and was driven by strong environmental changes, reflected in the lithology (onset of the sapropel and diatomite deposition), Oxygen and Carbon isotope record and in the foraminifer assemblages (Sierro et al., 2003). These changes are commonly related to a severe reduction of the Atlantic-Mediterranean water exchange (Sierro et al., 2003). Similar coeval changes were observed in Cyprus (Pissouri section; Kouwenhoven et al., 2006). The progressive restriction recorded in the UA prior to the MSC onset is recognizable in the higher amplitude of the precessional variability observed in the planktic/benthic and warm-oligotrophic/cold-eutrophic foraminifer (Sierro et al., 2003). From cycle UA8 upward the benthic foraminifers increase and reach their maximum abundance between UA21 and UA31 (Sierro et al., 2003). From UA16 to the top of the UA member, the planktic/benthic ratio ranges between 0% in the upper marls to 100% within the sapropel. Species such as *Globigerinoides obliquus*, *G. sacculifer* and *O. universa* show very typical cyclical patterns in the UA, reaching the maximum abundance in the middle upper part of the sapropels, or at the transition between the sapropel and the lower marls. The cyclical patterns observed in *Globigerina bulloides* and the group of Neogloboquadrinids are opposite to those seen in *Globigerinoides* and *O. universa*. In the UA the Neogloboquadrinids generally start to be present in the middle upper part of the sapropels, becoming abundant in the homogeneous marl above the sapropel, although in some intervals they remain abundant throughout the marls and the diatomites (Sierro et al 2003; Pèrez-Folgado et al., 2003). The small-sized planktic foraminifera, including both species of *Turborotalita* and *Globigerinita glutinata* are usually rare in the Lower Abad but occasionally dominate close to the upper marl-sapropel transitions in the Upper Abad (Sierro et al., 2003). However, from UA31 upward, only the

warm/oligotrophic *O. universa* and the cold/eutrophic *Turborotalita*, Neogloboquadrinids and *G. bulloides* are recorded (Sierro et al., 2003), complicating the recognition of a cyclic precessional pattern and of the environmental changes characterizing the last pre evaporitic phase. To decipher the environmental changes that took place just prior the MSC onset is further complicated by the lack of information regarding the foraminifer assemblage in cycle UA34.

3.2 The conceptual model for the deposition of the quadripartite cycle

The conceptual model of the quadripartite cycle is built on high resolution studies on four cycles of the lower part of the UA (UA5 to UA8) (Perez-Folgado et al., 2003; Vazquez et al., 2003; Filippelli et al., 2003; Flores et al., 2005; Modestu et al., 2017). This model describes the main paleoenvironmental dynamics driven by precessional cyclicity, and it divides the basic cycle into 4 stage characterized by distinct microfossil, geochemical and isotope signature: middle/upper sapropel - lower marl - diatomite - upper marls/lower sapropel.

1. Middle/upper sapropel

The middle/upper part of the sapropels is characterized by the dominance of warm-oligotrophic foraminifera, low benthic foraminifera abundance and the low $\delta^{18}\text{O}$ values measured on *O. universa* shells. These signatures were interpreted as a high freshwater input into the basin indicating the formation of a strong and permanent pycnocline at depth with the subsequent stratification of surface waters and anoxic condition at the bottom (Sierro et al., 2003; Pèrez-Folgado et al., 2003). The permanent pycnocline favours the formation of a deep nutricline as confirmed by the presence of inferred deep photic zone taxa, such as *Discoaster* sp and *Sphenolithus abies* (Flores et al., 2005).

2. Lower marl

In this layer the Neogloboquadrinids start to partially replace the warm/oligotrophic foraminifer, the benthic community increases in abundance and *O.universa* $\delta^{18}\text{O}$ increases (Sierro et

al., 2003; Pèrez-Folgado et al., 2003), whereas the CN assemblage is dominated by small *Reticulofenestra* (< 5 µm; Flores et al., 2005). All these features were interpreted as a temperature decrease that led to a more mixed water column in the cooler months, and a shoaling of the DCM concomitant with more oxygenated conditions at the sea floor (Flores et al., 2005).

3. Diatomite

In this layer, the Neogloboquadrinids were replaced by *G. bulloides* (i.e. from UA5 to UA14) or *Turborotalita quinqueloba*-*T. multiloba* (i.e. from UA14 to 16 and from UA20 to 28), benthic foraminifera and siliceous microfossils were abundant (Pèrez-Folgado et al., 2003). Heavier *O.universa* $\delta^{18}\text{O}$ values correlate with the dominance of the CN *Reticulofenestra* > 5 µm, *C. pelagicus* and *H. carteri* (Flores et al., 2005). All these features indicated a further temperature decrease, leading to a more mixed water column (upwelling regime) that promoted high productivity throughout the photic zone and oxygenated sea floor (Sierro et al., 2003; Pèrez-Folgado et al., 2003; Flores et al., 2005).

4. Upper marls/lower sapropel

During this stage *G. bulloides* is again the dominant species in some cycles together with *T. quinqueloba*-*T. multiloba*; the benthic foraminifer remains abundant. However, during the upper marl/lower sapropel transition a sudden drop in the planktic foraminifer abundance and diversity is recorded (Sierro et al., 2003). This trend is exacerbated especially from UA17 upward, where the samples are completely devoid of planktonic foraminifera (Sierro et al., 2003). From cycle UA23 upward, the upper marl/sapropel transition is also characterized by highest abundances of the benthic community (Sierro et al., 2003). The $\delta^{18}\text{O}$ values start to decrease in the upper marls, reaching their minimum values in the middle/upper sapropel (Pèrez-Folgado et al., 2003) and the CN assemblage is dominated by *Umbilicosphaera jafari* (Flores et al., 2005). During insolation minima the climate in the Sorbas Basin was probably dry leading to the formation of salty and dense water

that sunk to the bottom (Sierra et al., 2003). After the insolation minima, the continental run-off started to increase, further increasing the density stratification between the light/less saline surface water and the heavy/salty water at the bottom (Sierra et al., 2003). The pumping of these high density waters over the basin sill promoted the stagnation of the deep water in the deeper part of the basin (Sierra et al., 2003). The progressively reduced bottom water ventilation together with the relatively high productivity triggered the formation of sapropelitic sediments in broad areas of the basin (Sierra et al., 2003). Sierra et al. (2003) speculate that the rising of the bottom stagnant water during seasonal pulse of deep convection may have supplied highly eutrophic, relatively toxic waters to the photic zone that were responsible for the low diversity and scarcity/absence of planktonic foraminifera.

4- Aims

This thesis aims to track the environmental changes spanning the uppermost pre-MSC and the first stage of the MSC (from 6.23 to 5.33 Ma) in the Sorbas Basin. Specifically, this thesis will be focus on:

- (i) The eventual presence of the previously widely recorded CN bioevent, which could highlight specific environmental changes that occurred at the Mediterranean Basin scale.
- (ii) The cyclical precession-driven environmental change and its repercussion on the marine biota.
- (iii) The evolution of the paleoenvironmental dynamics toward and during the MSC.
- (iii) The causes that led to the CN disappearance approximately at the MSC onset; where they related to an increase in salinity of the water column?

In order to address these points, I analysed CN relative and absolute abundance and I analysed morphometric parameters (e.g. size, eccentricity, mass, calcification index) on selected CN taxa. Additional micropaleontological analyses were conducted exploring the benthic and planktic

foraminifer content, along with the trace element analyses performed on foraminiferal test.

Petrographic, mineralogical and isotopic composition were also performed on selected samples.

CHAPTER 1 - Calcareous nannofossil and foraminiferal trace element records in the Sorbas Basin: a new piece of the Messinian Salinity Crisis onset puzzle*

The Messinian Salinity Crisis (MSC) was an extreme event that affected the Mediterranean Sea during the late Miocene, leading to massive evaporite deposition across the basin. Here we focus on the Perales section (Sorbas Basin, Western Mediterranean), using calcareous nannofossil (CN) and foraminiferal geochemical analyses to trace the paleoenvironmental dynamics culminating in the MSC onset.

Orbital and tectonic forcing drove the CN fluctuations that correlate with the lithological quadripartite precessional cycle. Our integrated analysis reveals that cyclical sapropel deposition was

triggered by an increase in marine productivity, followed by an increase in freshwater input and the development of a Deep Chlorophyll Maximum (DCM). The overlying marl records the protracted freshwater input that led to the shallowing of the DCM, decreasing organic carbon export and promoting seafloor re-oxygenation. Stratification, acting as a barrier, trapped part of the river-sourced nutrients below the photic zone. The subsequent gradual decrease in temperature promoted the disruption of the stratification, mixing nutrients upward into the photic zone, and diatom proliferation and preservation. When the reservoir of dissolved silica was exhausted, bioturbated marls were deposited at the top of the cycle.

In the last pre-evaporitic cycle (UA34) the usual lithological cyclicity is obliterated; however the precessional footprint is revealed by CN fluctuations, suggesting that sapropel-like deposition lasted for most of the cycle. This cycle also records a succession of CN abundance peaks (MSC onset bioevent), as already recorded in several Mediterranean sections approximately at the MSC onset, suggesting that the same paleoenvironmental changes triggered the evaporitic phase in the whole Mediterranean. This bioevent marks the last step of water exchange reduction with the Atlantic (restriction pulse), which increased the sensitivity of the Mediterranean to freshwater input and associated nutrient delivery, culminating in a further increase in marine productivity.

* This chapter is based on Mancini, A. M., Gennari, R., Ziveri, P., Mortyn, P. G., Stolwijk, D. J. Lozar, F., 2020. Calcareous nannofossil and foraminiferal trace element records in the Sorbas Basin: A new piece of the Messinian Salinity Crisis onset puzzle. *Palaeogeography, Palaeoclimatology, Palaeoecology*, 554, 109796

2. Materials and methods

2.1 Calcareous nannofossil analysis

Standard smear-slides were prepared for each collected sample from UA23 to UA34 and observed at 1250X by polarized light microscopy. In each slide at least 500 specimens were counted and identified. The CN preservation ranges from poor to good; overall cycles UA29 and UA30 are

characterized by poor CN preservation. The samples affected by poor CN preservation are characterized by dissolution features, etching and/or overgrowth on the CN. The rare and the extremely rare species without known paleoecological significance are not shown in the figures. *Reticulofenestra pseudumbilicus* < 7 µm and > 7 µm, *Calcidiscus leptoporus* < 7 µm and >7 µm, *Pontosphaera multipora*, *Pontosphaera japonica*, *Discoaster variabilis*, *Discoaster brouweri*, *Discoaster pentaradiatus*, *Sphenolithus abies* and *Sphenolithus moriformis* are included in the informal groups of *R. pseudumbilicus* gr., *C. leptoporus* gr., *Pontosphaera* gr., *Discoaster* gr. and *Sphenolithus* gr., respectively. The informal group *Sphenolithus* gr. mainly comprises *S. abies*, whereas *S. moriformis* has a scattered occurrence and shows considerable abundance only in a few intervals. The presence/absence of diatoms in the CN counting phase was performed as well. Scanning electronic microscopy (SEM) analyses were performed on selected samples of the cycle UA34 using a JSM-IT300LV SEM equipped with an energy-dispersive EDS Oxford Instrument Link System microprobe (Department of Earth Sciences, University of Torino).

2.2 Foraminiferal analysis

In order to correlate our log with the Abad composite section published in Sierro et al. (2001), the presence of left coiled *Neogloboquadrina acostaensis* and of *Turborotalita multiloba*, which are age diagnostic species for the studied interval, were observed in some selected samples (20 samples from UA25 to UA31). About 100 grams of sample, previously dried, were soaked in diluted H₂O₂ for one day; successively the sediment was washed using a 63 µm sieve, oven-dried, and dry-sieved to obtain 3 different size fractions: >500 µm, 500-125 µm and 125-63 µm. Qualitative observations were carried out on the > 125 µm residues (the results are summarized in Fig. 1). A qualitative analysis (presence/absence) of planktic and benthic foraminifers was performed as well in the cycle UA34, which was not the object of previous studies.

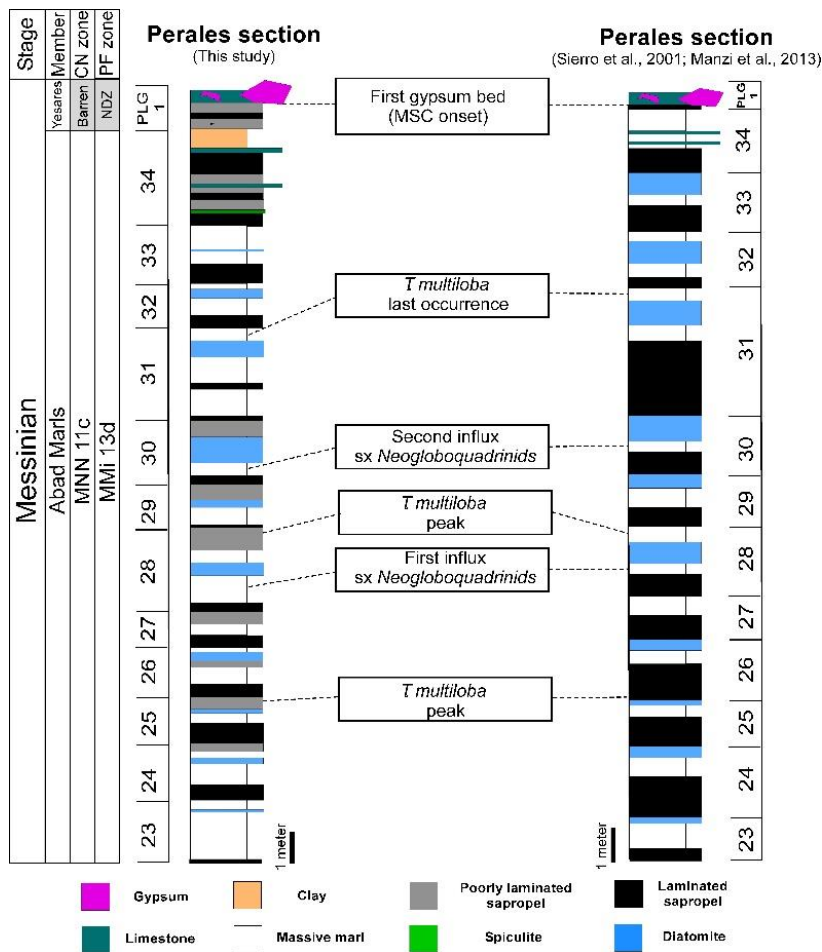


Fig. 1: Correlation with the Perales section achieved by Sierro et al. (2001) modified after Manzi et al. (2013). Foraminifer bioevent (Sierro et al., 2001) and the first gypsum bed (Manzi et al., 2013) are used as tie points. The *Turborotalita multiloba* last peak and the second influx of *Neogloboquadrina acostaensis* (sinistral coiling) are recorded in the upper and lower marl of the UA31 and UA30, respectively. These calcareous plankton events are synchronous throughout the Mediterranean (Sierro et al., 2001). Using these bioevents according to Sierro et al. (2001) and the recognition of the PLG1 layer, according to Manzi et al. (2013) it was possible to achieve the correlation with the Abad composite section proposed by Sierro et al. (2001). The CN and the planktic foraminifer (PF zone) zones were established according to Raffi et al., 2003 and Lirer et al., 2019.

2.3 *Orbulina universa* trace element analysis: a new picking protocol

Trace element analysis was performed on 31 samples taken throughout the studied interval (2-3 samples each cycle). A major challenge of the foraminiferal trace element analyses was the poor preservation of the *O. universa* calcite shells, often filled with diagenetic calcite (Fig.2 D, E and F). This diagenetic calcite overprint could potentially bias the overall trace element signals inherent to the

biogenic calcite of the foraminifer shells. To avoid this contamination, we focused only on well-preserved *O. universa*, using a new picking technique as follows:

- Wash the sediment in a sieve (we used the 63 μm) using ELIX water (this water is to be preferred because it prevents the precipitation of carbonate crystals) sprayed with a pump.

- When the fine fraction is washed away, oven-dry the sample (70 C°).

- Sieve the sediment of the target size range (the one we aim to measure). In this work, we focused on the foraminifer size between 315 and 355 μm . Take the target size fraction and put it in a beaker previously filled with ELIX water. Let the heavier foraminifers (filled or encrusted by secondary calcite) rapidly sink.

- Aspirate the floating shells with a pipette. This allows capturing the lighter shells that are likely devoid of diagenetic calcite or sediment infill.

- Put the captured foraminifers into a saucer and proceed to picking while the foraminifers are still wet. This procedure improves the possibility to pick pristine shells, since wet foraminifers (especially *O. universa*) better show their transparency, and more transparent tests are usually devoid of secondary calcite.

We further tested the reliability of this method by checking SEM pictures of both the heavier/sinking *O. universa* (Fig.2 D, E, F) and the lighter/floating ones (Fig.2 A, B, C). The test indicates that our methodology assures to capture the best-preserved *O. universa* specimens.

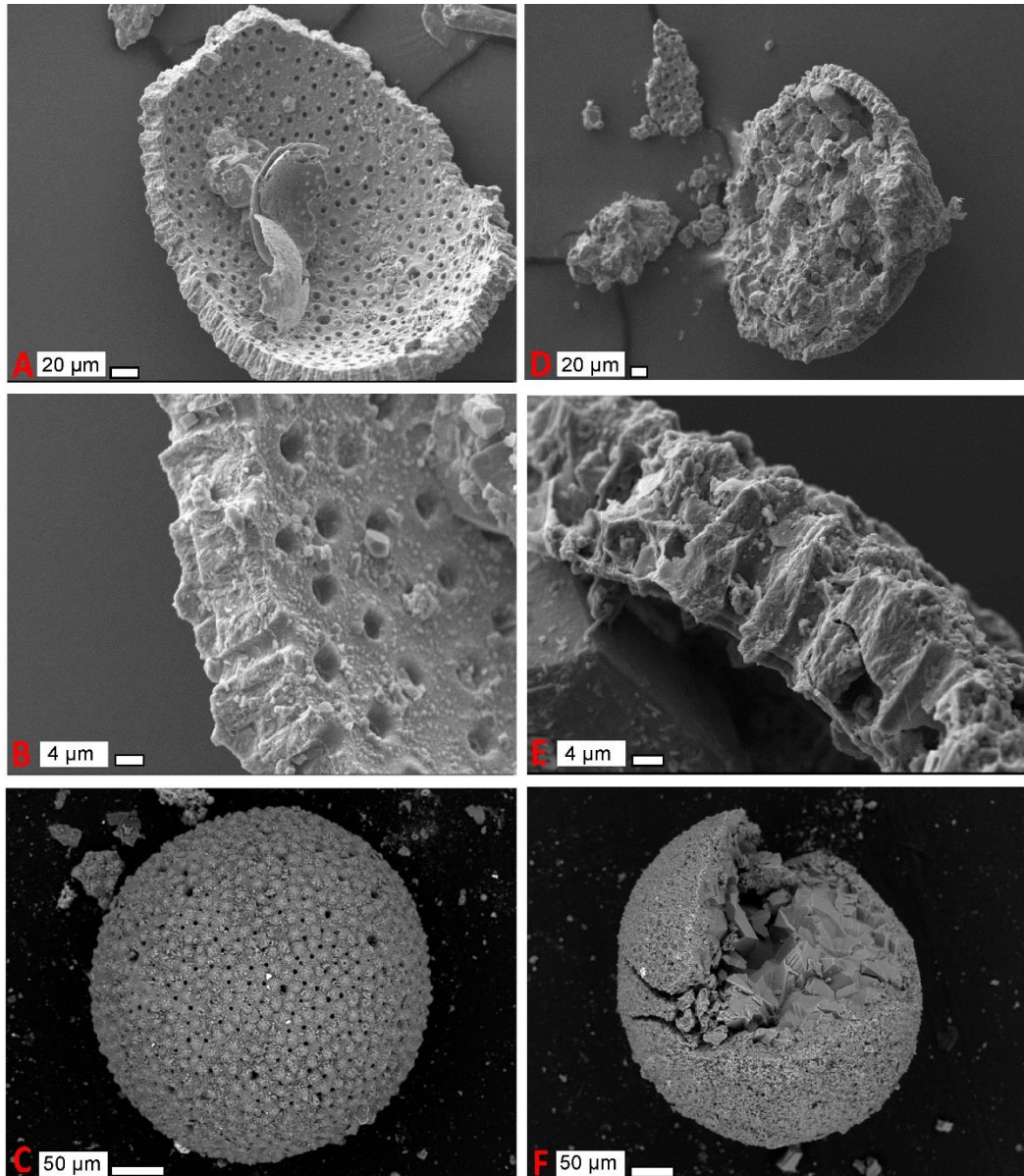


Fig. 2: SEM images of the foraminiferal species *O. universa* with different degrees of preservation.

(A-B-C): Floating *O. universa* (see 3.4) before the cleaning process, showing good preservation. The internal and external wall are affected by minor diagenetic secondary calcite and coccolith biogenic calcite. Reghizzi et al. 2017 show the effectiveness of the weak acid leach step in removing these kinds of foulings. (D E-F): Sinking *O. universa* (see 3.4) showing bad preservation. The foraminifer is completely filled with secondary diagenetic calcite.

2.4 *Orbulina universa* trace element analyses

The investigated samples were composed of a minimum of 100 μg of shell calcite of *O. universa* picked from sapropel and lower marls. In most cases, the well-preserved *O. universa* picked did not

provide the calcite weight needed for the analysis (100-150 µg of calcite); this restricted our analysis to only 14 samples in the UA23-base UA30 interval and in the transition from UA32 to UA33. The samples were cleaned according to the “Cd method” described by Rosenthal et al., 2004. The method consists of several steps: clay removal washes (water and methanol), a reductive step (ammonium hydroxide, citric acid and hydrazine hydrate), an oxidative step (sodium hydroxide and hydrogen peroxide), and finally a weak acid leach (nitric acid). The samples were analysed with an inductively coupled plasma mass spectrometer (ICP-MS, Agilent model 7500ce) at the Autonomous University of Barcelona. The procedure of data reduction followed that previously established by Yu et al., 2005.

According to the premise that the seawater temperature is the primary control on Mg²⁺ incorporation in the foraminiferal calcite shell during the calcification process, the Mg/Ca analysis is often used as a T proxy (Lea et al., 1999; Elderfield and Ganssen, 2000; Erez, 2003; Barker et al., 2005). The obtained Mg/Ca values were converted into temperature values according to Anand et al., (2003) using the equation:

$$\text{Mg/Ca} = B \exp(AT) \quad (1)$$

where Mg/Ca is the measured value from the calcite shell, A and B are constant coefficients (corrected for *O. universa* according to Anand et al., 2003 “Table 3”) and T is the calcification temperature.

Early studies reported that foraminifers can sequester barium and other elements in proportion to their concentration in the surrounding seawater (Boyle and Keigwin, 1985; Lea and Boyle, 1991). Consequently, the trace element studies are considered reliable proxies for ocean elements reconstruction in the past. Apart from hydrothermal vents, the major source of barium to the ocean is fluvial discharge (Martín and Meybeck, 1979). Moreover, the input of fluvial barium increases in the river-sea mixing zone as barium desorbs from the suspended load by ion exchange (e.g. Hanor and Chan, 1977). For these reasons, high levels of barium in surface seawater track continental inputs; consequently the measured Ba/Ca on foraminiferal shell is used here as a continental run-off proxy.

3. Results

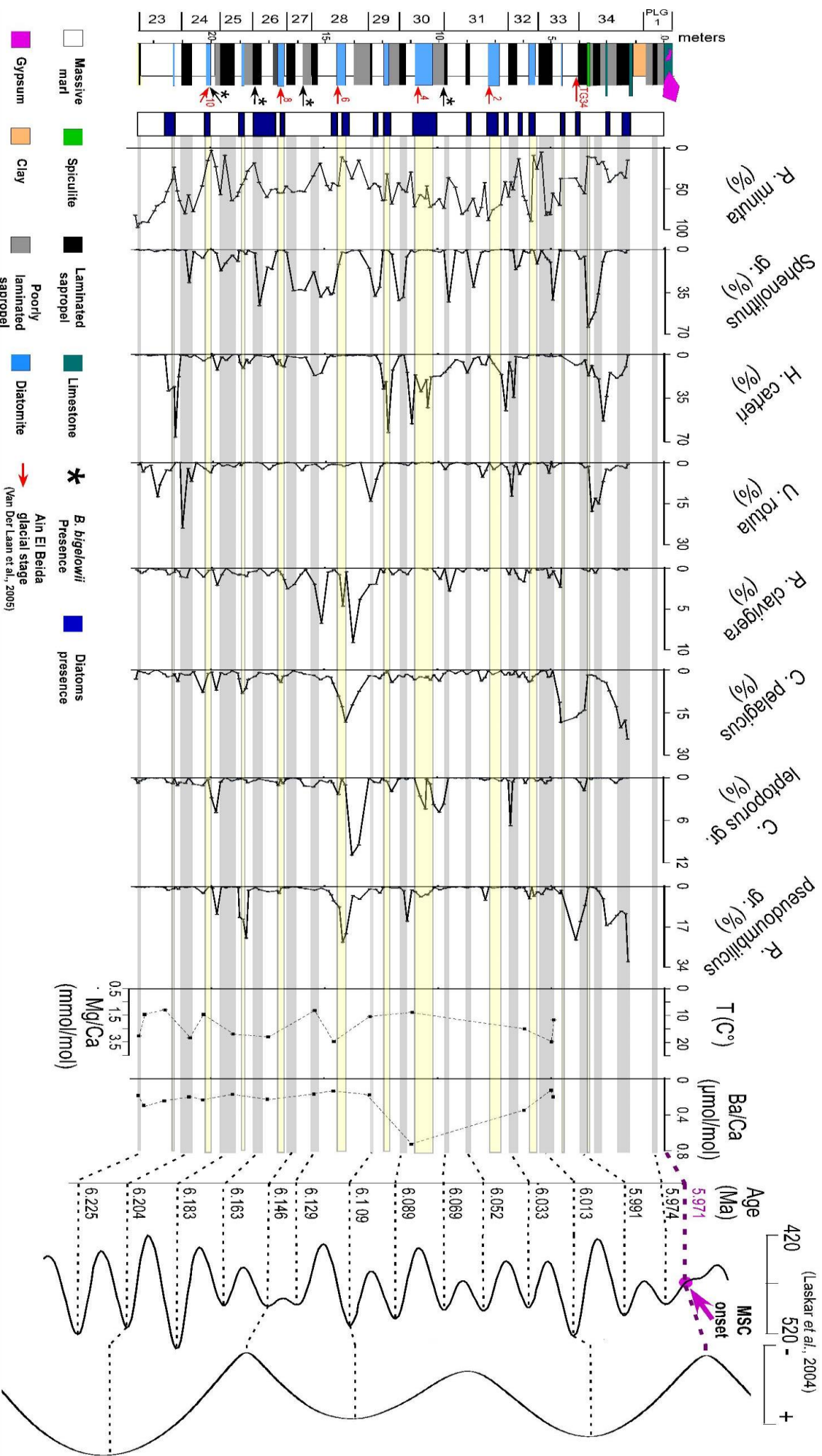
3.1 Calcareous nannofossil relative abundance

The CN assemblage is composed of 28 taxa (appendix). CN are present throughout the studied interval, except in all the samples collected above the second limestone layer of cycle UA34. The composition of CN assemblages is cyclical and quite regularly follows the lithological cyclicity (Fig 4.1 and 4.2). CN assemblages are generally dominated by *Reticulofenestra minuta*, which is present in all samples and commonly reaches up to 60% of the total assemblage. *R. minuta* usually shows minimum abundance in the diatomite, where it is often replaced by *R. pseudoumbilicus* sp. and *Reticulofenestra haqii*. *Sphenolithus* gr. show abundance peaks in the middle-upper part of the sapropel (ca. 30%) and an abundance maximum at 62% in the spiculite layer of the cycle UA34. Conversely, *Sphenolithus* gr. minimum abundance is recorded in the diatomite layer. *Sphenolithus* gr. also show a positive correlation with the temperature inferred from the Mg/Ca analysis (Fig. 3.1). *Helicosphaera carteri* occurrence is scattered but shows prominent peaks in abundance (more than 30%) generally associated to the diatomite layer. High *H. carteri* abundance (55%) is found concurrently with a prominent Ba/Ca peak in the lower marls of the cycle UA30 (Fig. 3.1). *Coccolithus pelagicus* and *R. pseudoumbilicus* gr. show a similar trend, with abundance peaks close to the diatomite and a progressive increase at the top of UA34. *C. leptoporus* gr. is mainly composed of a large morphotype (according to Quinn et al., 2004); its higher abundances are generally found in the upper marls. *Umbilicosphaera rotula* abundance never exceeds 24% of the total assemblage and shows peaks preferentially in the upper marl-sapropel transitions. The most prominent *U. rotula* peaks (24% at the base of the sapropel in UA24; 17% and 15% in the poorly/well laminated sapropels of the cycle UA34) coincide with the maximum abundance of benthic foraminifers recorded by Sierro et al., 2003 and in our material (Figs. 4, 5 and 6). *Rhabdosphaera clavigera* abundance is generally low and never exceeds 4.5%, aside from the cycle UA28 where three different peaks are recorded (from 4.5% to 9%), occurring together with *C. leptoporus* gr. and *C. pelagicus* peaks. From cycle UA28 *R. clavigera* shows a decreasing trend toward the top of the section. *Reticulofenestra haqii* abundance is scattered and

apparently does not correlate with the lithology. In cycles UA32 and UA33 the higher *R. haqii* abundance is recorded in few samples (from 40% to 88%). Similar to *R. haqii*, *Reticulofenestra antarctica* abundance is generally low, but shows a prominent peak (and other minor peak) in cycles UA32 and UA33. *Umbilicosphaera jafari* abundance is generally low but occurs in high abundance in some discrete intervals (from UA23 to UA25 and from UA31 to UA33), exceptionally reaching 87% of the assemblage in the upper marl of the UA24. *Pontosphaera* gr. is regularly present in moderate abundance generally in the diatomite up to cycle UA31, where it starts to decrease. *Syracosphaera* sp. 1 is preferentially present close to or in the diatomite, with an abundance that never exceeds 22% (cycle UA28) and generally is below 5%. The abundance of *Discoaster* gr. is scattered but shows prominent peaks, recorded preferentially in the upper marl, up to cycle UA28; it becomes rare above this level. Intriguingly, *Discoaster* gr. are present in some levels (lower marls of the cycles UA23, UA24, UA26 and in the sapropel of the cycle UA31) with moderate abundance; their poor preservation and strong recrystallization hinders the identification at the species level and consequently the discrimination between syndepositional and reworked specimens. This probably results in an underestimation of the *Discoaster* gr. abundance, especially in the upper part of the section. *Thoracosphaera heimii* shows a scattered abundance, with a maximum in abundance in UA34 (1,4%).

The relationship between the CN assemblage and the lithological cyclicity changes in cycle UA34, where a sequence of abundance peaks of peculiar species is recorded (Fig. 3.1), as previously reported in other sections approximating the MSC onset (Lozar et al., 2018; Lozar & Negri, 2019). The succession of peaks in abundance is composed of: *S. abies*, followed by *U. rotula*, *H. carteri*. *Sphenolithus abies* (during the MSC onset bioevent the informal *Sphenolithus* gr. is composed entirely of *S. abies*) peaks (62%) in the spiculite layer; *U. rotula* shows 2 peaks (17% and 15%) recorded in poorly laminated sapropel and in a laminated sapropel immediately above the *S. abies* peak. *H. carteri* gradually increases at the base of UA34 and peaks (33%) in a poorly laminated sapropel above the *U. rotula* peak. Above the MSC onset bioevent, *C. pelagicus* and *R. pseudoumbilicus* gr. increase up to the second limestone of the UA34 cycle, where suddenly all CN disappear.

Summer insolation 65°N (W/m²),
Eccentricity index
(Laskar et al., 2004)



420 520 +

MSC onset

Age (Ma)

5.974

5.974

5.991

6.013

6.033

6.052

6.089

6.089

6.109

6.129

6.146

6.163

6.183

6.204

6.225

6.225

6.225

6.225

6.225

6.225

6.225

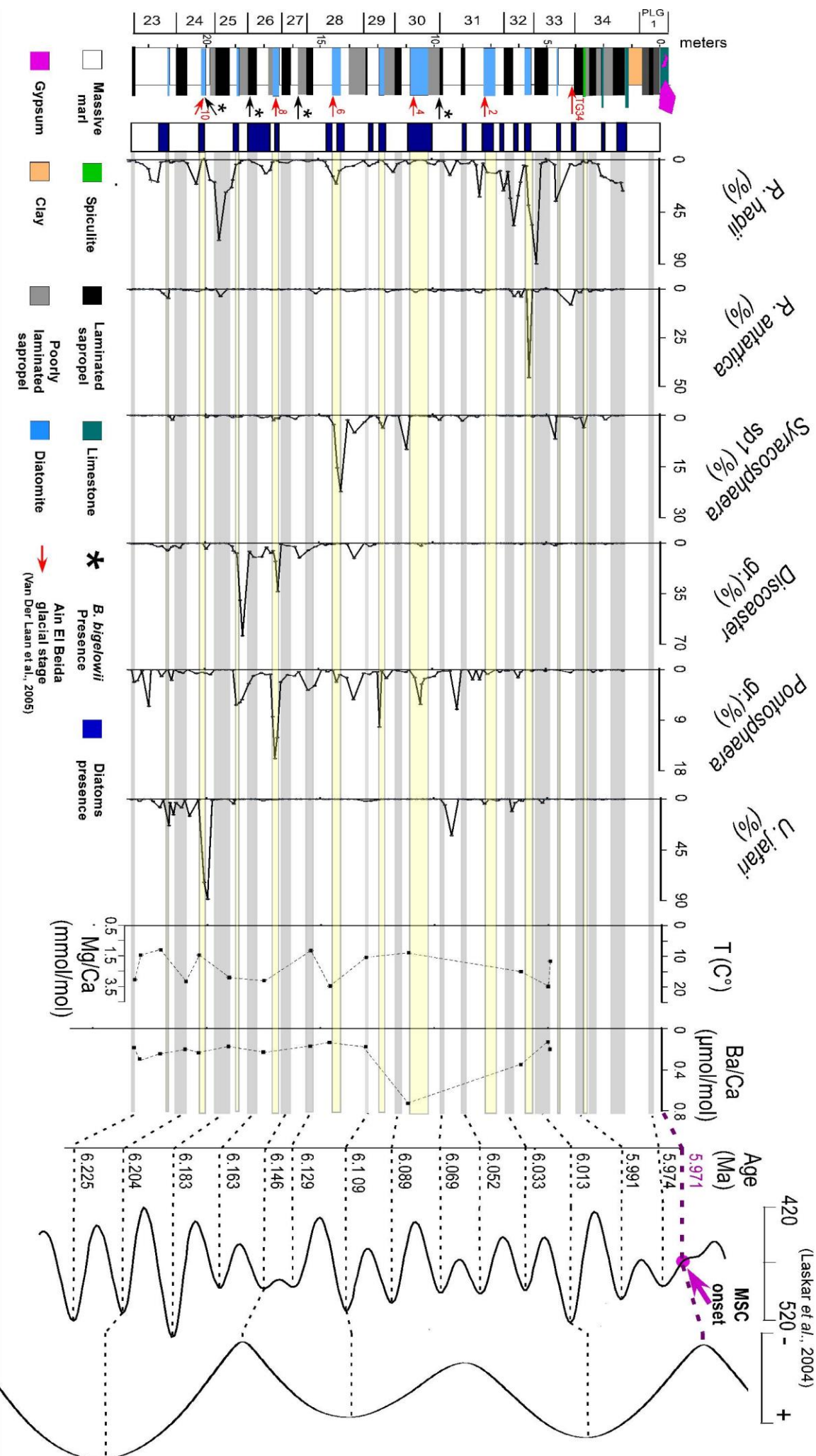
6.225

6.225

6.225

6.225

Summer insolation 65°N (W/m²),
Eccentricity index
(Laskar et al., 2004)



- Massive marl
- Gypsum
- Clay
- Poorly laminated sapropel
- Limestone
- Diatomite
- B. bigelowii* Presence Ain El Beida glacial stage (Van Der Laan et al., 2005)
- Diatoms presence

23 24 25 26 27 28 29 30 31 32 33 34 PLG₁
meters

R. haqii (%)
R. antarctica (%)
Syracosphaera sp1 (%)
Discoaster gr. (%)
Pontosphaera gr. (%)
U. fatani (%)

T (°C)

Ba/Ca (μmol/mol)

Age (Ma)

MSC onset

Fig. 3.1; 3.2: CN relative abundance compared with the Mg/Ca and Ba/Ca performed on *O. universa* and with orbital variation parameters (Laskar et al., 2004) and the glacial stage inferred from planktic and benthic $\delta^{18}\text{O}$ (red arrows, van der Laan et al., 2005). Blue intervals on the left column indicate diatom presence in the observed smear-slide. The numbers on the right line indicate the age of the sapropel mid-point expressed in Ma.

3.2 Trace elements analysis (Mg/Ca and Ba/Ca)

The obtained Mg/Ca values span from 1.21 mmol/mol to 3.45 mmol/mol and correspond to temperatures ranging from 9.5 °C to 19.7 °C. A long term temperature trend toward the MSC onset is not discernible in our results. The recognition of temperature trends is biased by the low stratigraphic resolution obtained in the upper portion of the studied section; however, it is still possible to observe an oscillation in phase with precessional climatic variation, with higher values (17.5°C - 19.2°C) during the upper part of the sapropel deposition in cycles UA23, UA25 and UA33. Low temperature values are recorded in the middle part of the sapropel in UA28 (8.1°C) and in the upper marl roughly at the marl-sapropel transition in UA29 (10.4°C). The lower marls are characterized by low temperature values in the cycles UA23, UA24 and UA30 (7.8°C – 9.6°C), a mild value in UA32 (15°C) and a high value in UA28 (19.7°C).

The Ba/Ca values generally span from 0.1 $\mu\text{mol/mol}$ to 0.4 $\mu\text{mol/mol}$. The higher value (0.7 $\mu\text{mol/mol}$) is recorded in the lower marls of the cycle UA30. The obtained Ba/Ca values are systematically lower compared to the *O. universa* Ba/Ca results obtained by Sprovieri et al. 2008 (Falconara section, Sicily, Italy); this reflects more arid conditions in the Sorbas Basin compared to Falconara, probably due to African rivers influence (Griffin, 2002) in the southern Mediterranean. Subtle oscillations are recorded in the UA23-UA29 interval, where slightly lower values are associated with the sapropels and relatively higher values are documented for the lower marls, with the outstanding high values of cycle UA30.

4. Discussion

4.1 Paleoecology of selected calcareous nannofossil taxa

The paleoecological signature of the species present during the MSC onset bioevent is of paramount importance for deciphering the paleoenvironmental changes preceding and characterizing the MSC onset. Since the interpretation of the Messinian CN abundance fluctuation is complicated by the fact that many of these species are extinct, we are providing a detailed review of the CN species paleoecology including new insights from this study (summarized in Fig. 4).

4.1.1 *Sphenolithus gr.*

A wide range of paleoecological preferences have been attributed to the extinct *Sphenolithus* spp. It is generally described as adapted to warm, stratified and oligotrophic environments during the Cenozoic (Perch Nielsen, 1985), from the late Eocene to the late Miocene (Mejía-Molina et al., 2010) and during the Pliocene (Gibbs et al., 2004), with a deep photic zone preferred habitat (Gibbs et al., 2004). Furthermore, *Sphenolithus* spp. is also regarded to prefer either open and well oxygenated marine conditions during the late Paleogene (Aubry et al., 1992) or marginal environments with freshwater influxes during the Burdigalian of the Northern Alpine foredeep (Auer et al., 2014). During the Messinian, *Sphenolithus gr.* is widely reported in the Mediterranean pre-evaporitic marls (Blanc-Valleron et al., 2002; Kouwhenhoven et al., 2006; Gennari et al., 2018; Flores et al., 2005; Lozar et al., 2018) and interpreted as a deep photic zone dweller (Flores et al., 2005), an opportunistic and mesotrophic taxon by Wade and Bown (2006) and adapted to high salinity fluctuations and to a shallow environment (Lozar et al., 2010). In the lower UA5-UA8 cycles, maxima in *Sphenolithus gr.* abundance occurs in the middle lower part of the sapropels, and this taxon is replaced in the middle-upper part by *Discoaster gr.* (Flores et al., 2005).

Our data show a cyclical increase in *Sphenolithus gr.* abundance in the middle-upper part of the sapropels, however, in our samples *Discoaster gr.* are often poorly preserved and recrystallized,

hampering the identification of the turnover recorded by Flores et al. (2005). *Sphenolithus* gr. high abundances are also retained in the upper marls of cycles UA27 and UA28, centred on the 6.14 Ma 100 kyr eccentricity minimum, which corresponds to a prolonged insolation maxima phase during an interglacial stage (Laskar et al., 2004). *Sphenolithus* gr. abundance is suppressed during the glacial isotope stages (red arrows in Fig. 3.1) inferred from the benthic and planktic $\delta^{18}\text{O}$ in the Ain el Beida section (Morocco, van der Laan et al., 2005). In our data, *Sphenolithus* gr. show a positive correlation with the temperature inferred from Mg/Ca (despite the lower resolution of this proxy), in agreement with previous studies (Haq and Lohmann 1976; Lohmann and Carlson, 1981; Flores et al., 1995; Castradori, 1998; Flores et al., 2005); this correlation is further supported by the dominance of warm oligotrophic foraminifers, which indicate the formation of a strong and permanent pycnocline at depth with the subsequent stratification of surface waters (Sierro et al., 2003). All these features suggest a robust temperature control on *Sphenolithus* gr. abundance. This is further suggested by scarcity of these taxa in the Northern Mediterranean pre-evaporitic successions (Piedmont basin and northern Apennines), where the *Sphenolithus* gr. abundance exceed 20% only during the MSC onset bioevent (see Section 5.4). However, the notable abundance differences of the *Sphenolithus* gr. peaks in the sapropelitic layers of the adjacent Tokhni (present in all the sapropel layers) and Pissouri (low and scattered occurrence) sections in the eastern Mediterranean allows to rule out temperature as the only factor controlling the abundance fluctuations of *Sphenolithus* spp. Furthermore, in the evaporitic phase of the Messinian Polemi section (Cyprus), Wade & Bown (2006) recorded high abundances of *Sphenolithus* gr. in diatom rich layers, suggesting the ability of this species to thrive in mesotrophic environments. Similar diatom-*Sphenolithus* coupling assemblages were found in the Moncalvo section (Lozar et al., 2018). This further suggests that *Sphenolithus* gr. abundance is not only controlled by the water temperature, but also by other environmental parameters, such as nutrient availability in the water column (deep vs shallow, oligotrophic vs eutrophic).

4.1.2 *Umbilicosphaera rotula*

Ziveri et al. (2004) reported that the living relatives of *U. rotula*, *Umbilicosphaera sibogae* var. *sibogae* and *Umbilicosphaera sibogae* var. *foliosa* mostly occur under oligotrophic and mesotrophic conditions, respectively. Guerreiro et al. (2014) suggest that *Umbilicosphaera* gr. is an upper photic zone dweller. Alves et al. (2016) use the genus *Umbilicosphaera* as a proxy for eutrophic conditions, due to the negative correlation with the oligotrophic genus *Discoaster* in the Miocene record of the Campos Basin (Brasil). Flores et al. (2005) recorded the *U. rotula* maximum abundance preferentially in the Sorbas upper marls. These authors suggest that *U. rotula* was able to thrive in surface waters where nutrients become depleted after diatom blooms, in a stable pycnocline development regime. In our longer record, *U. rotula* is present in the upper marls as well, but abundance maxima are also recorded in the upper marls-sapropel transition (base UA24, UA29 and UA32). The upper marls-sapropel transition (especially from UA17 upwards) were deposited under severe conditions in the upper portion of the water column, as suggested by the absence of planktic foraminifera, pointing to the ability of *U. rotula* to thrive also in a “stressed” environment (Sierro et al., 2003). The “stressed” condition may be related to eutrophic surface water (Sierro et al., 1999; 2003).

The finding of *U. rotula* high abundance, embedded in clusters of silica-rich matrix, in the sediments recording the MSC onset bioevent (this study, Fig. 5; Pollenzo section, Natalicchio et al., 2019) suggests that *U. rotula* was mainly transported to the sea floor by sinking fecal pellets. Fecal pellets and marine snow are formed in the upper oxygenated layers and enhanced during episodes of increased productivity (Aldredge and Silver, 1988; Dela Pierre et al., 2014). Sierro et al. (2003) report high abundance of benthic foraminifera in the upper marls; these authors indicate that peaks of benthic foraminifera in the UA corresponds to dominant *Bolivina* and *Bulimina* occurrences. These taxa are adapted to sea floor eutrophic conditions (Jannink et al., 1998; Murray, 2006) and their presence concomitant with *U. rotula* peaks, suggests high productivity in the water column and high organic matter export to the sea floor. This situation is exacerbated in cycles UA24 and UA34, where *U. rotula* peaks are accompanied by very abundant benthic foraminifers (Sierro et al., 2003; this study

Fig. 6). This supports our interpretation that *U. rotula* was able to flourish in high abundance in eutrophic conditions.

4.1.3 *Rhabdosphaera clavigera*

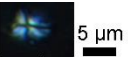

R. clavigera is a living taxon; it is reported as a warm water species that proliferates in oligotrophic surface conditions (Ziveri et al., 2004); it has an opportunistic behaviour and does not tolerate low light irradiance levels (Haidar & Thierstein, 2001; Malinverno et al., 2003); it has a preference for a stable and stratified water column, not tolerating turbulence (coastal proximity and/or upwelling) (Silva et al., 2008). In the late Quaternary sapropels, the increase of *Rhabdosphaera* spp. and *Florisphaera profunda* are positively correlated (Castradori, 1993; Negri et al., 1999a, b), suggesting some connection with the Deep Chlorophyll Maximum (DCM) development. The *R. clavigera*-sapropel relationship was recorded in the lower cycles of the UA (Flores et al., 2005), while it is not evident in our results. Our data show a scattered distribution, with few prominent peaks (3% - 8%) in the upper and lower marls and in diatomite of cycle UA28, coinciding with a glacial isotope stage (Van der Laan et al. 2008). Here, *R. clavigera* co-occurs with *C. leptoporus* and *C. pelagicus*, forming an assemblage already recorded by Silva et al. (2008) in the present-day Lisbon Bay. Both *C. leptoporus* gr. and *C. pelagicus* prefer cold-temperate water column and high to moderate nutrient availability (Giraudeau, 1992; Cachão and Moita, 2000; Cachão et al., 2002; Ziveri et al., 2004; Triantaphyllou et al., 2009; Okada and MacIntyre, 1979; Negri et al., 1999a). It appears that the increase in abundance of the genus *Rhabdosphaera* can be explained by opportunistic behaviour at the end of the spring bloom when nutrient levels start to become impoverished. *Rhabdosphaera clavigera* is a minor component of the Messinian CN assemblage (Flores et al., 2005; Lozar et al., 2018; Lozar & Negri, 2019; this study) that rarely exceed 10% of the total assemblage. The low *R. clavigera* abundance could be the result of some seasonal bloom, occurring when the spring temperatures are high enough, runoff is low and nutrients are depleted in the upper water column. These conditions

were seldom achieved during the deposition of the UA when the continental run-off was low during insolation maxima, or the spring temperatures were high enough during insolation minima.

4.1.4 *Helicosphaera carteri*

Helicosphaera carteri is an extant species that has been documented in mesotrophic/eutrophic, hyposaline and turbid waters (Giraudeau, 1992; Ziveri et al., 2004), and estuarine environments (Cachão et al., 2002). *Helicosphaera carteri* also proliferates in the mid photic zone (Corselli et al., 2002; Crudeli et al., 2006) and has a preference for warm waters (Brand 1994; Ziveri et al., 2004). Generally, in the Sorbas Basin, *H. carteri* abundance maxima are cyclically reached close to, or in, the diatomite.

Our data also reveal that *H. carteri* abundance acme occurs between UA29 and UA30, concurrently with a pronounced Ba/Ca peak. These findings further indicate the ability of this species to tolerate salinity fluctuation (or reduction in the water transparency) due to the increased continental run-off in a mesotrophic environment.

<i>Sphenolithus gr.</i> 			<i>Rhabdosphaera clavigera</i> 		
AUTHOR/S	LOCATION STUDIED	ECOLOGICAL PREFERENCES	AUTHOR/S	LOCATION STUDIED	ECOLOGICAL PREFERENCES
Perch Nielsen, 1985 *Cenozoic	Synthesis	Warm/oligotrophic water column	Ziveri et al., 2004 *Living	Atlantic	Warm/oligotrophic surface water
Mejia-Molina et al., 2010 *Upper Eocene - Upper Miocene	Northern Colombia, Caribbean sea	Warm/oligotrophic, stratified water column	Haidar & Thierstein, 1997 *Living	North Atlantic	Opportunistic, warm water, high light intensity tolerant
Gibbs et al., 2004 *Pliocene	Ceara Rise (South Atlantic)	Warm/oligotrophic, stratified water column, DCM presence	Malinverno et al., 2003 *Living	East Mediterranean	Warm water, upper photic zone dweller
Aubry et al., 1992 *Late Paleogene	Review	Open and well oxygenated marine conditions	Dimiza et al., 2008 *Living	East Mediterranean	Upper photic zone dweller
Wade & Bown, 2006 *Messinian	Cyprus	Mesotrophic water column	Silva et al., 2008 *Living	North Atlantic (Portugal coast)	Stable and stratified water column
Lozar et al., 2010 *Messinian	Piedmont (Italy)	High salinity fluctuations, shallow environment	Negri et al., 1998 *Tortonian - Messinian	M. Del Casino (Italy)	Opportunistic, nutrient decreasing
Flores et al., 2005 *Messinian	Sorbas (Spain)	Warm/oligotrophic	Flores et al., 2005 *Messinian	Sorbas (Spain)	Warm/oligotrophic water column
This study *Messinian	Sorbas (Spain)	Warm/stratified water column, DCM presence	This study *Messinian	Sorbas (Spain)	Seasonal proliferation with high spring temperature and decreasing nutrients conditions



<i>Umbilicosphaera rotula</i> 			<i>Helicosphaera carteri</i> 		
AUTHOR/S	LOCATION STUDIED	ECOLOGICAL PREFERENCES	AUTHOR/S	LOCATION STUDIED	ECOLOGICAL PREFERENCES
Ziveri et al., 2004 (<i>Umbilicosphaera sibogae</i> var. <i>sibogae</i>) *Living	Atlantic	Oligotrophic water column	Ziveri et al., 2004 *Living	Transects	Warm and mesotrophic water column
Ziveri et al., 2004 (<i>Umbilicosphaera sibogae</i> var. <i>foliosa</i>) *Living	Atlantic	Mesotrophic water column	Giraudeau, 1992 *Living	South Atlantic	Eutrophic and hyposaline water column
Guerreiro et al., 2017 (<i>Umbilicosphaera</i> spp.) *Living	North Atlantic	Upper photic zone dweller	Crudeli et al., 2006 *Late Pleistocene - Holocene	West Mediterranean	Middle photic zone dweller
Alves et al., 2016 (<i>Umbilicosphaera</i> spp.) *Miocene	Campos Basin (South Atlantic)	Eutrophic water column	Flores et al., 2005 *Messinian	Sorbas (Spain)	Cool and mesotrophic water column
Flores et al., 2005 *Messinian	Sorbas (Spain)	Nutrient decreasing, stable pycnocline development	This study *Messinian	Sorbas (Spain)	Mesotrophic water column, salinity fluctuations
This study *Messinian	Sorbas (Spain)	Eutrophic upper water column			

Fig. 4: Ecological preferences inferred for the CN involved in the MSC onset bioevent coming from previous work and this study. * Indicate the studied time interval

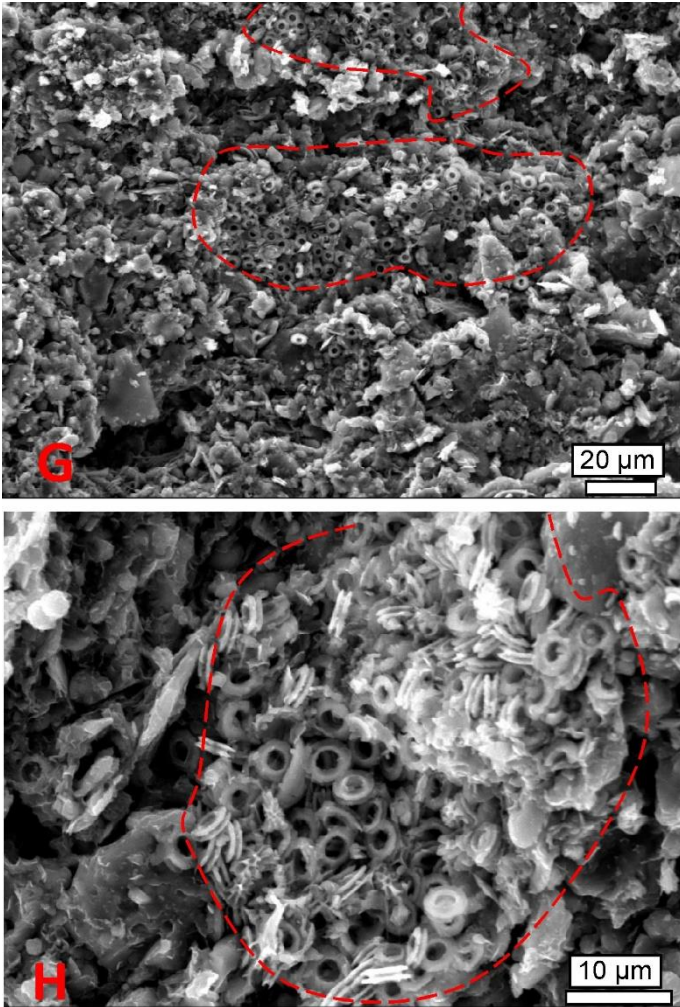


Fig. 5: SEM analyses of the samples containing the MSC onset bioevent (cycle UA34, *U. rotula* peak). G-H: Faecal pellet containing cluster of coccoliths (mostly *U. rotula*) embedded in a silica-rich matrix.

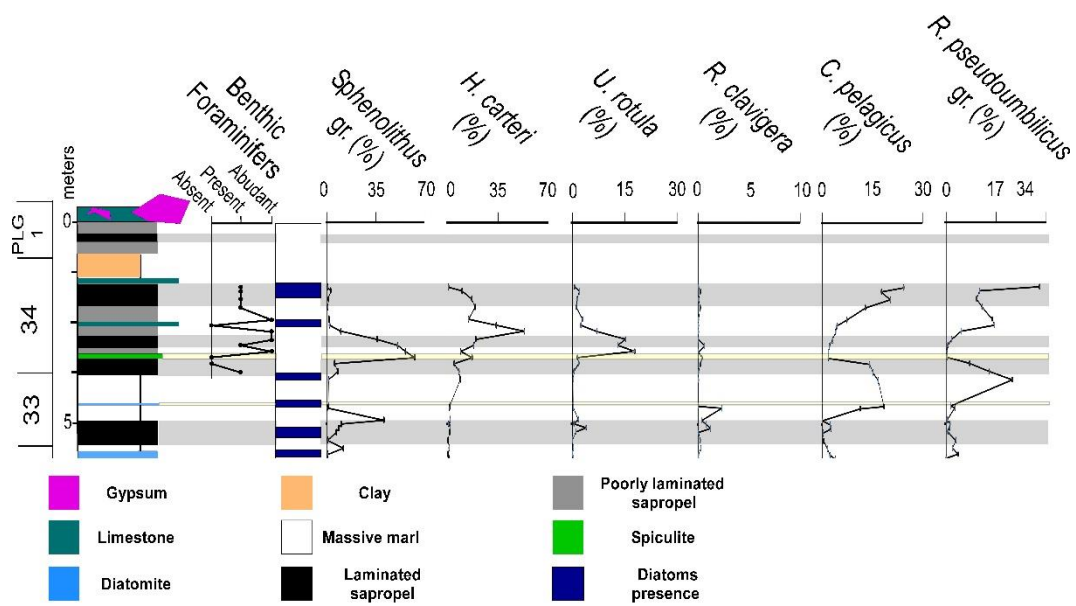


Fig. 6: Qualitative benthic foraminiferal analysis performed in the cycle UA34. The benthic assemblage is dominated by the taxa *Bolivina* and *Bulimina*. Planktic foraminifers >125 µm are absent in the cycle UA34.

4.2 Factors controlling the sapropels deposition in the Sorbas Basin

According to Sierro et al. (2003) the trigger for the sapropelitic deposition was the buoyancy gain of the surface water that promoted density stratification of the water column and anoxic condition at the sea floor. This mechanism was strengthened by the still relatively high productivity, which started during the deposition of the diatomite/upper marls and favoured the accumulation of organic matter at the sea floor (Sierro et al., 2003). This interpretation is based on the observation of the foraminiferal distribution and their stable isotope signature. The new and extended CN data add new insights and contribute to a better understanding of the mechanism of Messinian sapropel formation and its evolution towards the MSC onset.

The CN assemblages recorded at the transition from upper marls to sapropel and in the basal portion of the sapropel is dominated by *R. minuta*, *U. rotula* and *C. leptoporus* gr. *Reticulofenestra minuta* reflects high nutrient availability in the upper water column (Flores et al., 1995, 2000; Takahashi and Okada, 2000; Wade & Bown, 2006; Imai et al., 2013, 2015, 2017; Auer et al., 2014; Athanasiou et al., 2015), as also highlighted by *U. rotula* (see Section 4.1.2). In our results, *C. leptoporus* gr. specimens mainly belong to the large morphotype, which proliferate today in mesotrophic environments (Ziveri et al., 2004). At the same time, the dataset of Sierro et al. (2003) shows that the transition to the sapropel is also characterized by the presence of cold/eutrophic planktic foraminifers, such as *T. quinqueloba/multiloba* (above UA20) and *Globigerina bulloides* (below UA16). Benthic foraminifers are commonly dominated by high nutrient/low oxygen taxa from ca. 6.4 Ma onward (*Bulimina* gr., *Bolivina* gr. and *Uvigerina/Rectouvigerina*) (Sierro et al., 2003). Their maximum abundance is cyclically reached in the upper marls, followed by a sudden drop at the sapropel inception. At the sapropel base, the concomitance of high productivity at the sea surface, disappearance of benthic foraminifera and preservation of organic matter strongly suggests that the

increasing export of organic carbon to the sea floor exceeded the threshold leading to oxygen deficiency. Moreover, oligotrophy and stratification proxies are commonly lacking at the sapropel inception throughout the UA. Consequently, the anoxic conditions reached at the sea floor were more likely related to the huge oxygen consumption of the organic matter at the sea bottom rather than to the stagnation of the basin, similar to what happens today in the Oxygen Minimum Zone (Schimmelmann et al., 2016).

Evidence of stratification and DCM productivity are provided by *Sphenolitus* gr. high abundance in concomitance with surface oligotrophic planktic foraminifera (e.g. *O. universa* or *Globigerinoides* gr.) in the middle-upper sapropel partition, where $\delta^{18}\text{O}$ indicates a marked increase in fresh water input (Sierro et al., 2003; Pérez-Folgado et al., 2003, Reghizzi et al., 2017). With the establishment of predominantly stratified conditions, promoted by increasing runoff at time of maximum insolation (Sierro et al., 2003), most of the productivity shifted down to the DCM. The establishment of a DCM is a common feature characterizing the water column structure during Pleistocene sapropel deposition (Kemp & Villareal, 2013; Rohling et al., 2015 and references therein). The primary production in the DCM is mainly a new production that greatly enhances the export of organic matter from the photic zone when the water column is stratified and the surface layer is depleted in nutrients (Rohling and Gieskes, 1989; Legendre & Le Fevre, 1989; Eppley, 1989). Among other things (sinking speed, coating, sorption onto mineral particles, redox condition, microbial consumption; Hedge and Keil, 1995; Keil and Mayer, 2004; Burdige, 2007; Keil, 2017), the efficiency of organic carbon export also depends on the depth of the sea floor with respect to the (photic zone) depth at which most of the productivity is generated. We speculate that the development of a DCM permits an efficient transfer of the sinking organic carbon to the sea floor, also because the organic carbon does not flow throughout the photic zone, where the organic matter consumption is more effective (Neuer et al., 2002; De La Rocha & Passow, 2007). This mechanism is further enhanced when it occurs in a shallow environment like the Sorbas Basin, where benthic foraminifers and field observations suggest an evolution of the paleodepth from a fairly deep (1100m) at the LU/UA transition to a shelf depth (ca.

150m) prior the MSC onset (Dronkert, 1976; Troelstra et al., 1989; van de Poel et al., 1992; Baggley, 2000; Clauzon et al., 2015; Modestou et al., 2015). Among DCM proxies, the absence of the DCM dweller Neogloboquadrinids, in concomitance with *Sphenolithus gr.*, could be the result of different temperature preferences, because the living descendant of the Messinian Neogloboquadrinids proliferate today in the Mediterranean when winter temperatures are below 14°C (Kallel et al., 1997; Sierro et al., 2003). This is evident in the sapropel of cycle UA32, which corresponds to a relatively low summer insolation maxima at 65°N (Laskar et al., 2004) compared to other cycles, allowing the Neogloboquadrinids to be present in high abundance (Sierro et al., 2003) and suppressing the *Sphenolithus gr.* abundance. Nevertheless, a good correlation exists between the *Sphenolithus gr.* and the Neogloboquadrinids by comparison of our results with the dataset provided by Sierro et al. (2003) (UA25, UA28 and UA33 lower marls). We argue that, while stratification increased during the middle upper part of the sapropel formation, productivity, in part transferred to the lower photic zone, remained an important factor leading to the organic matter preservation at the sea floor. Overall, the fossil assemblage reflects high productivity and organic carbon export at the sapropel inception (anoxia triggering factor), and the presence of stratification and a DCM in the upper part of the sapropel (anoxia maintaining factor). Deviations from the pattern described above are only observed in cycles UA25 and UA30, where *Sphenolithus gr.* are present already from the base of the sapropel, like in the UA5-UA8 interval (Flores et al., 2005). Planktic foraminifera are in line with these deviations; in fact, *Trilobatus sacculifer* (*Globigerinoides sacculifer* in Sierro et al., 2003) and *O. universa* are dominant (>80%) in UA25 and UA30 sapropel base (Sierro et al., 2003), respectively, indicating a well-established stratification with oligotrophic and warm surface waters.

The deposition mechanism of the pre-evaporitic Sorbas Basin sapropel differs from the more recent Holocene/Pleistocene sapropel deposited in deep-water setting. Whilst the disruption of deep and intermediate water circulation can still be considered the driving cause for deep water Plio-Pleistocene sapropel formation (Rohling et al., 2015), we point to productivity processes as more relevant in marginal and restricted environments, like the Sorbas Basin. These differences

challenge the view of a single mechanism as a trigger for the cyclical sapropel deposition throughout the Neogene and Quaternary Periods.

4.3 Factors controlling the diatomite deposition in the Sorbas Basin

The precessional quadripartite cycle of the pre-evaporitic Sorbas Basin represents a general deviation from the recurrent tripartite “Tripoli” precessional cycle outcropping in Sicily and Gavdos (Blanc-Valleron et al., 2002; Pérez-Folgado et al., 2003). Basically, what differentiates the Sorbas Basin is the presence of the lower marls sandwiched between the sapropel and the diatomite. The fossil assemblage recorded in the lower marls is similar to that of the upper part of the sapropel, except for the presence of Neogloboquadrinids and benthic foraminifers (see Fig. 3 and Fig. 4 of Sierro et al., 2003). The Ba/Ca values are cyclically slightly higher in the lower marls suggesting an enhanced freshwater input. All the proxies (oligotrophic planktic foraminifers, *Sphenolithus gr.*, the $\delta^{18}\text{O}$ and the Neogloboquadrinids) still point to strong stratification of the water column, with oligotrophic conditions at the surface and the presence of a pronounced DCM during the lower marl deposition (Fig. 7). Notwithstanding, the return of benthic foraminifers in the lower marls (Sierro et al., 2003) is a clear signal of an oxygenation recovery at the sea floor. Rather than a return of mixing process that delivers oxygen to the sea bottom, it could be inferred that at this time a further shoaling of the nutricline occurred, as a result of the continued and enhanced riverine input that started during the upper part of the sapropels deposition, as also suggested by Sierro et al. (2003). The shoaling of the nutricline may result in an increased distance between the DCM and the sea floor, increasing the remineralisation of the organic matter during its sink through the photic zone and suppressing the export flux at the sea floor, responsible for the anoxic condition.

The diatomites are generally characterized by the presence of *H. carteri*, *C. pelagicus* and *R. pseudoumbilicus gr.* among the CN, and both cold/eutrophic and warm/oligotrophic planktic foraminifers (decreasing warm/oligotrophic over cold/eutrophic ratio; Sierro et al., 2003). The ecological requirements for *H. carteri* are discussed above (see Section 4.1.4); *C. pelagicus* is referred

as a cold species with the preference of high nutrient availability (Negri et al., 1999a, b; Ziveri et al., 2004), probably provided by upwelling (Cachão and Moita, 2000; Giraudeau, 1992), although some authors attribute to *C. pelagicus* the capability to proliferate in a wide range of salinity conditions (from 26.9 to 36‰) (Silva et al., 2008). *Reticulofenestra pseudoumbilicus* is referred to prefer high nutrient availability, with no particular preferences for water temperature (Lohmann and Carlson, 1981). The coexistence of cold/eutrophic, warm/oligotrophic and fresh water sensitive species may indicate that the diatomite deposition was characterized by strong seasonality, with more oligotrophic surface conditions associated with a DCM during summer, and more eutrophic surface conditions during winter/spring. A strong seasonality during the diatomite deposition is further indicated by the presence of *Thalassionema* and *Rhizosolenia* (Pérez-Folgado et al., 2003) among the diatoms. In fact, *Thalassionema* is generally associated with surface productivity (McKenzie et al., 1979; Moissette and Saint Martin, 1992), conditions that probably occurred during winter, and *Rhizosolenia* is generally referred as a DCM inhabitant (Margalef, 1978; Kemp and Villareal, 2013), conditions that probably occurred during summer.

According to Filippelli et al. (2003) siliceous productivity was triggered by a mechanism of enrichment in phosphorous, called sediment-nutrient-oxygen feedback (SNO Effect), which acted within the Sorbas Basin at the precessional scale. The authors suggest that during the sapropel deposition, the bottom water stagnation caused the build-up of phosphorous in the surface sediments, below the photic zone. This trapped the phosphorous reservoir below the pycnocline; the phosphorous was then injected back into the photic zone at the recovery of the water mixing during cold phase, resulting in an increased biosiliceous productivity and the consequent diatomite deposition. Supporting this scenario, we also claim that the dissolved silica is the main limiting nutrient for biosiliceous productivity (Ragueneau et al., 2000), and the preservation of the diatom frustules is strongly related to the dissolved silica content in the water column and in the sediments (Pellegrino et al., 2018). The dissolved silica in the ocean, like phosphorous, is mainly provided by continental runoff (Treguer & De La Rocha, 2013; Pellegrino et al., 2018) and it can be associated with the

phosphorous SNO effect as well, because the silica content in the water column increases with water depth. The dissolved silica and phosphorous were mainly provided by the rivers during the upper part of the sapropel and lower marl deposition, remaining trapped below the photic zone because of the stratification that occurred at this time. When the temperature started to gradually decrease, promoting water mixing and the disruption of the stratification, the nutrients were distributed in the photic zone stimulating biosiliceous productivity. Moreover, the same mechanism suggested by Filippelli et al. (2003) at the precessional scale, may be responsible for the cyclical dissolved silica and phosphorous enrichment in the photic zone during an annual cycle: during spring the nutrients were provided by run-off and remained trapped below the photic zone during summer stratification, then the stratification broke during autumn/winter and distributed the nutrients into the photic zone. The break of the stratification that occur during late autumn, could promote a huge diatoms flux at the sea bottom (i.e. fall dump, according to Kemp et al. 2000). The rapid accumulation of diatoms at the sea floor was responsible for the temporary oversaturation of dissolved silica, promoting diatom frustules preservation. The Neogloboquadrinids are phytoplankton grazers that feed on diatoms and are adapted to exploit the DCM (Hemleben et al., 1989; Sierro et al., 2003). The concomitant presence of scattered diatom frustules and the Neogloboquadrinids during the lower marls deposition, indicates that the diatoms were present also during this interval, but the diatom flux at the sea floor was not sufficient to sustain the dissolved silica oversaturation, responsible for the diatom preservation. The strong seasonal signal derived by the microfossil assemblages that characterizes the diatomites suggests that runoff was still important to sustain siliceous productivity by replacing the fraction of silica buried in the sediments.

Above the diatomites, the upper marls are characterized by high productivity mainly confined in the surface water expressed by the fossil assemblage (see Section 4.2). Thus, the decline of the siliceous productivity (below the threshold of silica preservation) was related to the combination of the depletion of the silica and phosphorous deep reservoir (by means of the SNO effect) and the

decreased runoff contribution (Sierra et al., 2003). The latter was a consequence of the decreasing insolation index leading to drier and cooler conditions.

4.3 The sapropel UA34 case

Differently from cycles UA1 to UA33, the cycle UA34 does not show the quadripartite pattern, as it is mainly made up of dark, organic-rich marls (sapropel-like), intercalated with 2 limestone and a spiculite layers (see Section 2.3). Increases of *R. pseudoumbilicus* gr. and *C. pelagicus* were recorded below the second limestone layer in organic-rich layers. In our results *R. pseudoumbilicus* gr. and *C. pelagicus* abundance maxima are recorded during diatomite deposition; consequently, we suggest that the *R. pseudoumbilicus* gr. and *C. pelagicus* increases in the cycle UA34, in the poorly or well laminated sapropels below the second limestone layer, indicate the transition from insolation maximum to minimum. This transition is further indicated by diatom presence, which frequently occurred at this level (Fig. 3). We suggest that, at the time just before the MSC onset, the ongoing basin restriction promoted an increase in the marine productivity, resulting in an enhanced export of the organic matter to the sea bottom; this in turn led to anoxic bottom conditions, without the contribution of the stagnation of the deep water. This mechanism resulted in a constant accumulation of organic-rich sediments and the obliteration of the cyclic pattern observed in the older UA cycles. This represents another clue indicating that the stagnation of the basin played a secondary role in the sapropel deposition in the shallow Sorbas Basin, which is best explained by oxygen consumption at the sea bottom due to the high productivity and high organic matter export from the photic zone.

4.4 The MSC onset bioevent record in the Western Mediterranean

Basically, the MSC bioevent was recorded in all on shore sections reporting a CN abundance record. The MSC bioevent consists of a succession of abundance peaks of the species *S. abies*, followed or accompanied by *H. carteri*, *U. rotula* and *R. clavigera*. This peculiar succession of bioevents is recorded in the Perales section in the cycle UA34, reinforcing the idea that the same

paleoenvironmental change took place in the whole Mediterranean approximately at the MSC onset. Based on the reported widespread occurrence, we confirm that the MSC bioevent is a good proxy of the MSC onset occurrence (Lozar et al., 2018) and it also represents a reliable tool for deciphering the environmental changes characterizing the onset of this basin-wide event. Information regarding the MSC onset record across the Mediterranean and its detailed description are compiled in Lozar and Negri (2019).

4.5 Paleoenvironmental reconstruction during the MSC bioevent

Prior to the MSC, the Mediterranean was affected by a progressive restriction of the marine connections with the Atlantic Ocean, commonly related to tectonic uplift processes in the gateway area (Duggen et al., 2003; Garcia-Castellanos and Villaseñor, 2011). The first evidence of significant restriction in the Mediterranean-Atlantic exchange was recorded by a reduction of deep-water ventilation all over the Mediterranean at 7.15 Ma, after the Tortonian-Messinian boundary (Kouwenhoven et al., 1999, 2003). This event is also associated with the increased deposition of diatom-rich sediments (Tripoli Formation, Sicily) or opal-rich deposits (Upper Abad, Spain) observed between 7.15 Ma and 6.7 Ma throughout the Mediterranean. The widespread precipitation of authigenic calcite, dolomite and/or aragonite between 6.3 and 5.97 Ma, immediately prior to the MSC onset, is another response to ongoing restriction (Roveri et al., 2014). This restriction in the Sorbas Basin resulted in a shallowing of the basin (Dronkert et al., 1976; Troelstra et al., 1980; van de Poel et al., 1992; Baggley, 2000; Clauzon et al., 2015, Modestou et al., 2015). In the nearby Bajo Segura Basin, a shallowing of the basin from outer to inner shelf was recognized at 6.03 Ma, described as a “consolidation phase” of the Mediterranean Basin restriction (Corbí et al., 2020). In Banengo, Moncalvo and Pollenzo sections (Italy; Lozar et al., 2018) only few precessional cycles (from 2 to 4) are present below the MSC bioevent, complicating the recognition of shoaling features. However, in these sections, the MSC bioevent is accompanied by the presence of benthic foraminifers indicating shallow

water (Banengo and Moncalvo; Lozar et al., 2018) or deep outer neritic to bathyal environment (Pollenzo section; Lozar et al., 2018).

As described above, the cycle UA34 of the Sorbas Basin represents the pre-evaporitic restriction acme. In this framework the MSC bioevent, found approximately at the MSC onset in the whole Mediterranean, is somehow related to this restriction effect. The acme of the pre-evaporitic basin restriction had the effect of modifying the basin susceptibility to the fresh water and nutrient input, due to decreased dilution caused by the reduction of the input of Atlantic water into the Mediterranean. This ultimately had the effect of amplifying the (paleo) ecological signal recorded in the sediment.

Approximately at the MSC onset, during the insolation maximum, the basin restriction in the whole Mediterranean, continuously affected by continental run-off, may have resulted in a reduced surface water buoyancy loss. The density differences between surface and intermediate waters is a recurrent feature reported before and during sapropel formation (Rohling et al., 2015 and references therein) and is thought to trigger the shoaling of the intermediate water toward the base of the photic zone, promoting new nutrient advection and fuelling the DCM (Rohling & Gieskes. 1989; Castradori et al., 1993; Rohling et al., 1994; Corselli et al., 2002). These conditions could have triggered the *Sphenolithus gr.* peak during the MSC onset bioevent in the whole Mediterranean. When the protracted continental run-off further decreased the surface buoyancy loss and triggered a further shoaling of the DCM, *Sphenolithus gr.* started to decrease. The protracted continental run-off also resulted in an increased surface salinity fluctuation, turbidity and high nutrient supply, limiting the light penetration in the photic zone and constraining the productivity in the middle-upper photic zone. These conditions led *U. rotula* and *H. carteri* to flourish. Seasonally, when the spring temperatures were high enough and nutrients started to be depleted or confined to the upper photic zone, *R. clavigera* peaked.

Above the MSC bioevent, the CN continues to be present for one precessional cycle in the Tokhni section (Cyprus; Gennari et al., 2018), for two precessional cycles in Pollenzo section (Italy;

Lozar et al., 2018), for ten precessional cycles in the Fanantello section (Italy, Manzi et al., 2007); in Moncalvo (Italy; Lozar et al., 2018) only diatoms are recorded in the cycles above the MSC bioevent. In all of these sections the evaporite deposition is delayed and replaced by organic-rich shales and carbonate. Overall, the fossil assemblage following the MSC bioevent reflects eutrophic conditions (Lozar et al., 2018; Gennari et al., 2018), resulting from the gateway restriction amplifying the continental run-off delivery of nutrients into the receiving basin. We suggest that the widespread record of the MSC onset bioevent in the Mediterranean is the fossil signal marking the last step of the restriction straddling the MSC onset, resulting in a widespread increase of marine productivity due to the overwhelming influence of the continental run-off to the basin. This restriction step likely coincided with the “climax phase” of the restriction proposed by Corbí et al., (2020), that is usually accompanied by the presence of dwarf planktic foraminifers (Lozar et al., 2010; Corbí et al., 2020; Mancini et al., in progress).

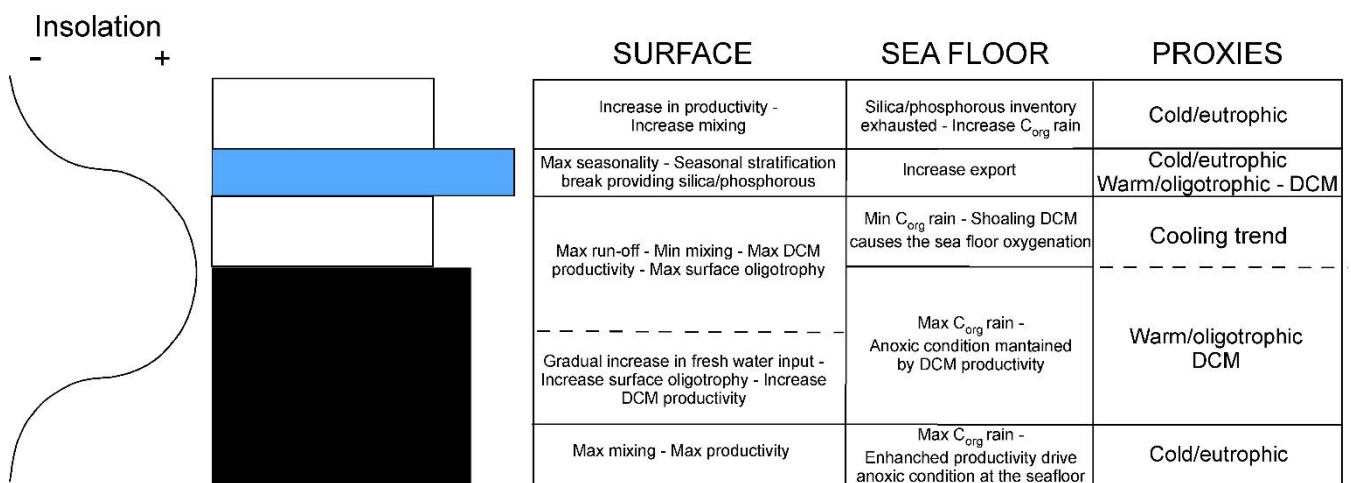


Fig. 7: Depositional model of the quadripartite precessional cycle in the Upper Abad member. The reconstruction of the surface water column and sea floor condition is achieved comparing our results with previous works from Sierro et al. (2003); Pérez-Folgado et al. (2003); Flores et al. (2005); Filippelli et al. (2005) and Reghizzi et al. (2017). C_{org} = Organic Carbon.

5. Conclusions

CN and geochemical analyses on *O. universa* tests were performed on the sediments spanning the MSC onset in the Sorbas Basin, adding new insight on the paleoenvironmental conditions

triggering the cyclical deposition of the lithological quadripartite cycle and on the MSC onset. The new foraminifers picking protocol proposed here allowed to bypass the problem of contamination by secondary calcite affecting the foraminifer shells.

Some important differences emerged between the most recent Holocene/Pleistocene sapropels deposited in deep-water setting and the shallow Sorbas Basin sapropels. The former were commonly characterized by a stratified water column at the onset of the sapropelitic episodes; the latter by high organic carbon export at the sapropel inception and by a DCM development in the middle-upper part of the sapropel.

The diatomite preservation in the geological record is related to conditions of exceptionally high dissolved silica in the water column, which is mainly provided by the rivers. In the Sorbas Basin the increased freshwater input, which occurred during the upper part of the sapropel and the lower marl deposition, generated a deep reservoir of nutrients (dissolved silica and phosphorous) that were injected into the photic zone when the decrease in temperature promoted the disruption of the stratification. This mechanism promoted a huge diatom proliferation and the consequent diatomite deposition. When the deep reservoir of dissolved silica was exhausted and was not replaced by continental run-off, bioturbated marls were deposited again at the top of the cycle.

In the last pre-evaporitic cycle (UA34), *C. pelagicus* and *R. pseudoumbilicus* gr. increase their abundance indicating a temperature decrease, a condition matching the passage from insolation maximum to insolation minimum. At this time, the deposition of sapropel-like layers further suggests that the deposition of organic-rich sediments does not necessarily require deep water stagnation. The cycle UA34 also records a precise sequence of CN peaks in abundance (MSC onset bioevent); this event was previously reported in the Messinian sections straddling the MSC onset in the Northern and Eastern Mediterranean. The MSC onset bioevent is comprised by a succession of peak abundances of *S. abies*, followed or accompanied by *U. rotula*, *H. carteri* and *R. clavigera*, and represents a useful tool to approximate the MSC onset. This peculiar and widespread fossil signal is the result of the restriction affecting the Atlantic gateway, which ultimately amplified the nutrients and continental run-off

susceptibility of the Mediterranean Basin, due to the decreased dilution effect of the Atlantic water in the recipient basin. The obliteration of the lithologically quadripartite cycle affecting the last pre-evaporitic cycle is also related to this restriction pulse. Overall, in both Eastern and Western Mediterranean the fossil signal above the MSC onset bioevent reflects the increase in marine productivity induced by the basin restriction that preconditioned the evaporitic phase.

Appendix A: Taxonomic appendix:

Amaurolithus delicatus (Gartner and Bukry, 1975)

Amaurolithus primus (Bukry and Percival, 1971)

Braarudosphaera bigelowii (Gran & Braarud 1935)

Calcidiscus leptoporus (Murray and Blackman, 1898)

Calciosolenia fossilis (Deflandre in Deflandre & Fert 1954)

Coccolithus pelagicus (Wallich, 1877)

Discoaster brouweri (Tan, 1927)

Discoaster pentaradiatus (Tan, 1927)

Discoaster variabilis (Martini and Bramlette, 1963)

Discosphaera tubifera (Murray & Blackman 1898)

Helicosphaera carteri (Wallich, 1877)

Pontosphaera discopora (Schiller, 1925)

Pontosphaera japonica (Takayama 1967)

Pontosphaera multipora (Roth, 1970)

Reticulofenestra antarctica (Haq, 1976)

Reticulofenestra haqii (Backman, 1978)

Reticulofenestra minuta (Roth, 1970)

Reticulofenestra pseudoumbilicus (Gartner, 1967)

Reticulofenestra rotaria (Theodoridis, 1984)

Rhabdosphaera clavigera (Murray and Blackman, 1898)

Sphenolithus abies (Deflandre and Fert, 1954)

Sphenolithus moriformis (Brönnimann & Stradner, 1960)

Syracosphaera pulchra (Lohmann, 1902)

Syracosphaera sp1

Umbilicosphaera rotula (Kkamptner, 1956)

Umbilicosphaera jafari (Müller, 1974)

Thoracosphaera heimii (Lohmann 1920)

Chapter 2 – Calcareous nannofossil size and abundance response to the Messinian Salinity Crisis onset and paleoenvironmental dynamics*

Dwarfism is a common feature affecting organisms across extreme events that characterized the Earth history, frequently referred as the result of “stressed conditions”. To date, no study addressed the morphological and biometric changes across the Messinian Salinity Crisis (MSC), one of the most recent and impacting event occurred in the Mediterranean Sea, historically interpreted as characterized by hypersaline conditions.

Here we focus on morpho/biometric changes affecting calcareous nannofossils (CN) toward the MSC onset in order to better constrain the paleoenvironmental dynamics and the loosely defined “stressed conditions” characterizing this interval.

Size characterization and absolute abundance of selected CN taxa were performed in the Perales (Spain, Western Mediterranean) and in the Banengo and Pollenzo sections (Italy, Northern Mediterranean). We also tested whether size changes and orbital cyclicity were related through analysing size and calcite mass of *Reticulofenestra minuta* using an automated image analysis system of CN recognition (SYRACO).

We recorded a significant size reduction affecting the CN taxa involved in the MSC onset biostratigraphic event, related to the restriction of the Mediterranean Basin that resulted in increased productivity and enhanced environmental variability, stimulating CN growth rate and decreasing their platelet sizes. *Reticulofenestra minuta* size and mass correlate with the orbital cyclicity with minimum values during periods of enhanced environmental variability, coinciding with the diatomitic deposition in the Sorbas Basin. Our finding reveals that the size change recorded across the MSC onset coincided with the instauration of a productive and highly variable environment, linked to the restriction of the paleo Gibraltar Strait.

*This chapter is based on Mancini, A. M., Grelaud, M., Ziveri, P., Nallino, E., Lozar, F. 2021: Calcareous nannofossil size and abundance response to the Messinian Salinity Crisis onset and paleoenvironmental dynamics. *Paleoceanography and Paleoclimatology*, 36 e2020PA004155

2- Material and methods

2.1 Studied material and age model (Piedmont Basin)

In the Piedmont Basin, 6 sample were studied spanning the last 5 pre-evaporitic precessional cycle in the Banengo section (45° 04' 21" N, 8° 03' 23" E; Fig. 1) and 9 samples spanning the last 7 pre-evaporitic precessional cycle in the Pollenzo section (44° 41' 06" N, 7° 55' 29" E; Fig. 1). In the Piedmont Basin, the precessional cyclicity in the pre-evaporitic successions is defined by the alternation of shale (sapropel equivalent) and white marls/carbonate rich layers (Dela Pierre et al., 2011; Lozar et al., 2018). The age model relies on foraminifer bioevents (Violanti et al., 2013; Lozar et al., 2018) and the

recognition of the first branching selenite bed, that corresponds to the 6th precessional cycle of the first stage of the MSC (Lugli et al., 2010, Dela Pierre et al. 2011).

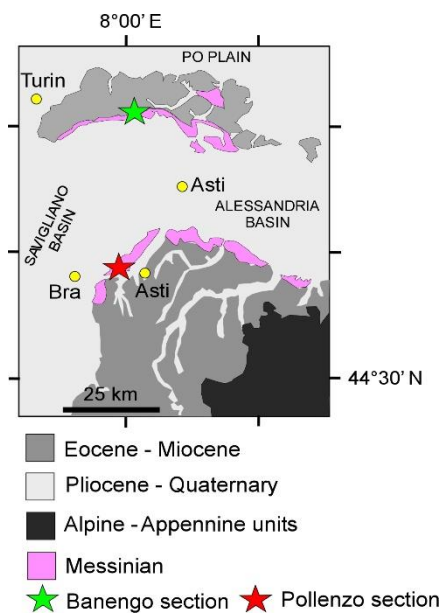


Fig. 1: Geological map of the North-West Italy showing the Piedmont Basin and the Banengo and Pollenzo sections (modified from Natalicchio et al., 2019 and Sabino et al., 2020).

2.2 Absolute abundance: samples preparation and counting

In order to perform the absolute abundance analyses, samples were prepared following the protocol developed by Beaufort et al. (2014). Briefly, a small amount of dried sediment (≈ 2.0 mg) was disaggregated into a 50 ml tube using a micro spoon. The tube was filled with ELIX water until 45 ml, hand mixed and sonicated for few seconds ($\cong 2$ seconds). A constant volume of the suspension (7 ml) was extracted with a pipette, poured into a beaker and sonicated a second time (≈ 2 seconds). The solution was then transferred, the beaker being cleaned 3 times by spraying ELIX water, into a petri dish with a cover slide at the bottom and left to settle for 4 hours. After the sedimentation of the material, the water was evaporated in an oven at 70°C. The obtained samples were permanently mounted on a slide with Norland Optical Adhesive 61 (“NOA61”) and analysed through light microscopy.

In each sample, a minimum of 500 nannofossils were identified using Olympus BX51 polarized microscope and counted at 1250X magnification. The reworked specimens, whose stratigraphic range is older than that of the analysed material, were not included in the counting but they were counted separately. The final results are expressed in number of nannofossils per gram of dried sediment (CN/g).

2.3 Biometric measurements

For each selected sample, the morphological parameters (Fig. 2) of 50 specimens were measured, that represents the common number used among the CN biometric studies (Tremolada et al., 2008; Lübke and Mutterlose, 2016; Faucher et al., 2017b). The number of analysed samples depended on the abundance and preservation of the analysed taxa; measurements were performed in 24 samples for *S. abies*, in 34 samples for *H. carteri*, in 26 samples for *U. rotula* and in 32 for *Coccolithus pelagicus*. Pictures of the specimens were obtained from a Jenoptik camera (using Progres 5 software) mounted onto Olympus BX50 microscope with a magnification of 1250X. The pictures were analysed with the software ProGres 5. One of the major issues in the biometric studies is the preservation of the specimens under exam, therefore we performed biometric measurements only on well preserved specimens; the broken, overgrown and etched specimens were excluded from the measurements. At least 1-2 samples were analysed for each precessional cycle (from UA23 to UA33), except in the last pre-evaporitic cycle (UA34) where all samples containing the selected CN taxa were analysed. This has been done in order to reveal the biometric change accompanying the MSC onset bioevent and the MSC onset.

Regarding *S. abies*, the measures were taken with the specimens viewed at 45° to the polarizers in order to discern the apical spine length. For *H. carteri* and *C. pelagicus*, the ellipticity index (average length/average width) was calculated in order to highlight morphometric changes. In our study the ellipticity index is used to track eventual malformations affecting nannofossils, evaluating the deviation from the ellipticity average calculated in our dataset. In the Perales section, for *U. rotula*,

both the coccolith external and central area diameters (Fig. 2) were measured. The ratio between central area diameter/total diameter lengths were calculated and values close to 1 indicate a large central area over the total diameter.

In order to demonstrate that the morphometric change accompanying the MSC onset bioevent were global or coeval, size analyses were performed in Banengo and Pollenzo sections (Piedmont basin, North Mediterranean) as well. The samples were analysed following the procedure described above. In Banengo section 6 samples were analysed (1 for each precessional cycle) for *S. abies* and *H. carteri*; in Pollenzo section 9 samples were analysed (1-2 for each precessional cycle) for *S. abies* and *H. carteri*. *Coccolithus pelagicus* and *U. rotula* were not analysed in the Piedmont Basin because their low abundance and poor preservation.

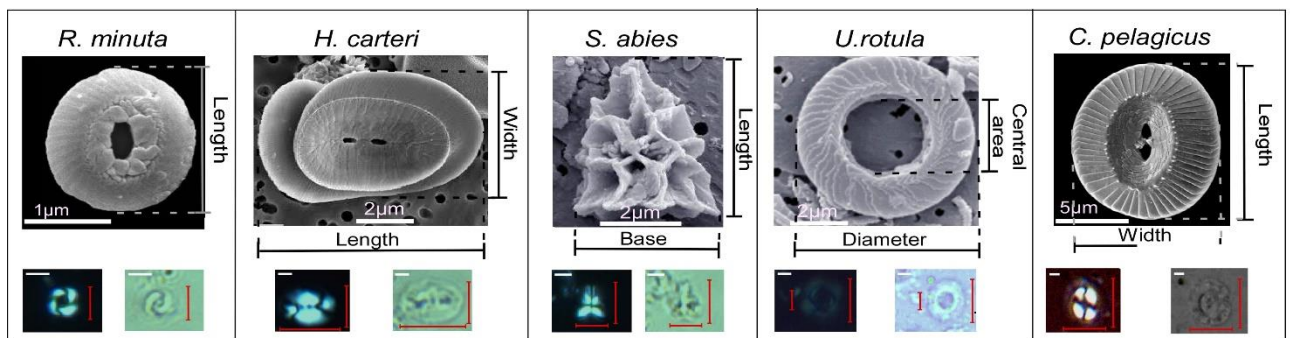


Fig. 2: Electron microscope photographs of the CN object of this study with the measured morphometrical parameters at the electronic microscope (above) and at the light microscope (below; the red lines represent the measured biometric parameter; scale bar is 2 µm). The electronic microscope pictures have been re-drawn and modified from Nannotax3 website

(<http://www.mikrotax.org/Nannotax3>) (courtesy of J. Young, P. Bown and L. Cros).

2.4 SYRACO: corrected length and calcification index

SYRACO is an automated system of coccoliths recognition developed by Beaufort and Dollfus (2004). In our study, SYRACO was used for the recognition and the measurement of the length and

the mass (Beaufort, 2006) of *R. minuta* coccolith. This analysis was performed for *R. minuta* because this taxon was the only present in all the analysed samples and was conducted in the Perales section only because this section spans a longer time interval, making possible to appreciate possible morphometry changes at the precessional scale. A certain amount of picture (at least 40, depending on the abundance of *R. minuta*) were taken with a SPOT insight camera mounted on a LEICA 6000B microscope with a x1000 magnification. A total of 97 samples were processed and a minimum of 200 *R. minuta* coccoliths were measured by SYRACO for each sample. In order to test the reliability of the SYRACO measures, 10 samples were selected for comparing the SYRACO results with a classical manual measurement at the light microscope. In each sample 100 *R. minuta* were identified and measured using the software ProGres 5. The obtained average values were successively processed in order to obtain the equation of the linear regression between SYRACO and the manual measurements (fig. 3a). The linear regression equation was successively used to correct the SYRACO-derived length in all the remaining samples (Fig. 3a). In order to have a comparable dataset, we used only the SYRACO measurements for the doubled measured parameters.

Reticulofenestra minuta calcification index was obtained following the protocol developed by D’Amario et al. (2018); dividing the mass values obtained from SYRACO by the normalized mass (density of calcite x coccolith volume). To calculate the coccolith volume, we multiplied the cube of the corrected length by K_s (estimated shape dependent constant). Unfortunately, the K_s values for *R. minuta* was never calculated (Young and Ziveri, 2000), so we choose to use the K_s calculated for *Gephyrocapsa oceanica* (0.05) that best approximate the shape of *R. minuta* (Young personal communication).

2.5 Statistical analysis

All the statistic treatments were performed using the software Past 4.03 (Hammer et al., 2001) and Excel. For each selected species, the average of the morphometric parameters, the deviation from the mean average (expressed in %), as well as the standard deviation were calculated.

One-way ANOVA (parametric ANalysis Of VAriance) test were performed in order to assess the degree of variance between the obtained means. The null hypothesis is that all the obtained means are the same and the encountered differences among the means are stochastic and not significant. In the case that ANOVA revealed significant differences ($p < 0.05$), a post-hoc Tukey HSD (Honestly Significant Difference) test was performed in order to identify which of the samples (or group of samples belonging to the same precessional cycle) differed. The correlation coefficient R^2 was calculated between the measured biometric parameters for all the analysed taxa in the 3 analysed sections. Finally, frequency histograms were performed for all the analysed taxa in order to assess which size class is more common in our dataset.

3-Results

Calcareous nannofossils are abundant and moderately/well preserved within the study interval and sections (for detail see the supplementary materials Fig. S1). The ANOVA test results recorded a significant size variation affecting our dataset in all the section studied for all the taxa considered. The Tukey HSD test identified where are located the samples and cycles which statistically differed (for detail see the supplementary materials Figs. S2 and S3). The target taxa concentration and morphometric data are shown in Figures 3, 4, 5, 6, 7 and 8 with key trends noted below.

3.1 *Helicosphaera carteri*

In the Perales section, *H. carteri* absolute abundances never exceed 0.40×10^9 CN/g, except in the cycles UA23, UA32 and UA34, where absolutes abundances from 0.55×10^9 to 1.35×10^9 CN/g were recorded (Fig. 4). *Helicosphaera carteri* length and width range from a minimum of $4.7 \mu\text{m}$ and $3.4 \mu\text{m}$ respectively, to a maximum of $11.0 \mu\text{m}$ and $7.9 \mu\text{m}$ (Fig. 3c) respectively. The average size of *H. carteri* shows maxima values in a cluster of samples in the cycle UA29; minima values are reached in the cycle UA34, where a statistically significant decrease from the mean average was recorded (Fig. 4 and

supplementary materials Fig. S2). The ellipticity index show higher values preferentially when the *H. carteri* width is below the average size. Highest ellipticity index values were recorded in the cycles UA23, UA24, UA26 and UA34 (Fig. 4). In the Banengo section, *H. carteri* length and width span from 6.1 μm to 12.1 μm and from 4.2 μm to 7.3 μm respectively (Fig. 5). The minimum average *H. carteri* size values are recorded during the MSC onset bioevent in concomitance with *H. carteri* peak in relative abundance (Fig. 6); the ellipticity index shows highest values in the cycles Bm2 and Bm5. In the Pollenzo section *H. carteri* length and width span from 4.27 μm to 11.7 μm and from 2.5 μm and 6.5 μm respectively (Fig. 5). The minimum *H. carteri* size value is recorded during the MSC onset bioevent in concomitance with *H. carteri* peak in relative abundance (Fig. 6), although sizes below the mean average were documented also in the 2 cycles before (UA32 and UA33) the MSC onset bioevent. In the Pollenzo section, after the MSC onset bioevent, *H. carteri* partially recovered its mean size which remains below the average mean size calculated in this site. The ellipticity index in the Pollenzo section shows an opposite trend compared to the other section, with minimum values during the MSC onset bioevent. Some differences emerged comparing the correlation coefficient (i.e. R^2), between the measured length, width and the ellipticity index (Fig. 3, Fig. 5 and supplementary material Fig S4). The correlation coefficient between length and width was higher in Perales section ($R^2 = 0.9154$) than in the Banengo ($R^2 = 0.5608$) and Pollenzo ($R^2 = 0.6731$) sections. These differences could be the results of the different amount of sample analysed and specimens measured. Furthermore, the analysed time interval in the 2 sections of the Piedmont Basin contain few precessional cycle before the MSC onset, which were characterized by unstable environmental conditions, likely resulting in a more variability of the measured biometric parameters.

3.2 *Sphenolithus abies*

In the Perales section, *S. abies* absolute abundance never exceeds the 0.5×10^9 CN/g, except in the cycle UA34 where the highest abundances are recorded (from 2.06×10^9 to 3.45×10^9 CN/g). As already observed for *H. carteri*, the 2 measured parameters (base and length) tend to increase

together although this relation seems to be less marked for *S. abies* ($R^2=0.5601$). *Sphenolithus abies* length and base span from 2.3 μm to 6.9 μm and 1.0 to and 5.7 μm respectively (Fig. 3e). The averages of *S. abies* lengths and base in the cycle UA34 show statistically significant decrease (Fig.4 and supplementary material Figs. S2, S3 and S5). More generally, a decreasing trend of the measured parameters is discernible from the cycle UA29 (where the maxima values are recorded) upward (Fig.4).

In the Banengo section *S. abies* base and length span from 1.8 μm to 5.9 μm , and 2.5 μm to 6.2 μm , respectively (Fig.5). It shows a decreasing trend of the average basal width from the bottom to the top (Fig.6). The minimum *S. abies* average value is recorded during the MSC onset bioevent, matching the *S. abies* peak in relative abundance (Fig.6).

In the Pollenzo section *S. abies* length and base span from 1.5 μm to 6.5 μm and 1.7 μm and 6.5 μm respectively (Fig.5); the minimum average value is recorded during the MSC onset bioevent, matching the *S. abies* peak in relative abundance (Fig.6). Above the MSC onset bioevent, *S. abies* shows size values below the average calculated in this site.

3.3 *Umbilicosphaera rotula*

Due to the rarity and poor preservation of *U. rotula* in the Piedmont Basin, it has only been possible to measure it consistently throughout the Perales section.

In the Perales section, *U. rotula* absolute abundance never exceed the 0.2×10^9 CN/g, except in the cycle UA24 (0.37×10^9 CN/g) and in the cycle UA34, where its maximum abundance was reached (1.12×10^9 CN/g) (Fig. 7). *Umbilicosphaera rotula* diameter and central area size span from a minimum 3.2 μm and 1.2 μm , to a maximum of 8.3 μm and 4.1 μm respectively (Fig. 3g). We found a large morphometric variability in *U. rotula*, with specimens showing heterogeneous central area/diameter index (Fig. 7). High *U. rotula* diameter size is recorded in the cycles UA23, UA28 and UA29; the lowest *U. rotula* diameter size is recorded in the cycle UA34, where a statistically significant decrease from the average recorded (Fig.7 and supplementary material Fig. S2). Likewise, the *S. abies* trend, a general decreasing trend of the *U. rotula* diameter is recognizable from UA29 onward with the exception of

UA32 where an increase in the diameter is observed. *Umbilicosphaera rotula* central area measurements show high values in the cycle UA23 and UA28, whereas minimum values are recorded in the cycle UA34.

3.4 *Coccolithus pelagicus*

In the Perales section, *C. pelagicus* absolute abundance is generally low (below 2.5×10^8 CN/g), with the exception of cycle UA34 where it increases up to 8.72×10^8 CN/g (Fig. 7). *Coccolithus pelagicus* length and width span from a minimum of 4.3 μm and 3.8 μm respectively, to a maximum of 14.3 μm and 13.4 μm respectively (Fig. 3i). The ellipticity index does not mark any significant variation, and slightly fluctuates close to the mean average (Fig. 7). The length and the width trends are well correlated ($R^2 = 0.7412$, Fig. 3i), showing maxima values from the bottom up to the cycle UA26. A slight increase in *C. pelagicus* length and width is also recognizable in the cycle UA34 (Fig. 7). Differently from the others analysed taxa, *C. pelagicus* does not show a size reduction in the UA34 but it retains size values that fluctuate around the mean average.

3.5 *Reticulofenestra minuta*

Reticulofenestra minuta is the main contributor to the total coccolith concentration as revealed by the CN absolute abundance (Fig.8). High absolute abundance of this taxon is recorded preferentially in the lower part of the studied section (UA23 and UA24) and in the last pre-evaporitic cycle (UA34), where *R. minuta* exceed the 1.5×10^9 CN/g.

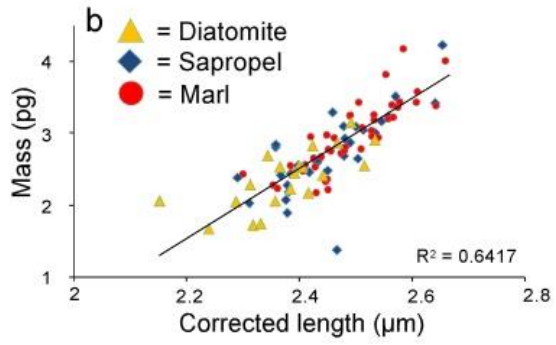
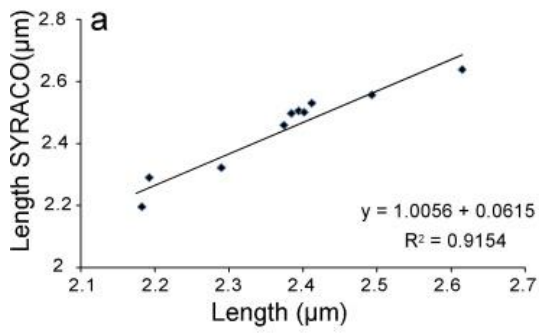
The average of the *R. minuta* length spans from 2.1 μm to 2.6 μm , with the lowest size and mass values recorded generally in the diatomite and the highest in the sapropel layers. The *R. minuta* length and mass are positively correlated ($R^2 = 0.6417$, Fig. 3b) and show a similar trend (Fig. 8). Differently, *R. minuta* calcification index is not correlated with the length and mass ($R^2 = 0.0265$ and $R^2 = 0.0276$, supplementary material Fig. S4). *Reticulofenestra minuta* mass shows a decreasing trend

from UA32 toward the MSC onset, with lowest value in the cycle UA34 where a statistically significant size decrease was recorded (Fig.7 and supplementary material Fig. S2).

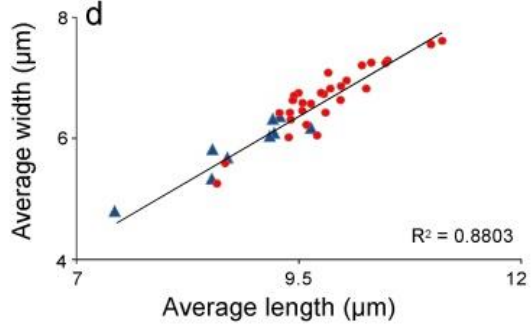
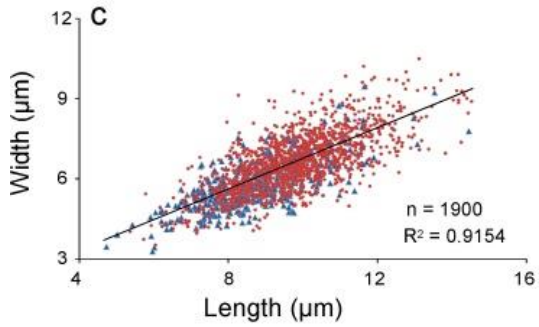
	<i>H. carteri</i>		<i>S. abies</i>		<i>U. rotula</i>		<i>C. pelagicus</i>		<i>R. minuta</i>	
	Length	Width	Length	Base	Diameter	Central area	Length	Width	Length	*Mass (pg)
Perales	9.57 ± 1.48	6.47 ± 0.91	4.10 ± 0.74	3.37 ± 0.61	5.39 ± 0.65	2.7 ± 0.32	9.5 ± 1.47	7.3 ± 1.39	2.45 ± 0.09	2.76 ± 0.54
Pollenzo	7.79 ± 1.30	4.89 ± 0.75	4.08 ± 0.79	3.51 ± 0.63	/	/	/	/	/	/
Banengo	8.99 ± 1.09	5.80 ± 0.73	4.16 ± 0.71	3.59 ± 0.58	/	/	/	/	/	/

Table 1: Mean average value expressed in μm (*except the mass, that is expressed in pg) of the measured biometric parameter (dark) with the calculated standard deviation (red) for every taxa analysed in the different section

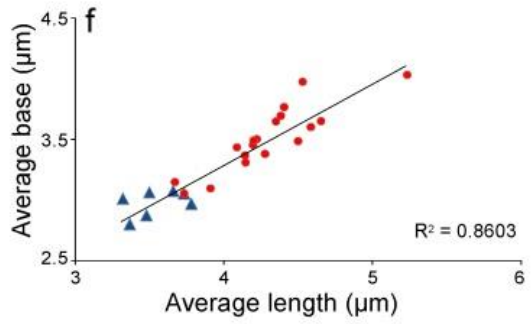
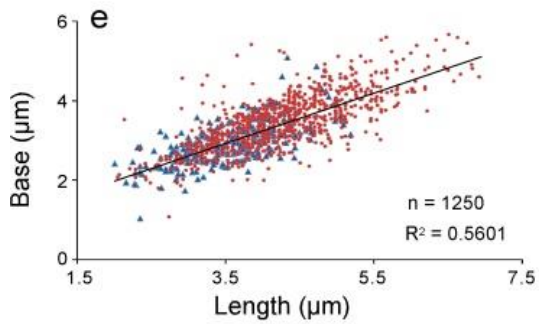
R. minuta



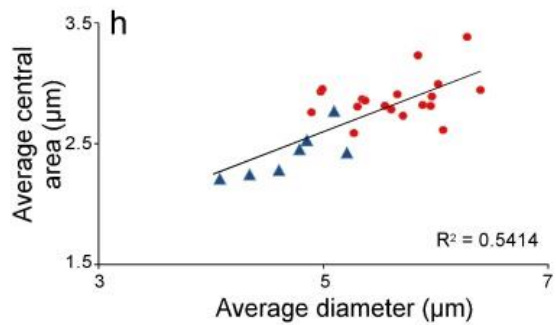
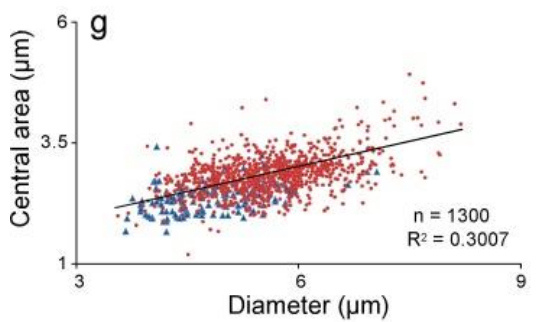
H. carteri



S. abies



U. rotula



C. pelagicus

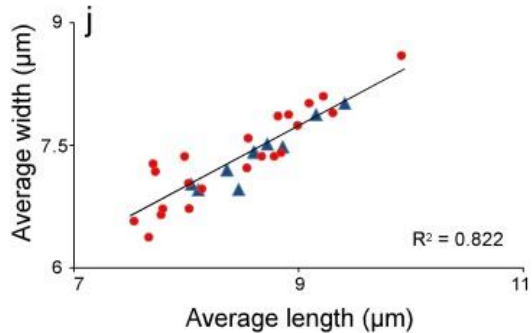
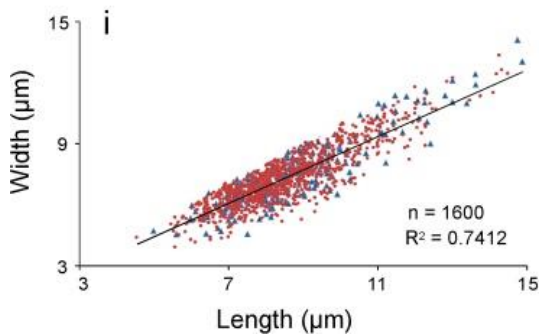


Fig. 3: Relationship between the morphometrical parameters measured for each CN taxa (Perales section, Sorbas Basin).

a): Relationship between the average *R. minuta* length obtained using SYRACO and with an operator. The obtained linear regression equation has been successively used to correct the data obtained from SYRACO (see 2.4 paragraph). b):

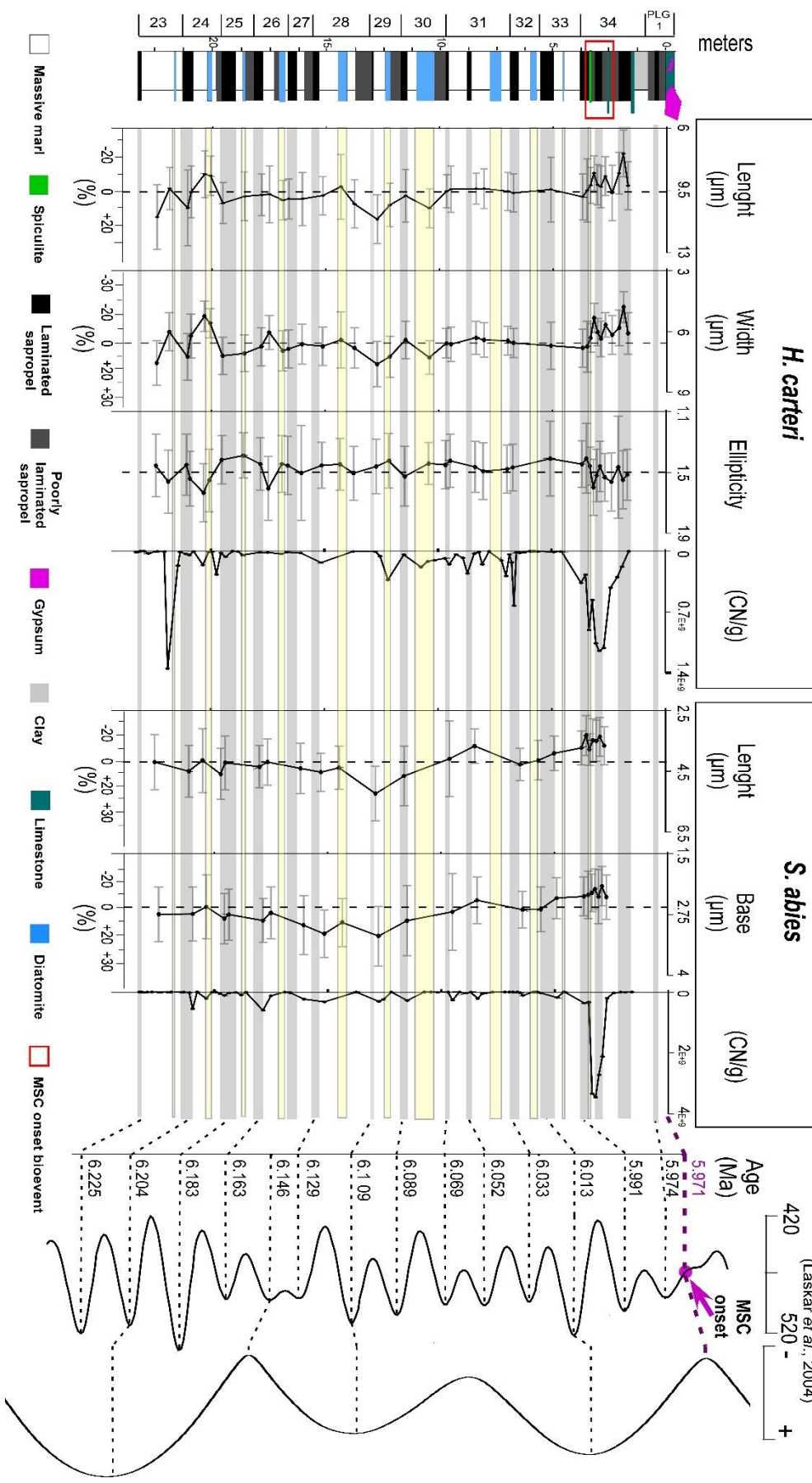
Relationship between the average *R. minuta* corrected length and the average mass for each lithology of the Perales section.

The R^2 value was calculated considering the entire dataset (triangle + cycle + diamond).

c, e, g, i): Relationship between the morphometrical parameters for each selected taxa, where n is the number of measured CN, the blue triangles represent the size during the MSC-CN bioevent and the red cycles the size in the remaining part of the section. The R^2 value was calculated considering the entire dataset (triangle + circle).

d, f, h, j) Relationship between the average length or diameter and the average width, base or central area. Blue triangles mark the CN average size during the MSC-CN bioevent, the red circles the average size in the remaining part of the section.

The R^2 value was calculated considering the entire dataset (triangle + circle).



Summer insolation 65°N (W/m^2),
 Eccentricity index
 (Laskar et al., 2004)

Fig. 4: *Helicosphaera carteri* and *S. abies* biometric measurements and absolute abundances in the Perales section compared with the change in orbital parameters (precession and eccentricity from Laskar et al., 2004). The error bars represent the standard deviation. The dashed line represents the mean average, the lower axis shows the variation expressed in % from the mean average. The red rectangle indicates the position of the MSC onset bioevent (Mancini et al., 2020).

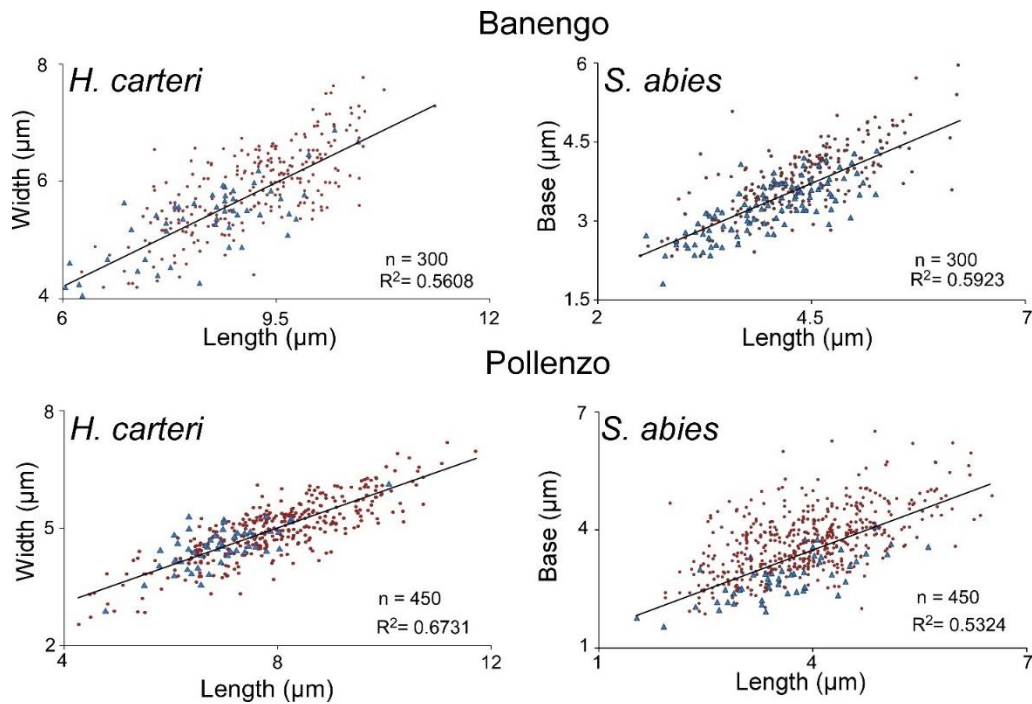
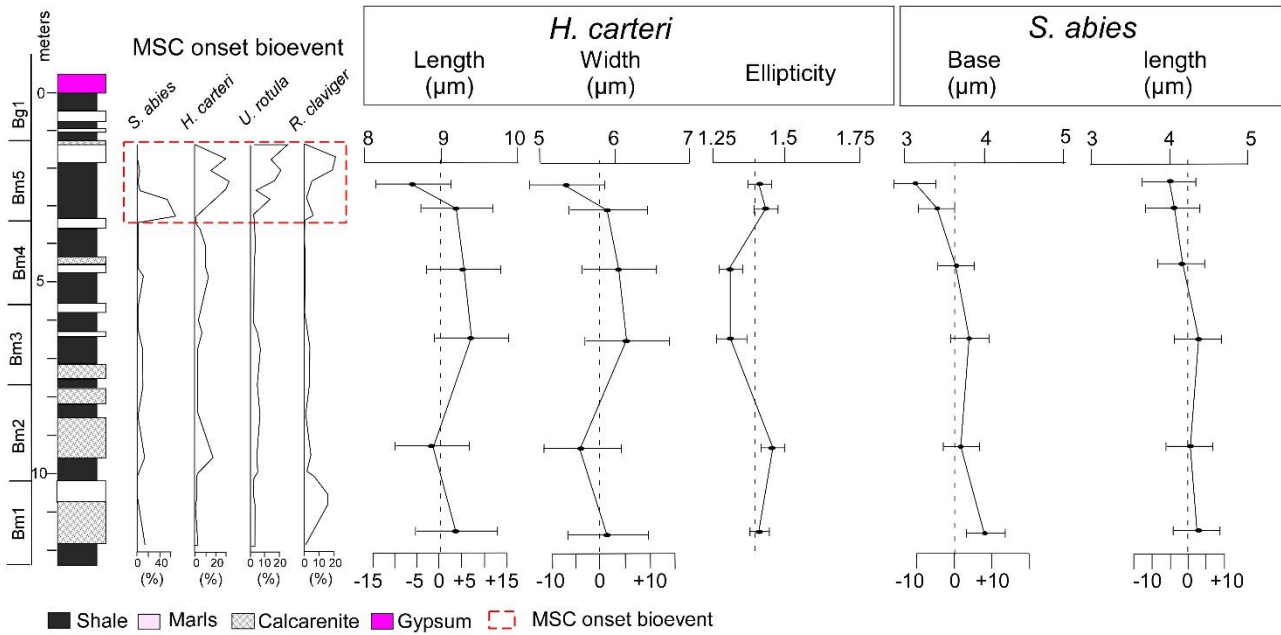


Fig. 5: Relationship between the morphometrical parameters measured for *H. carteri* and *S. abies* (Banengo and Pollenzo sections, Piedmont Basin), where n is the number of measured coccoliths, the blue triangles represent the size during the MSC-CN bioevent and the red circles the size in the remaining part of the section. The R^2 value was calculated considering the entire dataset (triangle + circle).

Banengo



Pollenzo

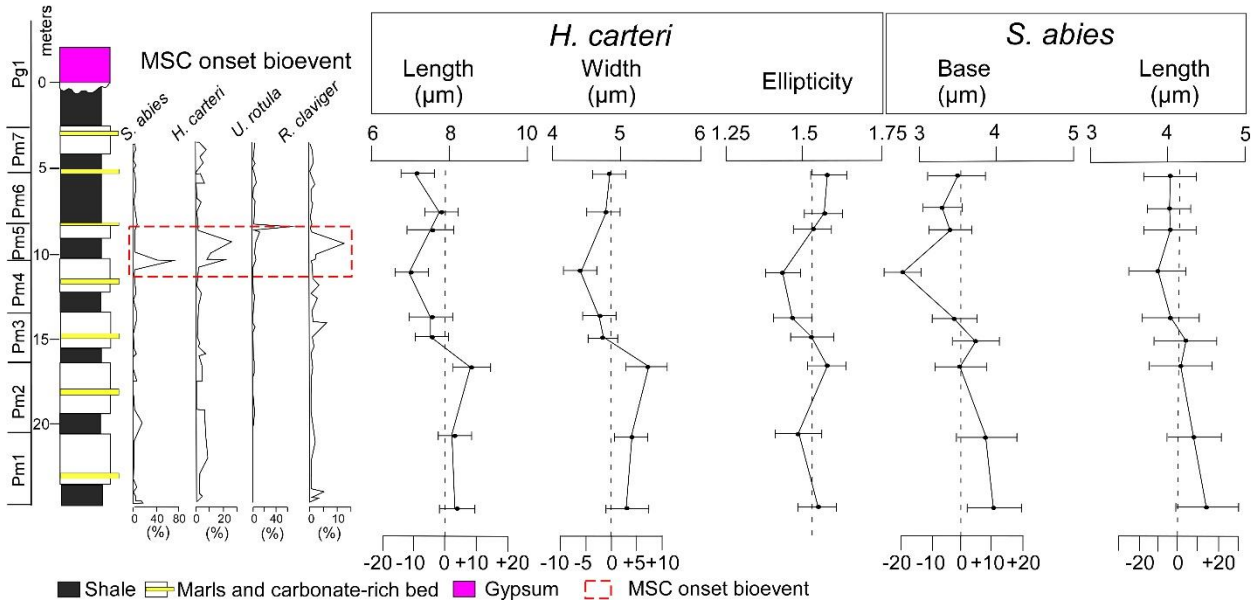
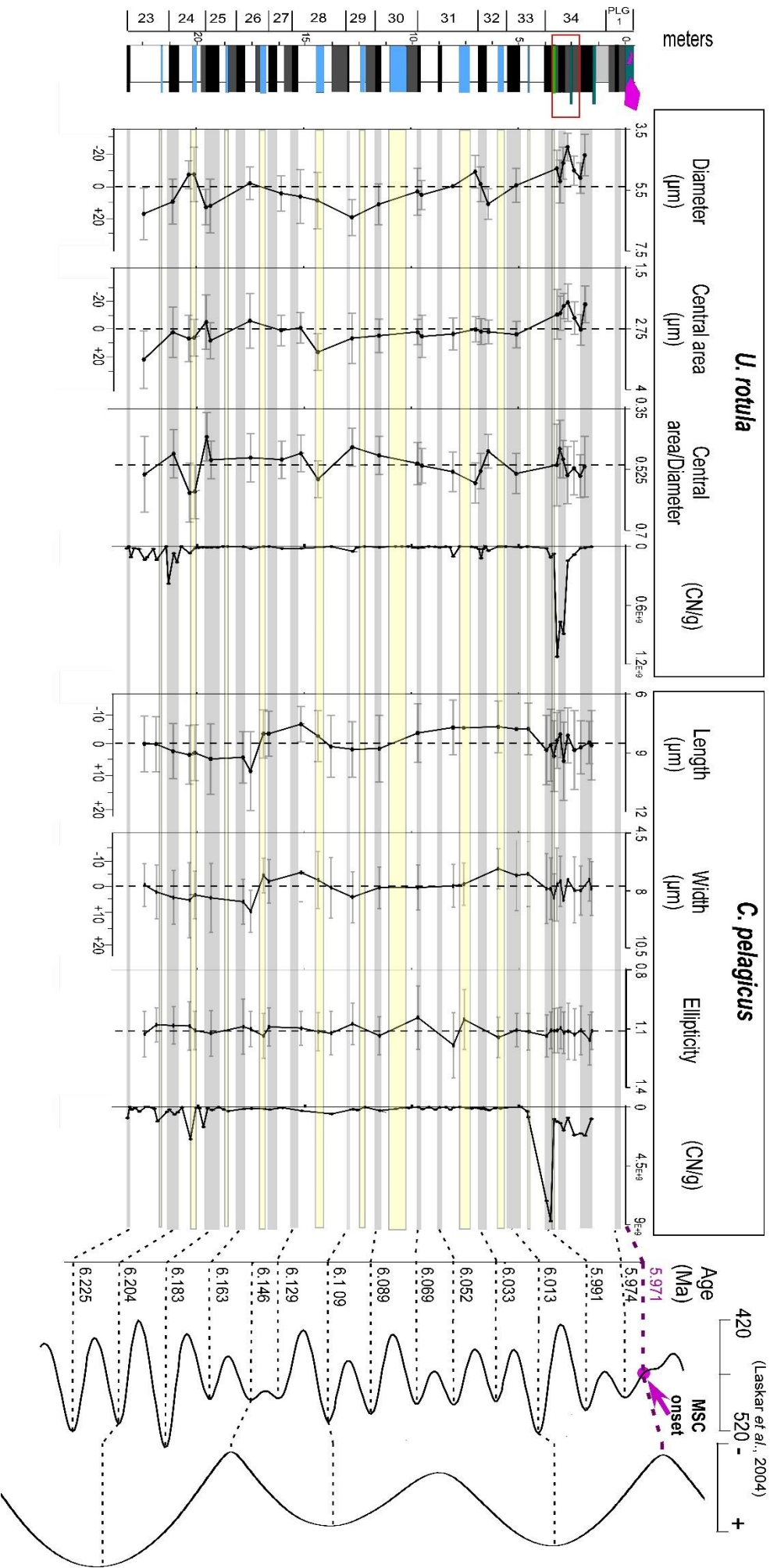


Fig. 6: *Helicosphaera carteri* and *S. abies* biometric measurements in the Banengo and Pollenzo sections (Piedmont Basin) compared with the relative abundance of the species involved in the MSC onset bioevent. The error bars represent the standard deviation. The dashed line represents the mean average, the lower axis shows the variation expressed in % from the mean average.



Summer insolation 65°N (W/m²),
Eccentricity index
(Laskar et al., 2004)

420 520
MSC onset

Age (Ma)
5.991
5.974
5.971
6.013
6.033
6.052
6.069
6.089
6.109
6.129
6.146
6.163
6.183
6.204
6.225

Fig. 7: *Umbilicosphaera rotula* and *C. pelagicus* biometric measurements and absolute abundances in the Perales section compared with the change in orbital parameters (precession and eccentricity from Laskar et al., 2004). The error bars represent the standard deviation. The dashed line represents the mean average, the lower axis shows the variation expressed in % from the mean average. The red rectangle indicates the position of the MSC onset bioevent (Mancini et al., 2020). Legend as in Fig. 4.

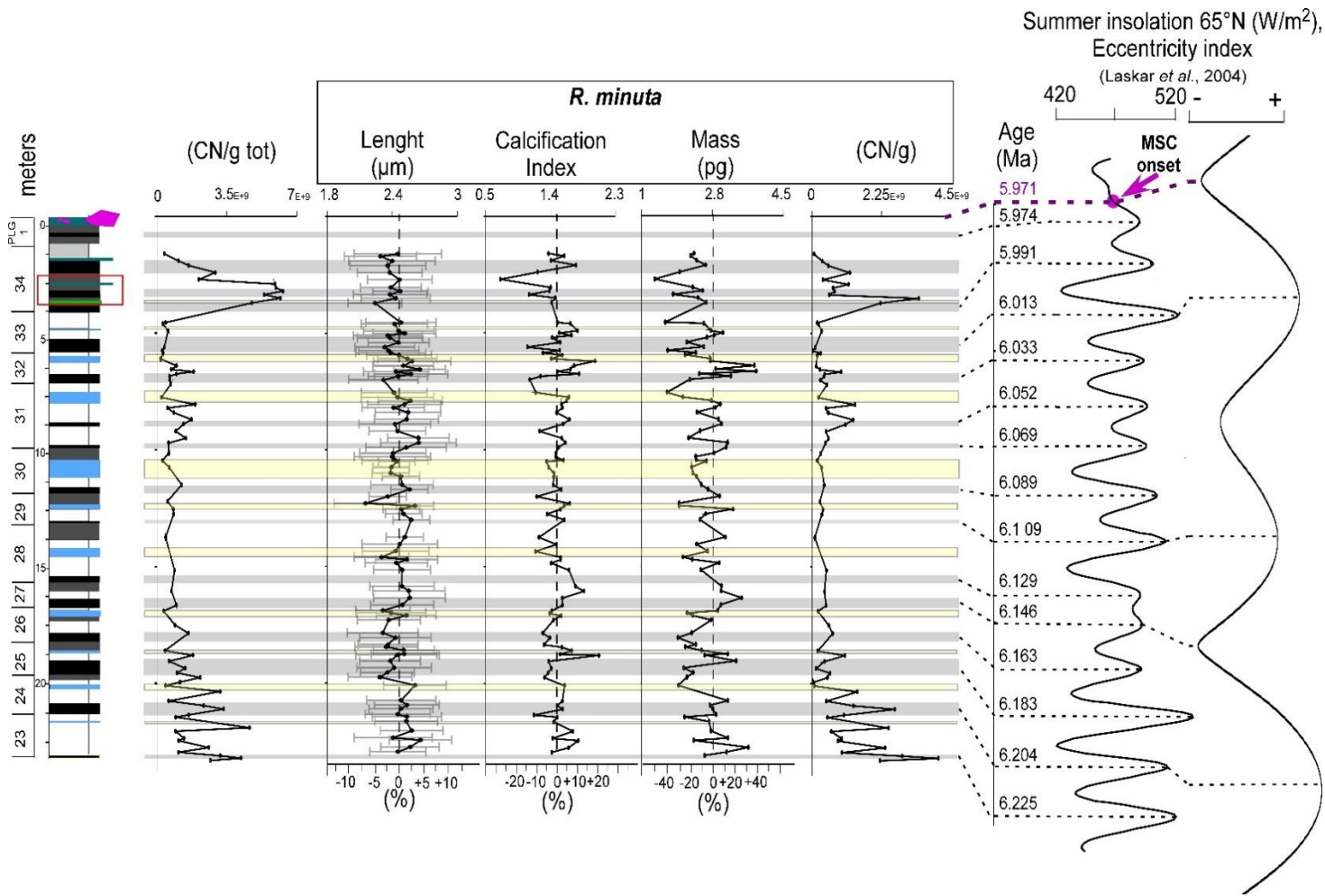


Fig. 8: *Reticulofenestra minuta* biometric measurement and absolute abundance in the Perales section compared with the change in orbital parameters (precession and eccentricity from Laskar et al., 2004). The error bars represent the standard deviation. The dashed line represents the mean average, the lower axis shows the variation expressed in % from the mean average. The red rectangle indicates the position of the MSC onset bioevent (Mancini et al., 2020). Legend as in Fig. 4.

4- DISCUSSION

4.1 Size decrease during MSC onset bioevent and productivity change

As revealed by the ANOVA and Tukey HSD test (supplementary materials Figs. S2 and S3) a statistically relevant size decreases affected *H. carteri*, *S. abies* and *U. rotula* (*U. rotula* was tested in the Perales sections only), concomitant with an increase in CN absolute abundance recorded in the cycle UA34 (Figs. 4, 6 and 7). Calcareous nannofossils absolute abundance in the sedimentary record is extensively used to track changes in CN productivity through the geological past (Flores et al., 1997; López-Otálvaro et al., 2008; Browning et al., 2008; Gibbs et al., 2018). We excluded that the recorded increase in CN absolute abundance was due to a concentration factor as a result of a slowdown of the sedimentation rate, because the precessional cycle bearing the MSC onset bioevent in the Perales section is roughly twice as thick as compared with the other UA cycles. It can be inferred that the increased CN absolute abundance concomitant with a size reduction is not related to the slowdown of the sedimentation rate but represents a primary signal, thus indicating an increase in the calcareous nanoplankton productivity.

In our study, the recorded size reduction took place during a very peculiar event characterized by a distinct fossil signal approximating the MSC onset in several Mediterranean successions (Lozar et al., 2018; Gennari et al., 2018; Lozar and Negri et al., 2019; Mancini et al., 2020). This event was firstly identified by Lozar et al. (2018) and described as a succession of CN peak in abundance of the species *S. abies*, *H. carteri*, *U. rotula* and *R. claviger*. This event was recently named MSC onset bioevent (Mancini et al., 2020), and marks the last restriction pulse affecting the Mediterranean Basin and triggering the MSC onset (Mancini et al., 2020). The decreased water exchange between the Mediterranean Sea and the Atlantic Ocean increased the sensitivity of the Mediterranean Sea to continental runoff and associated nutrient supply into the basin, ultimately resulting in enhanced marine productivity (Mancini et al., 2020). A further outcome of this study is the possibility to use the CN size reduction as a biostratigraphic signal in those sections in which it is masked by the cyclical peaks of the species involved in the MSC onset bioevent (*e.g.* Tokhni section, Gennari et al., 2018; Perales section, Mancini et al., 2020). However, several samples encompassing several precessional

cycle needed to be analysed in order to discern the size variation during the MSC onset bioevent, since the recorded absolute values of the CN sizes is not comparable between the 3 sections studied.

High CN absolute abundances are also recorded in the cycles UA23 and UA24, (4.64×10^9 CN/g and 3.54×10^9 CN/g respectively (Fig. 8), but not associated with noticeable size decreases. This suggests either that the CN growth rate alone was likely not high enough for driving any relevant size change, or the mechanisms leading to size reduction are likely associated with the triggering factors inducing the enhanced CN productivity. Therefore, we hypothesized that the CN size decrease concomitant with high CN abundance recorded during the MSC onset bioevent could be linked to the enhanced fresh-water influence delivering nutrients and the associated changes in the water column structure. Differently, in the lower UA23 and UA24 cycles, indication of important freshwater input was not recorded, and the CN high abundance encountered in these cycles could be explained as a result of a diminished sedimentation rate resulting in highest concentration of CN in the bulk sediment. From this observation, it could be inferred that the enhanced freshwater input and the associated changes in the water column structure, turbidity and nutrients delivery are the primary candidates for explain the CN size reduction accompanying the MSC onset. Since the increase in water turbidity cannot explain high CN absolute abundance, we infer that the nutrient delivery may have had the primary control on the CN size reduction. In the Eastern Mediterranean, Karakitsios et al (2017) show a sharp freshwater input occurring at 1.651 Ma evidenced by *H. carteri*, *C. leptoporus*, *U. jafari*, *R. haqii* and *Reticulofenestra minutula*; this event was probably related to the open gateway with the Parathetys at the Meotian/Pontian boundary, (see also Gennari et al. 2018) but no evidence of such freshening has been detected further West in the Sorbas basin.

The relationship between the nutrient regime and coccolithophores size was highlighted by some culture experiments, in which the taxa *C. leptoporus*, *C. quadriperforatus*, *H. carteri* and *Emiliana huxleyi* show that during the exponential growth phase, characterized by a rapid cell division rate, small cells (characterized by a low number of interlocking coccoliths) are produced (Gibbs et al., 2006; Gibbs et al., 2013; Šupraha et al., 2015; Sheward et al., 2017). Conversely, larger cells (with

higher number of coccoliths) are produced during slow cell division (Gibbs et al., 2013; Sheward et al., 2017). Taking into account that a correlation could exist between the coccosphere size, the number of coccoliths covering the cell and the coccoliths size (Hendericks et al., 2007; Gibbs et al., 2013; Aloisi, 2015), an assessment of the cell division rate can be inferred from morphometrical changes measured on the coccoliths, as already performed by Gibbs et al. (2013; 2018) in the sediments straddling the Paleocene-Eocene thermal maximum (PETM). The size reduction affecting *H. carteri*, *S. abies* and *U. rotula*, and the highest CN productivity recorded, could be the results of rapid cell division, occurred during period of excess nutrient availability and favourable water column structure (e.g. it was reconstructed that *S. abies* exploited nutrients in the deep photic zone when thermal stratification occurred, Flores et al., 2005; Mancini et al., 2020). In our study, similar morphometric changes were not observed in *C. pelagicus*, which is in line with the culture experiments that showed no significant coccolith size change related to experimental conditions (*i.e.* stationary growth phase vs. exponential growth phase; Gibbs et al 2013; Sheward et al., 2017). However, draw a parallel between the fossil record and the laboratory experiments could be rather speculative, since some taxa considered in our study are extinct and the coccolithophores response to the environmental variables could be strain-specific, as demonstrated for *C. pelagicus* (Henderiks and Rickaby, 2007; Gibbs et al 2013; Sheward et al., 2017). Differently from other coccolithophore taxa, *C. pelagicus* morphology was not affected also during the PETM, likely because of its insensibility to the broad $p\text{CO}_2$ variation that characterized this event (Henderiks and Rickaby, 2007).

Therefore, we infer that during the MSC CN bioevent, *S. abies*, *H. carteri* and *U. rotula* shifted to more r-selected strategy, by increasing their cell division rate to exploit nutrients during seasonal favourable conditions. This resulted in a size decrease and in an increase in CN absolute abundance (Fig. 8).

In other geological case histories, the CN size reduction is often reported to be related to “stressed” conditions (Faucher et al., 2017b) and the CN size increase with stable conditions (Ferreira et al., 2017). However, our results show that the CN size reduction occurred during period

characterized by high CN productivity, thus indicating optimal environmental condition for calcareous nannoplankton to growth rather than stressed, at least during the MSC onset bioevent. Relevant size decreases were recorded during Oceanic Anoxic Events (Lübke and Mutterlose, 2016; Erba et al., 2010; Faucher et al., 2017b) in relation with abrupt increase in CO₂ emissions (and the consequent pH decrease in surface water) (Erba et al., 2010), toxic metal increase (Faucher et al., 2017a), or with an increase in continental runoff and the associated increase in water turbidity (Lübke and Mutterlose, 2016). Generally, the amplitude of the CN size reduction during the OAEs is comparable to that recorded during the MSC CN bioevent (Erba et al., 2019).

After the MSC onset, the CN productivity gradually decreased and the CN size (*H. carteri*, *S. abies* and *U. rotula*) oscillates without reaching the previous size average. The basin restriction occurring during the MSC CN bioevent amplified the sensitivity of the Mediterranean Basin to external forces, such as temperature change, freshwater input, and nutrient delivery (Mancini et al., 2020). This ultimately may have resulted in an increased environmental variability, which could fall within the definition of “stressed” conditions. An attempt of comparison between the paleoenvironment straddling the MSC with actual analogue could be provided by modern lagoon environments (*e.g.* in the Términos Lagoon, SE Gulf of Mexico), in which strong changes in salinity, productivity and turbidity occurred in response mainly to seasonal change in the freshwater input (Yáñez-Arancibia and Day 2005; Poot-Delgado et al., 2015). Coccolithophores were recorded in some lagoon environments (Sakka et al., 1999; Poot-Delgado et al., 2015) showing distribution pattern according mainly to seasonal variations (Poot-Delgado et al., 2015). Therefore, it could be inferred that after the MSC onset bioevent, calcareous nannoplankton were likely affected by strong environmental variability because of the increased basin restriction; they were forced to increase the cell division rate to face and survive the rapid development of hostile environmental conditions, such as rapid and extreme changes in salinity and nutrient delivery.

In our studied sections, the MSC onset bioevent is accompanied by the disappearance of normal size planktic foraminifers (> 125 µm; Violanti et al., 2013; Lozar et al., 2018); the assemblage

is dominated by dwarf foraminifers in the 43-125 μm size fraction (Fig. 9). The record of dwarf planktic foraminifers during the MSC interval was already reported in cores and land sections (Cita et al., 1978; Hsü et al., 1978; Van de Poel, 1992; Riding et al., 1998; Iaccarino and Bossio, 1999; Fortuin and Krijgsman, 2003; Braga et al., 2006), and interpreted as the result of “stressed” or “anomalous” water column condition (Boltovskoy and Wright, 1976; Corbì et al., 2016), although some authors suggested that dwarf planktonic foraminifers were symptomatic of high nutrients input (van de Poel, 1992; Kaiho et al., 2006). We suggest that the anomalous or stressed conditions were likely related to the restriction of the Mediterranean Basin, that resulted in an increase in the environmental variability (e.g. increase in the freshwater input and the associated nutrients delivery) which forced also the foraminifers to complete their life cycle faster and hence, to reduce their size (Fig. 9).

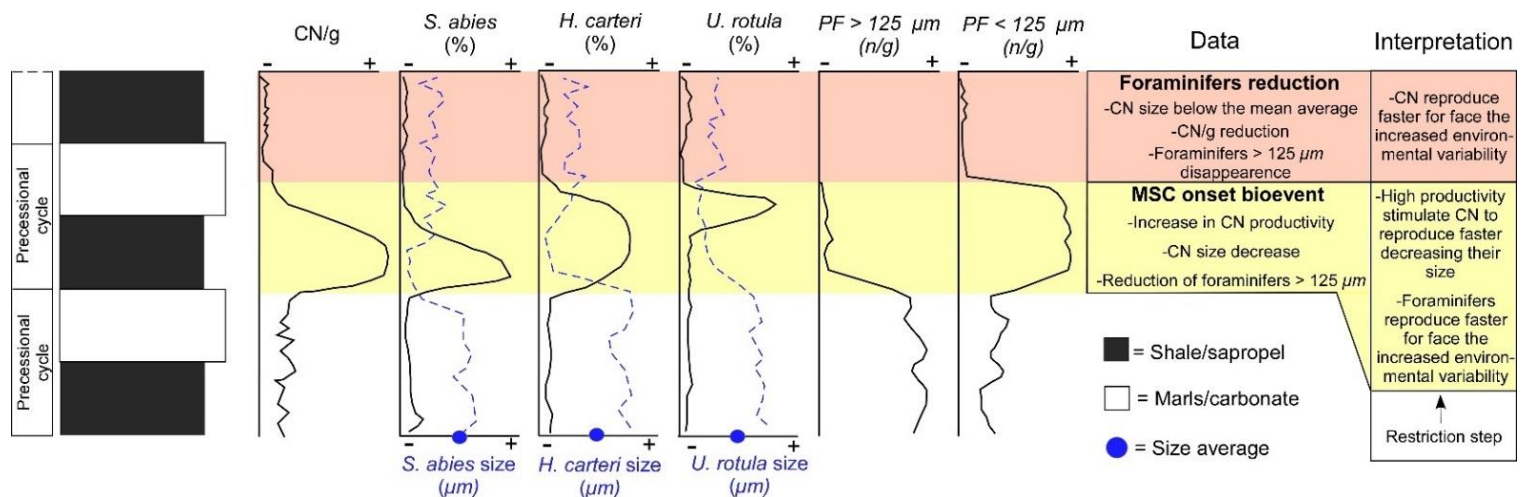


Fig. 9: Schematic representation that summarize the CN size and abundance and foraminifer size fraction fluctuations accompanying the MSC onset bioevent in the 3 studied sections (see 4.1 for explanation)

4.2 *Reticulofenestra minuta* size as a tracer for precessional variability

Very little is known about how orbital forcing affects climate and environmental change and how this is linked to coccolithophore size. Suchéras-Marx et al. (2010) highlight the relevance of orbital-controlled environmental factors influencing CN morphometric parameters. To test this hypothesis, our analysis was restricted to *R. minuta*, which dominated the assemblage throughout the studied interval.

Our results reveal a good correlation between *R. minuta* size and mass and the lithological changes of the sedimentary quadripartite cycle (Fig. 3b), deposited under precessional control (Sierro et al., 2003). *Reticulofenestra minuta* shows minimum in the average length and mass during diatomite deposition (Figs. 3b and 8). Diatomites were deposited in an environment characterized by strong seasonality, with enhanced runoff inducing stratification during humid phases and vigorous vertical mixing during drier phases (Mancini et al., 2020). Conversely, higher mass and larger size values are recorded in the upper part of the sapropel layers (Figs. 3b and 8).

From cycle UA31 toward the MSC onset, the mass of *R. minuta* shows higher fluctuation amplitude with the tendency toward lower values (Fig. 8), likely reflecting an increase in the environmental variability at the precessional scale, that could be attributed to the restriction step occurred at ~6.03 Ma and recorded in the nearby Bajo Segura Basin (Corbì et al., 2020) and in the whole Mediterranean approximately at the same time (Kouwenhoven et al., 2006; Gennari et al., 2018). The same response was recorded in the foraminiferal diversity index and on the benthic foraminiferal absolute abundance in the Perales section (Sierro et al., 2003), marking an increase in the environmental instability toward the MSC onset. In this framework, it is reasonable inferring that the drivers of the *R. minuta* size decrease relate to unstable environmental condition that occurred within an annual cycle, leading *R. minuta* to reproduce faster to face the unstable environmental condition during the diatomite deposition and toward the MSC onset. On the opposite, *R. minuta* size and mass show higher value in the upper part of the sapropel partitioning, where the available proxies point to a stable and strongly stratified water column (Mancini et al., 2020).

4.3 The possible role of $p\text{CO}_2$ on calcareous nannoplankton size

In recent years, many studies focused on the calcareous nannoplankton response to the ongoing ocean acidification and warming (Langer et al., 2006; Iglesias-Rodriguez et al., 2008; Zondervan, 2007; Meyer and Riebesell, 2015; Langer et al., 2009), caused by substantial accumulation of anthropogenic CO_2 emissions in the atmosphere (LaQuèere et al., 2017), and the consequent impact

on the biological carbon pump (Rost and Riebesell, 2004; Ziveri et al., 2007). The geological record offers many opportunities to study rapid environmental perturbations and their impact on the biota. For instances the Paleocene-Eocene Thermal Maximum (PETM) is often compared to the current anthropogenic climate change, although the rate of CO₂ emission is several times lower compared to the present scenarios (Zeebe et al., 2016).

The late Miocene was characterized by a rapid decline in the global sea surface temperature (6°C between 30°-60° N within 7.5 - 5.5 Ma; Herbert et al., 2016), likely related to the decrease in *p*CO₂ inferred from the stable isotopes of coccolithophores and changes in the global vegetation covering (Bolton and Stoll, 2013; Bolton et al., 2016; Herbert et al., 2016). Recent studies underline the relevance of the MSC on the decline in CO₂ content occurring during the late Miocene, as the result of limited water exchange between the Mediterranean Sea and the Atlantic Ocean (Capella et al., 2019). Interestingly, we noted that the late Miocene cooling trend (Herbert et al., 2016) fits with the Coccolithophore Assemblage Size (CAS, Hermann and Theirstein, 2012) and with the onset of the MSC (Fig. 10). Henderiks and Pagani (2008) speculate that the shift toward smaller size of the reticulofenestrads during the Oligocene reflects an adaptive response to a decrease in *p*CO₂. However, this physiological adaptation to *p*CO₂ fluctuations is species specific and for instance did not affected *C. pelagicus* (Hendericks and Rickaby, 2007; Gibbs et al., 2013). The size reduction affecting some selected species during the MSC CN bioevent occurred abruptly, does not fit the gradual decrease in temperature (and *p*CO₂) inferred from late Miocene records (Herbert et al., 2016). Moreover, the calculated sea surface temperature in the East Mediterranean during the Messinian (from 6.45 Ma to 5.97 Ma) did not reveals any cooling trend toward the MSC onset (Vasiliev et al., 2019). Consequently, the size reduction during the MSC onset bioevent was likely not directly related to the ongoing global decrease in temperature and *p*CO₂. Differently, the cyclical *R. minuta* size and mass fluctuation could be related with precession-induced *p*CO₂ variability, but this inference remains speculative, because of the scarcity of knowledge regarding the *p*CO₂ trend and its variability at the precessional scale throughout the late Miocene.

Although the trigger for the CN size reduction during MSC CN bioevent was likely related to local environmental changes, further efforts are necessary to better understand the sparse but striking data regarding the correlation within CN size, $p\text{CO}_2$ and MSC onset.

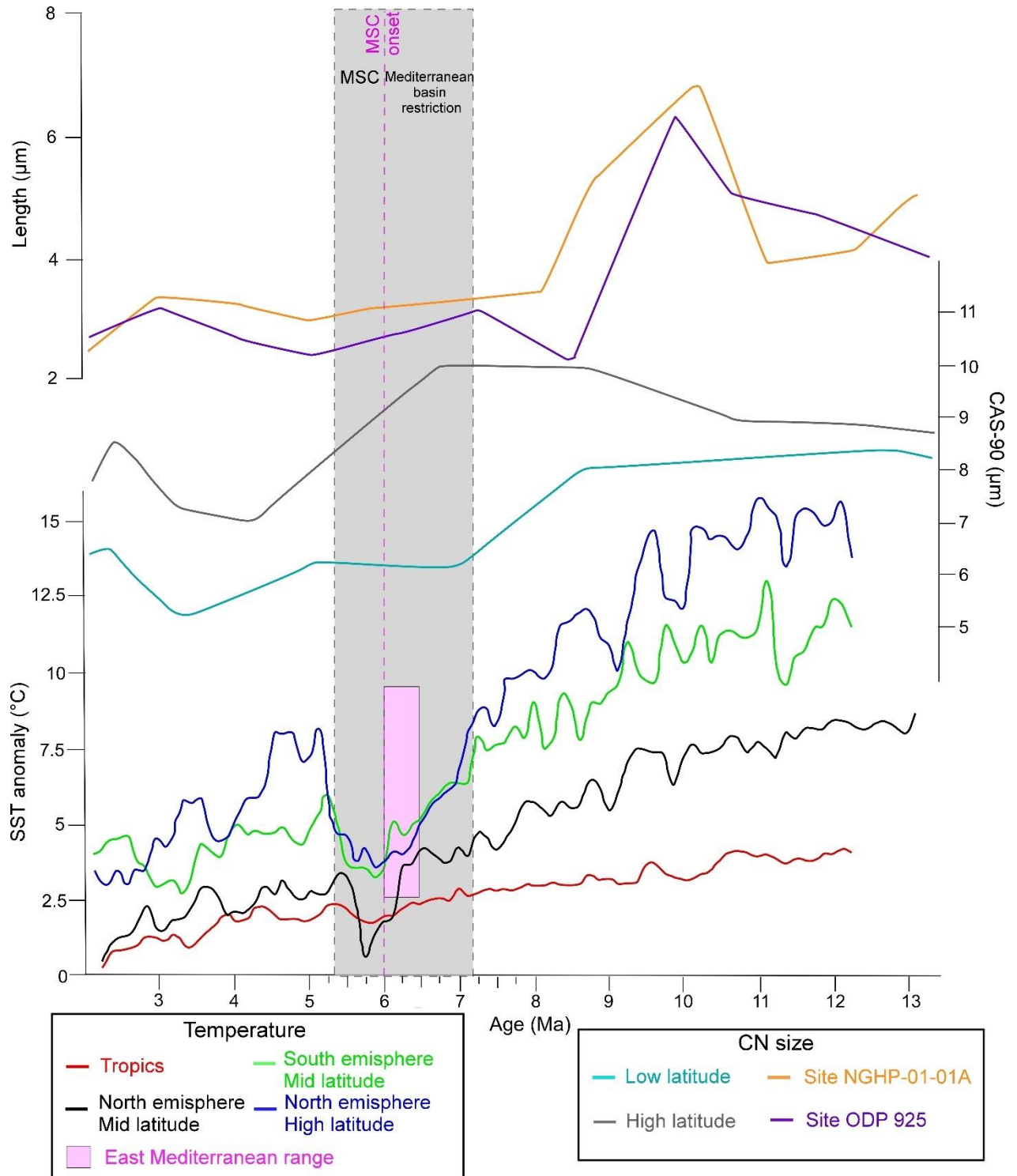


Fig. 10: Sea surface temperature evolution based on alkenone record over the late Miocene and Pliocene (Herbert et al., 2016; Vasiliev et al., 2019) compared with the 90th percentile of Coccoliths Assemblage Size (CAS-90) (Hermann and Thierstein, 2012) and the Noëlaerhabdaceae coccolith length (Bolton et al., 2016). The grey rectangle marks the period of the Mediterranean Basin restriction and of the MSC (Capella et al., 2019). The blue line represents the temperature evolution at high latitudes (> 50°N) in the North hemisphere; the green line represents the temperature evolution at mid latitudes (30°-50°S) in the South hemisphere; the black line represents the temperature evolution at mid latitudes (30°-50°N) in the North hemisphere; the red line represents the temperature evolution at the tropics (Herbert et al., 2016). The violet rectangle represents the East Mediterranean sea surface temperature range (Vasiliev et al., 2019). The cyan and the grey lines represent the means of CAS-90 evolution at the low latitudes (< 45°) and at high latitudes (> 45°). The orange and the violet lines represent the Noëlaerhabdaceae coccolith length measured at the site NGHP 01-01A (Indian Ocean) and at the ODP site 925 (Atlantic Ocean), respectively. Data from Herbert et al., 2016; Hermann and Thierstein, 2012 and Bolton et al., 2016; re drawn after Herbert et al., 2016 and Bolton et al., 2016.

Conclusion

Calcareous nannofossil biometry and absolute abundance analyses were performed in the Sorbas Basin (Perales section) and in the Piedmont Basin (Banengo and Pollenzo sections) in order to highlight the impact of the MSC onset on marine organisms and ultimately decipher the paleoenvironmental dynamics spanning this time interval.

An increase in the CN absolute abundance, concomitant with a size decrease of *H. carteri*, *S. abies* and *U. rotula* was recorded at the time of the MSC onset bioevent. These morphometric changes are in the same order of magnitude of those reported during major environmental perturbations during Earth history. These size reductions were likely related to an increase in calcareous nanoplankton productivity that led to selected calcareous nanoplankton taxa to increase the overall growth rate and decreasing their size, as supported by laboratory culture experiments. Calcareous nanoplankton productivity was triggered by a restriction pulse affecting the Atlantic-Mediterranean gateway that increased the continental run-off and the associated nutrient delivery influence in the Mediterranean Sea. After the MSC onset bioevent, the analysed taxa did not recover their normal size, and their mean size always fluctuated below the mean average, in parallel with a drastic reduction of

CN absolute abundance. In this case, dwarf CN are symptomatic of a highly variable environment, comparable with actual lagoonal system in which the environmental parameters are strongly modulated by the freshwater input.

Our analysis also reveals that *R. minuta* size and mass cyclically fluctuate miming the precession curve, revealing that such size decrease occurs during time interval characterized by strong seasonal variability, corresponding to the diatomite layer in the Perales section. The *R. minuta* size and mass fluctuation amplitude increases from ~ 6.03 toward the MSC onset, where it shows the lowest values. Also in this case, smaller CN were related to unstable water column conditions, which forced CN (and foraminifers, toward the MSC onset) to reproduce faster and decrease their size to face the unstable environmental conditions.

The influence of the gradual global decline of $p\text{CO}_2$, characterizing the Messinian, was not responsible for the size reduction recorded during the MSC onset bioevent, although a possible role governing the size variability of *R. minuta* at the precessional scale cannot completely be discarded.

Supplementary material

Preservation issues and statistical analyses

Introduction

In this document we detailed the preservation issue encountered during the analysis phase with a plate showing different preservation degree affecting CN. We also listed the statistical analysis results.

1- Preservation

The CN in our samples were generally moderately/well preserved. *Reticulofenestra minuta* and *S. abies* are very resistant to dissolution processes (Gibbs et al., 2004) and were generally excellently preserved. The other species analysed in our study were more subject to dissolution and

overgrowth; these features hampered the biometrical investigation in few samples coming from both Sorbas and Piedmont Basins. The poorly preserved specimens are preferentially located in the last (1 or 2) precessional cycle before the MSC onset.

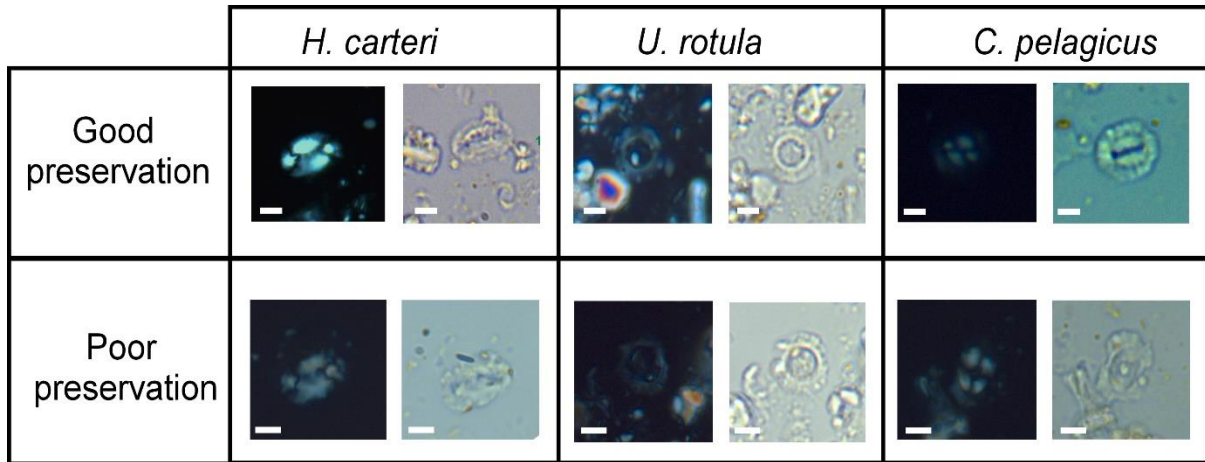


Fig.S1: Optical microscope photographs of some CN taxa analysed in our study showing different degree of preservation.

2- Statistic analysis results

2.1 ANOVA and Tukey test

The one-way ANOVA test applied for all the taxa measured in all the 3 sections studied, revealed a statistically significant difference among both the analysed samples and cycles. In the following part the Tukey HSD test results are listed.

Length

R. minuta

Mass

	UA34	UA33	UA32	UA31	UA30	UA29	UA28	UA27	UA26	UA25	UA24	UA23
UA34		0.903	0.5397	0.0831	0.000998	0.1958	7.13E-06	0.00124	0.000144	6.46E-08	2.21E-10	1.12E-10
UA33	2.267		1	0.9583	1.84E-01	9.69E-01	3.42E-03	7.59E-02	2.76E-02	8.26E-05	1.33E-07	2.33E-09
UA32	3.141	0.7355		0.9986	0.3862	0.9994	0.00951	0.1598	0.06833	0.000234	3.24E-07	4.84E-09
UA31	4.487	1.994	1.314		0.9067	1	0.08522	0.5112	0.3423	0.003821	6.01E-06	9.34E-08
UA30	6.453	4.013	3.464	2.253		9.92E-01	0.8772	0.9957	0.9929	0.3024	0.002213	6.5E-05
UA29	3.972	1.915	1.337	0.2601	1.616		0.3318	0.7674	0.6763	0.0494	0.000274	9.61E-06
UA28	8.215	5.966	5.535	4.473	2.359	3.59		1	1	0.9997	3.23E-01	0.0432
UA27	6.369	4.536	4.103	3.199	1.491	2.66	0.4473		1	0.9976	0.3501	0.06773
UA26	7.171	5.05	4.593	3.565	1.583	2.862	0.62	0.09998		0.9872	0.1666	0.0179
UA25	9.746	7.37	6.996	5.92	3.663	4.762	1.111	1.397	1.703		0.7694	0.2142
UA24	11.73	9.516	9.23	8.272	6.141	6.938	3.61	3.546	4.077	2.655		0.9995
UA23	13.04	10.8	10.57	9.629	7.455	8.114	4.83	4.598	5.252	3.912	1.176	

	UA34	UA33	UA32	UA31	UA30	UA29	UA28	UA27	UA26	UA25	UA24	UA23
UA34		6.05E-10	1.1E-10	1.1E-10	1.1E-10	1.1E-10	1.1E-10	1.1E-10	1.1E-10	1.1E-10	1.1E-10	1.1E-10
UA33	11.27		0.1464	7.02E-08	1.11E-10	1.10E-10	1.10E-10	1.10E-10	1.10E-10	1.10E-10	1.10E-10	1.10E-10
UA32	16.13	4.157		0.005213	1.08E-07	6.06E-10	1.1E-10	1.1E-10	1.1E-10	1.1E-10	1.1E-10	1.1E-10
UA31	22.1	9.72	5.791		0.1522	0.000675	4.72E-07	8.37E-08	1.11E-10	1.1E-10	1.1E-10	1.1E-10
UA30	25.12	13.18	9.583	4.134		6.27E-01	0.02007	0.001034	8.55E-08	1.11E-10	1.1E-10	1.1E-10
UA29	24.72	14.4	11.27	6.602	2.965		0.9755	0.3572	0.003252	8.05E-07	2.12E-10	1.1E-10
UA28	27.99	17.1	13.96	9.109	5.199	1.854		0.9589	0.1044	9.2E-05	9.70E-09	1.1E-10
UA27	25.43	16.42	13.7	9.664	6.439	3.53	1.99		0.9782	0.1458	0.000241	1.1E-10
UA26	31.41	20.95	18.08	13.51	9.657	5.986	4.358	1.824		0.8167	0.005472	1.1E-10
UA25	37.08	25.55	22.69	17.8	13.4	8.936	7.332	4.16	2.537		0.3143	2.89E-10
UA24	37.86	27.27	24.64	20.18	16.11	11.76	10.35	6.986	5.771	3.633		6.85E-05
UA23	46.18	35.42	33.1	28.76	24.42	19.19	18.06	13.64	13.21	11.58	7.436	

Length

H. carteri

Width

	UA34	UA33	UA32	UA31	UA30	UA29	UA28	UA27	UA26	UA25	UA24	UA23
UA34		0.1238	0.1362	0.001659	8.40E-11	2.20E-11	3.53E-07	3.32E-08	1.48E-06	2.67E-05	0.001254	2.35E-11
UA33	4.175		1	0.9999	0.076	0.02945	1	0.9619	0.9975	0.9999	0.9999	0.4643
UA32	4.123	0.03868		0.9999	0.07024	0.02635	0.9999	0.9553	0.9967	0.9999	0.9999	0.4418
UA31	5.941	1.051	1.001		0.000117	4.87E-09	0.6029	0.09929	0.3726	0.7217	1	0.000817
UA30	10.17	4.428	4.467	6.767		1	0.06331	0.5452	0.2768	0.1272	0.000137	0.9795
UA29	15.29	4.863	4.91	9.265	0.5602		0.004501	0.3669	0.1106	0.02873	6.68E-09	0.9857
UA28	8.291	0.9063	0.9537	3.009	4.517	5.595		0.9955	1	1	0.6381	0.4779
UA27	8.84	1.993	2.038	4.293	3.12	3.477	1.527		1	0.9991	0.1113	0.9942
UA26	7.941	1.428	1.472	3.465	3.685	4.236	0.7688	0.6924		1	0.4011	0.9086
UA25	7.185	0.9524	0.997	2.77	4.161	4.873	0.133	1.274	0.5819		0.7494	0.6842
UA24	6.034	1.005	0.9547	0.07944	6.721	9.196	2.944	4.233	3.405	2.709		0.000984
UA23	10.88	3.277	3.322	6.173	1.835	1.754	3.251	1.573	2.266	2.848	6.113	

	UA34	UA33	UA32	UA31	UA30	UA29	UA28	UA27	UA26	UA25	UA24	UA23
UA34		0.000887	0.01402	2.35E-07	6.31E-11	4.33E-11	4.36E-11	7.88E-10	5.45E-08	0.02886	5.21E-02	5.61E-01
UA33	6.146		1	0.9871	1.00E+00	8.84E-05	1.00E+00	1.00E+00	0.9727	9.28E-01	0.316	1
UA32	5.168	0.7224		1	0.9996	3.36E-06	0.9998	0.99	0.7852	0.9985	0.772	0.9888
UA31	8.385	1.732	0.7993		0.5709	4.34E-11	5.23E-01	3.59E-01	0.1202	1	0.4936	0.3395
UA30	10.39	0.299	1.184	3.071		4.94E-09	1	1	0.9559	0.4488	0.00211	1
UA29	22	6.846	7.731	13.42	9.26		1.49E-10	8.14E-06	0.0637	4.35E-11	4.33E-11	8.32E-06
UA28	11.38	0.2006	1.114	3.163	0.1583	10.06		1	0.9224	0.4291	7.53E-04	0.9999
UA27	9.658	0.8448	1.678	3.494	0.7549	7.502	0.9346		0.9985	0.2703	0.001767	1
UA26	8.725	1.905	2.627	4.191	2.034	4.513	2.209	3.351		0.08305	0.00119	0.9987
UA25	4.871	2.184	1.35	0.9294	3.308	11.59	3.348	3.702	4.384		0.996	0.2566
UA24	4.609	3.591	2.658	3.22	5.859	16.21	6.198	5.919	6.05	1.505		0.00151
UA23	9.733	0.8675	1.702	3.537	0.7857	7.496	0.9677	0.02595	1.332	3.737	5.971	

Length

S. abies

Base

	UA34	UA33	UA32	UA31	UA30	UA29	UA28	UA27	UA26	UA25	UA24	UA23
UA34		0.01348	7.32E-08	0.8643	0.00E+00	0.00E+00	0.00E+00	3.86E-11	0.00E+00	0.00E+00	0.00E+00	3.97E-06
UA33	5.189		0.1224	0.9192	3.27E-07	0.00E+00	7.37E-06	0.004598	0.01855	0.00029	0.00313	0.4376
UA32	8.685	4.184		0.001432	0.316	3.23E-08	0.9639	0.9994	1	0.9997	1	1
UA31	2.417	2.222	5.998		8.39E-11	0.00E+00	5.29E-10	1.24E-05	1.97E-05	6.19E-08	1.52E-06	0.01503
UA30	13.44	8.332	3.592	10.15		0.01064	0.9309	0.8789	0.1189	0.6075	0.2907	0.09273
UA29	20.43	14.43	8.874	16.24	5.282		4.24E-07	4.93E-06	3.92E-11	1.24E-08	5.76E-10	1.11E-09
UA28	14.6	7.547	1.978	9.769	2.17	8.269		1	0.8404	0.9999	0.9811	0.6926
UA27	10.3	5.594	1.222	7.409	2.371	7.652	0.5673		0.9969	1	1	0.9662
UA26	11.5	5.061	0.05198	7.283	4.2	10.3	2.486	1.462		0.997	1	1
UA25	13.28	6.507	1.141	8.724	3	9.088	1.02	0.2672	1.46		1	0.9619
UA24	12.34	5.731	0.4955	7.953	3.652	9.751	1.815	0.9149	0.6706	0.7907		0.9985
UA23	7.708	3.331	0.7384	5.146	4.331	9.612	2.83	1.96	0.8007	1.992	1.348	

	UA34	UA33	UA32	UA31	UA30	UA29	UA28	UA27	UA26	UA25	UA24	UA23
UA34		0.4674	0.000857	0.1269	4.14E-11	0	0	0	0	0	1.20E-07	2.18E-06
UA33	3.272		0.4833	1	9.59E-05	4.92E-14	6.53E-14	2.73E-07	0.000126	8.75E-05	0.109	0.04112
UA32	6.167	3.241		0.7726	0.5482	4.28E-05	0.001224	0.07358	0.9057	0.878	1	0.9991
UA31	4.164	0.7151	2.657		0.000655	2.59E-12	5.93E-12	2.88E-06	0.001258	0.000902	0.3427	0.1335
UA30	10.29	6.837	3.115	6.253		0.1833	0.8516	0.9987	0.9988	0.9994	0.4186	0.9796
UA29	15.52	11.4	7.067	10.82	3.953		0.9428	0.7879	0.002008	0.002774	1.64E-06	0.002676
UA28	17.47	11.38	6.05	10.66	2.454	2.11		1	0.05091	0.06775	3.39E-05	0.05687
UA27	12.05	8.375	4.447	7.791	1.332	2.62	0.9158		0.6788	0.7296	0.02675	0.5219
UA26	11.7	6.756	2.276	6.041	1.32	5.884	4.623	2.859		1	0.8315	1
UA25	11.81	6.863	2.374	6.15	1.217	5.773	4.487	2.753	1.239		0.7849	1
UA24	8.57	4.246	0.2266	3.531	3.37	7.934	7.133	4.908	2.51	2.628		0.9992
UA23	7.862	4.72	1.281	4.136	1.833	5.786	4.571	3.165	0.7965	0.8964	1.253	

Diameter

U. rotula

Central area

	UA34	UA33	UA32	UA31	UA30	UA29</
--	------	------	------	------	------	--------

Fig.S2: Tukey HSD (Honestly Significant Difference) results in the Perales section; the q (studentised range distribution) and the *p* values are below and above the diagonal, respectively. Significant differences among the samples are recorded by *p* value < 0.05 (marked in pink), higher differences are recorded by *p* < 0.001 (marked in orange).

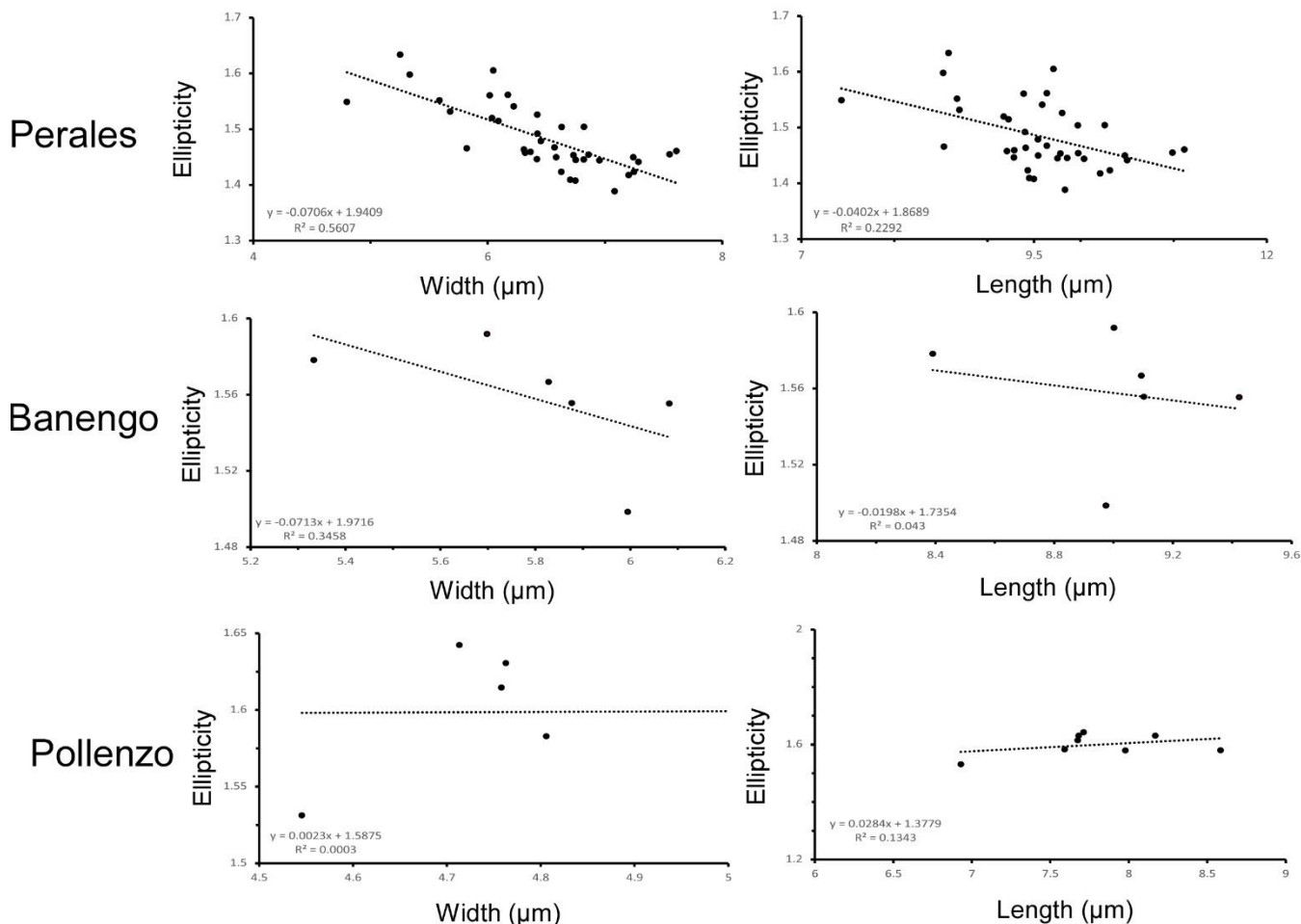
		<i>H. carteri</i>										
		Length					Width					
		Bm5	Bm4	Bm3	Bm2	Bm1		Bm5	Bm4	Bm3	Bm2	Bm1
Banengo	Bm5		0.2437	0.9947	0.9982	0.003586			0.015	0.001276	0.943	0.3715
	Bm4	2.903		0.213	0.5514	1.688E-05		4.466		0.9729	0.2311	0.7685
	Bm3	0.5637	3.002		0.9743	0.04798		5.467	0.8671		0.05721	0.3853
	Bm2	0.4238	2.147	0.8553		0.007679		1.068	2.943	3.81		0.8926
	Bm1	5.071	6.906	3.903	4.759			2.555	1.655	2.522	1.288	
Pollenzo	Pm7											
	Pm6	2.379		0.8682	0.6459	1.51E-07	0.03632	0.00164				
	Pm5	0.513	1.787		0.9999	0.001314	0.703	0.2257				
	Pm4	0.03239	2.342	0.4806		0.004794	0.883	0.4135				
	Pm3	5.181	8.362	5.694	5.213		0.1776	0.6284				
	Pm2	1.704	4.347	2.217	1.737	3.477		0.9871				
	Pm1	2.802	5.615	3.315	2.835	2.379	1.098					
	Pm1	2.643	4.608	2.208	2.692	4.196	0.393					
		<i>S. abies</i>										
		Base					Length					
		Bm5	Bm4	Bm3	Bm2	Bm1		Bm5	Bm4	Bm3	Bm2	Bm1
Banengo	Bm5		7.27E-07	0.000397	2.05E-06	2.58E-12			0.7009	0.1085	4.69E-08	8.13E-11
	Bm4	7.811		0.7635	0.9998	0.3293		1.817		0.8562	0.000478	7.42E-06
	Bm3	5.886	1.667		0.8542	0.02023		3.446	1.411		0.01698	0.000602
	Bm2	7.523	0.2496	1.418		0.2411		8.538	5.821	4.41		0.8808
	Bm1	10.88	2.662	4.329	2.911			10.07	7.151	5.74	1.33	
Pollenzo	Pm7											
	Pm6	3.261		7.903E-06	0.7518	5.64E-01	0.0000691	0.0000691				
	Pm5	9.138	7.291		9.876E-09	8.386E-08	0	0				
	Pm4	1.542	2.105	9.01		0.9978	0.0095	0.0095				
	Pm3	0.647	2.514	8.491	0.7953		0.1491	0.1491				
	Pm2	2.939	6.655	12.08	4.936	3.586		1				
	Pm1	2.939	6.655	12.08	4.936	3.586	0					
	Pm1	3.943	2.149	2.373	2.791	0.3326	0.7111					

Fig.S3: Tukey HSD (Honestly Significant Difference) results in the Piedmont Basin; the q (studentised range distribution) and the *p* values are below and above the diagonal, respectively. Significant differences among the samples are recorded by *p* value < 0.05 (marked in pink), higher differences are recorded by *p* < 0.001 (marked in orange).

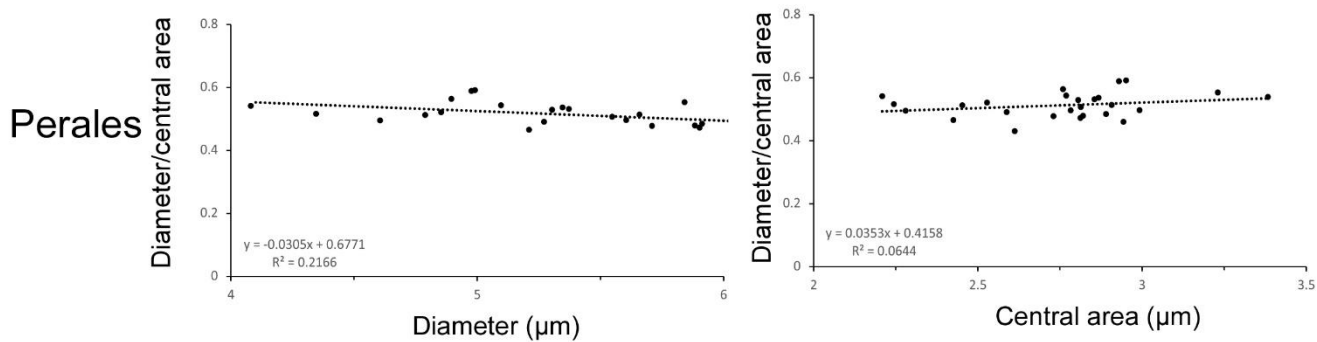
2.2 Correlation coefficient

In the following part the obtained correlation coefficient R^2 between some measured biometric parameter analysed in our study are listed.

H. carteri



U. rotula



R. minuta

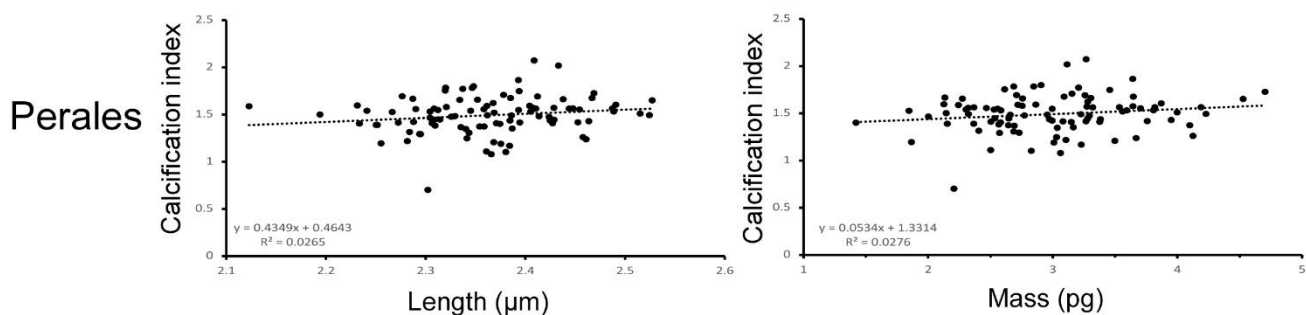
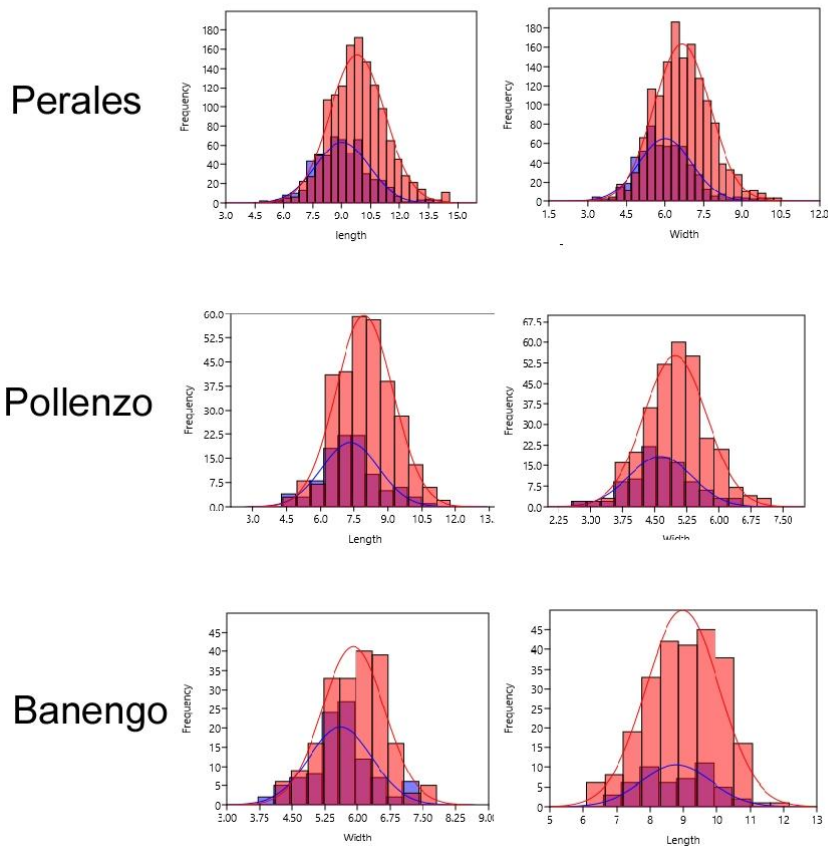


Fig.S4: Correlation coefficient R^2 between some measured biometric parameters analysed in our study.

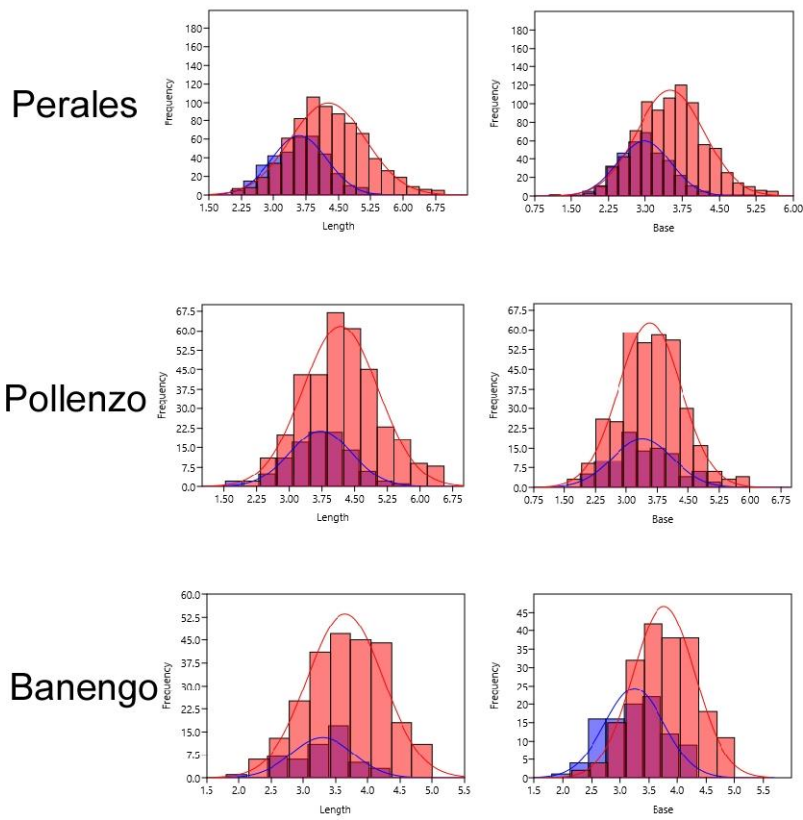
2.3 Frequency histogram

In the following part we illustrate with histograms how frequent are some size ranges during the MSC onset bioevent (blue column) and in the remaining part of the section (red column).

H. carteri



S. abies



U. rotula

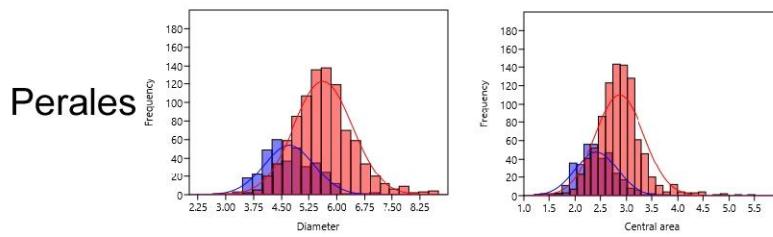


Fig.S5: Frequency histogram showing different size range of the measured biometric parameters. Blue (violet when superimposed) column refers to results obtained in the cycle hosting the MSC onset bioevent, the red column refers to the remaining part of the dataset.

CHAPTER 3- Taphonomic bias and paleoenvironmental conditions across the first phase of the Messinian Salinity Crisis in the Sorbas Basin (SE Spain)*

During the Messinian Salinity Crisis (MSC, 5.97-5.33 Ma) the combination of tectonic and climatic processes resulted in the deposition of evaporite across the Mediterranean Basin. The calcareous nannofossil (CN) and foraminifer disappearance approximately at the onset of the MSC was interpreted as caused by hypersaline conditions in the water column, that were lethal for most marine eukaryotes. Here we focus on potential taphonomic bias affecting the preservation of calcareous fossils deposited across the first phase of the MSC in the Sorbas Basin, with the aim to test if their disappearance was related to adverse environmental conditions or to the preferential dissolution of biogenic calcite. Samples were collected in the Sorbas Basin (S-E Spain), spanning the pre MSC and its first phase, characterised by the presence of gypsum/marl couplets.

Micropaleontological analysis and petrographic observation suggest that the dissolution of biogenic calcite approximately at the MSC onset was the result of a taphonomic bias related to the oxidation of both pyrite and organic matter at the sea floor. A generally poorly preserved micropaleontological assemblage was recorded during the first phase of the MSC together with aragonitic laminated sediment, which deposited possibly as a result of intense bloom of non-calcifying autotrophs. This suggests either that calcite suffered chemical instability and/or the biocalcifier organisms were suppressed by ecological competition. The fossil association recorded during this interval indicated a lagoonal-like environment punctuated by more open marine episodes and a shallowing of the basin upward in the section. We concluded that the disappearance of calcitic fossil approximately at the MSC onset was related to the ongoing basin restriction that increased the

sensitivity of the basin to the fresh-water input and temperature changes; this in turn enhanced the alternance between stratified and mixed water column condition and promoted a seasonal fluctuation of the chemocline.

* This chapter is based on Mancini, A. M., Gennari, R., Natalicchio, M., Dela Pierre, F., Lozar, F., (in prep.). Taphonomic bias and paleoenvironmental conditions across the first phase of the Messinian Salinity Crisis in the Sorbas Basin (SE Spain)

1.1 Calcareous nannofossils analysis

A total of 97 samples were processed with the standard smear slides technique (Bown and Young, 1998) for the calcareous nannofossils (CN) relative abundance study. Particular attention was paid in the smear slide preparation procedure in order to avoid contamination between samples, since the presence/absence of CN is an important parameter in this study. In each slide, at least 400 CN specimens were identified and counted at 1250× by polarized light microscopy; the reworked species from older stratigraphic interval were counted separately. The taxa *Sphenolithus abies* and *Sphenolithus moriformis* were grouped together in the informal group *Sphenolithus* gr. Since the marine fossil record in PLG deposits was often considered as the result of reworking from older sediments (Trenkwalder et al., 2008; Karakitsios et al., 2016), our analysis aimed at assessing the potential reworked nature of the CN and, in general, of the micropaleontological assemblage. Accordingly, we assume that the presence of intact coccosphere and/or the preservation of dissolution prone species (*i.e.* *Syracosphaera pulchra*, *Pontosphaera* sp., according to Roth et al., 1975; Roth and Coulbourn, 1982; Roth, 1994; Gibbs et al., 2004) are likely indicative of in-situ assemblages, suggesting moderate or no reworking processes

1.2 Microfossil analysis

A total of 57 samples from the Los Molinos and Perales sections were prepared for the benthic and planktic foraminiferal investigation. About 100 g of oven-dried sediment were soaked in

diluted H₂O₂ for 1 day, and dry-sieved to obtain 3 different size fractions: > 500 µm, 500 - 125 µm and 125 - 63 µm. The analysis was performed on both the > 125 µm and < 125 µm residues as the largest size fraction only yield non-disaggregated sediment fragments. Since foraminifer abundance and preservation were often scarce, we chose to describe samples by means of qualitative observations separately on the > 125 µm and < 125 µm residues.

1.3 Petrographic and mineralogical analyses

A total of 11 thin sections were obtained from epoxy impregnated samples cut parallel and perpendicular to the bedding. Optical microscope observations of the thin sections were performed using an Olympus BX51 (Department of Earth Science, University of Turin) Two representative thin section of laminated samples were observed using a Nikon microscope equipped with a B-2a filter block (illumination source with an excitation wave length of 450–490 nm) (Department of Plant Biology, University of Turin). Selected sites were carbon coated and analyzed at the Scanning Electron Microscope (SEM) using a JMS-IT300LV instrument (Department of Earth Sciences, University of Turin). Semi-quantitative characterization of the main elements was performed during SEM investigation using an energy-dispersive EDS Oxford Instrument Link System microprobe. Elemental compositional maps were performed on selected area using the software Inca (acquisition time 1 hour, Cts > 130000). Additional 1- 2 representative stubs from freshly broken sediment chips for each precessional cycle were prepared for morphological investigation. Morphological investigation was also performed on previously picked microfossils (benthic and planktic foraminifers and ostracods).

The laminated sediments from cycles PLG4 and PLG7 show alternance of white and brown laminae (Fig.4); the white laminae from 11 samples were scraped using a tiny needle and then powdered using an agate mortar. Powder of limestone layer belonging to the PLG6, PLG7, PLG9 and PLG11 was obtained as well using the same procedure. The powders were successively analyzed with X-Ray Powder Diffraction (XRPD). Measurements for the raw identification of the crystalline

phases were carried out using a Rigaku MiniFlex 600 benchtop X-ray diffractometer (Bragg-Brentano geometry, CuK α radiation, X-ray source operating at 600W (40 kV, 15 mA); D/teX Ultra2 silicon strip detector; $2^\circ < 2\theta < 50^\circ$, step width 0.01° , scan speed $5^\circ/\text{min}$).

1.4 Carbon and oxygen stable isotope analyses

An aliquot of the same powder samples prepared for XRD analyses was used for stable oxygen and carbon isotope analyses using an automated carbonate preparation device (Gasbench II) and a Thermo Fisher Scientific Delta V Advantage continuous flow mass spectrometer at the Department of Earth Sciences, University of Milan. Carbonate powder samples were reacted with > 99% orthophosphoric acid at 70°C . The carbon and oxygen isotope compositions are expressed in the conventional delta notation calibrated to the Vienna Pee-Dee Belemnite (V-PDB) scale by the international standards IAEA 603 and NBS-18. Analytical reproducibility for these analyses was better than $\pm 0.1\text{‰}$ for both $\delta^{18}\text{O}$ and $\delta^{13}\text{C}$ values.

2- Results

2.1 Calcareous nannofossils

Calcareous nannofossil content of the pre-MSC in the Perales section was described in detail in Mancini et al. (2020). Cycle UA34 records the so called MSC onset bioevent (Lozar and Negri, 2019; Mancini et al., 2020) that coincides with a relevant increase in the CN absolute abundance (Mancini et al., submitted). Above this event, the CN absolute abundance significantly decreases and the assemblage is dominated by *Coccolithus pelagicus* and *Reticulofenestra pseudounbilicus*. The preservation of CN from the MSC onset bioevent toward the MSC onset (base of cycle PLG1) progressively decreases, as also suggested by dissolution feature (e.g. etching) affecting coccoliths (mostly *Helicosphaera carteri* and *C. pelagicus*). From the second limestone bed of cycle UA34 (Fig.2), the observation of smear slides indicates the sharp disappearance of CN; above this level and up to cycle PLG2, CN are absent. Interestingly, reworked specimens of older

stratigraphic intervals, usually present in the UA cycles with variable percentages (0.4 -23.6 %), were not observed in this interval.

Los Molinos section

In the Los Molinos section, CN are present in 36 samples out of 61. The CN preservation is generally scarce, as revealed by dissolution features affecting coccoliths (e.g. etching; Fig.2c, supplementary material Fig.7c). The abundance and diversification of the CN are generally low, except for few samples with higher concentration and more diversified assemblage in cycles PLG4, PLG6, PLG7, PLG9 (Fig.1). Overall, the CN assemblage is dominated by *R. minuta*, followed by other reticulofenestrids, *Helicosphaera carteri*, *Sphenolithus* gr.; *Coccolithus pelagicus*. *Umbilicosphaera rotula* and *Umbilicosphaera jafari* are present in moderate to low abundance. The content of reworked specimens of older stratigraphic intervals is generally low (~ 2% on average) and rarely exceed 5%. In one sample both dissolution prone CN and intact coccospheres (*R. minuta*, *R. haqii*, *U. jafari*, *H. carteri*, *C. pelagicus*) are present (PLG4, Fig.1).

It is worth noting that all the samples devoid of possible in situ assemblages are also characterized by the absence of clearly reworked specimens. In particular cycles PLG1, PLG2, PLG5 and PLG8 are completely barren of both autochthonous and reworked CN.

Rio Aguas section

In the Rio Aguas section, all samples are barren of CN except in two cases (lowermost sample of PLG8) in which Paleogene and Cretaceous nannofossils were encountered in extremely low abundance.

2.2 Foraminifera

Perales section

Planktic foraminifers (PF) disappearance at the top of cycle UA33 predates the BF disappearance (Manzi et al., 2013; this study). BF are present up to the second limestone layer of cycle UA34; within this cycle, they are exclusively represented by the stress tolerant Bolivinids and

Buliminids, whose shell is characterized by a progressive increase in dissolution and encrustation features (Fig.2a; supplementary material Fig.2); this trend coincides with abundant pyrite or oxidised pyrite observed inside the foraminifer shell (Fig.2a; supplementary material Fig.2). Above the second limestone, foraminifers are absent at the optical microscope observation of the blue clay and the marls of cycles PLG1 and PLG2.

Los Molinos

In the Los Molinos section foraminifers are generally scarce or absent except in cycle PLG6 and 9 where some layers yield more frequent BF. Preservation is generally scarce, with specimens showing partial dissolution of the external side of the wall, fragmentation and external encrustation; pyrite or oxidised pyrite infills were also observed (Fig.2; Fig 3; supplementary material Fig.7). In some case, the external encrustation of the shells hampered the identification at the species or even at genus level.

In cycle PLG4 the >125 µm fraction is always barren, except in one sample where they are more frequent, while rare bolivinids and *Turborotalita quinqueloba* are present in the smaller fraction of samples collected in the lower half of the hemicycle (Fig.1). All the samples of cycle PLG5 were barren of foraminifera in both the size fractions. The basal sample of cycle PLG6 yield very rare and badly preserved BF in the small-size fraction. Rare to common *Fursenkoina fusiformis* is observed in the middle of the marly interval of PLG6; the assemblage is nearly monospecific, although some *Bulimina aculeata* is also present in the <125 µm size fraction. Just above, only few *Criboelphidium specimens* and small bolivinids were observed. In cycle PLG7 barren samples alternates with samples yielding rare BF that are variably represented by *Ammonia*, *Criboelphidium*, *Bulimina* and *Bolivina* in both size fractions. Usually the assemblages are oligospecific, except in PLG7 at 90 cm, where these genera are present together. Cycles PLG11 and 12 are prevalently barren: on 16 collected samples, only 7 contain calcareous fossils. Instead, in the entire marly interval of cycle PLG9, samples yield rare to common miliolids, sometimes associate with

disarticulated valves of the *Cyprideis* ostracod genus. As for PLG6 the assemblage is nearly monospecific.

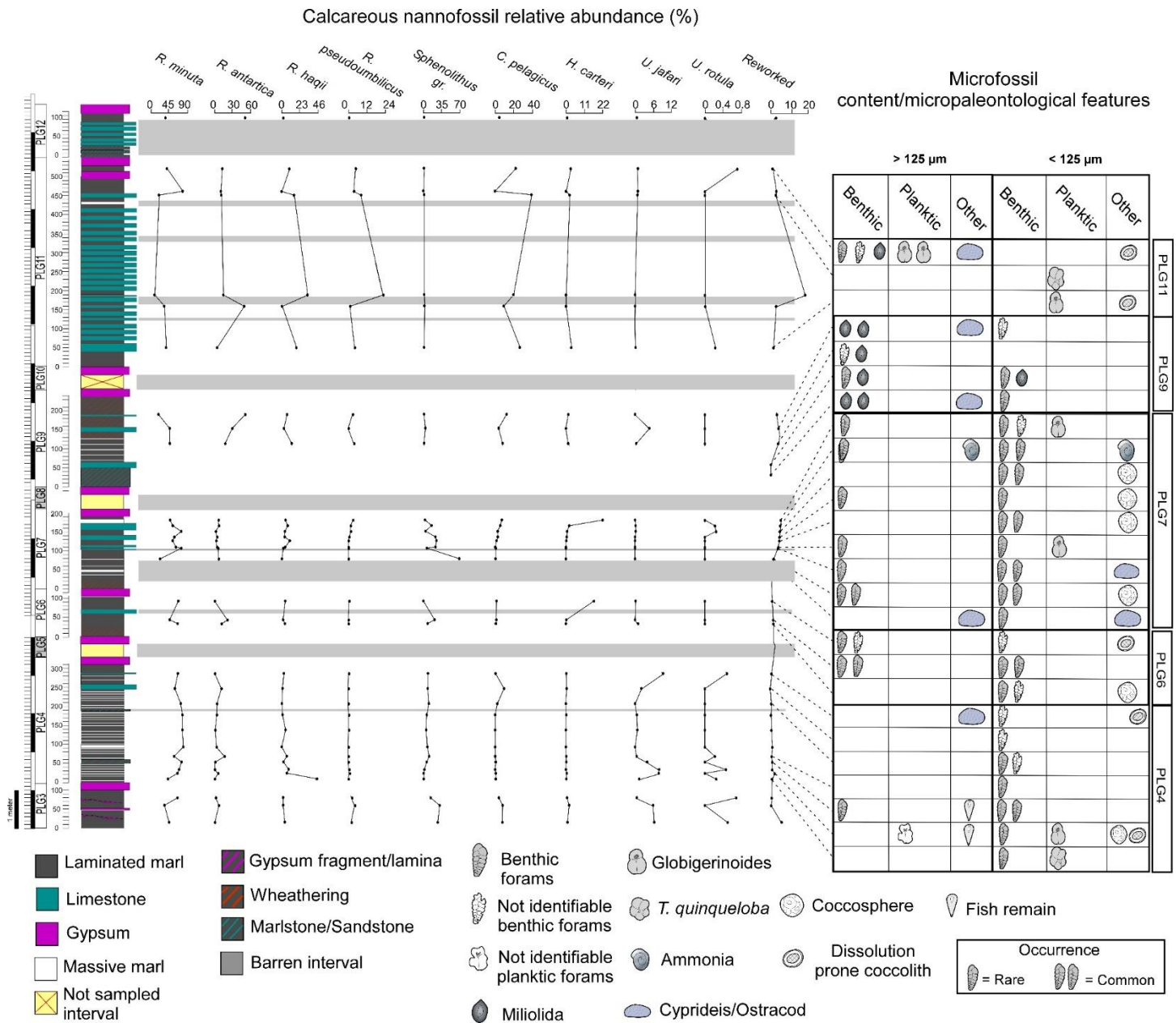


Fig. 1: Micro and nanno paleontological content of the composite section (Perales and Los Molinos). Bolivinids, Buliminids, Uvigerinids, Elphidium, Cibroelphidium and Fursenkoina are grouped together and plotted as Benthic foraminifers. PLG5 and PLG8 were barren of fossils; PLG10 was sampled and measured. Gypsum layers are not to scale.

2.3 Petrographic and taphonomic observation

The petrographic and micropaleontological analyses allowed to recognize 3 distinct intervals with different distribution, abundance and preservation of the calcareous fossils in the transition between the pre-evaporitic and in the MSC deposits (i.e. from cycles UA34 to PLG12). From the bottom to the top of the composite section, these intervals are:

Interval A

This interval spans from the base of UA34 up to the second limestone layer of the cycle UA34 (Fig. 2). Planktic foraminifers disappear at the optical microscope investigation at the base of the taphonomic interval A (top of UA33), although few specimens of *Orbulina universa* were sporadically encountered up to the first limestone layer. The taphonomic interval A is characterized by the presence of the MSC onset bioevent, in which CN absolute abundance is higher in our stratigraphic record (Mancini et al., submitted). During the MSC onset bioevent, CN dominate the fossils assemblage and they do not show any major indication of dissolution. Above the MSC onset bioevent, a decrease in the preservation state of BF was recorded; they frequently show encrustation and/or dissolution of the calcitic wall as well as an increase in pyrite and/or oxidised pyrite infill (Fig.2 A4, A4₂; supplementary material Fig 2 A, B, C, D, E and F). Pyrite and oxidised pyrite moulds most likely after PF and BF were observed in this interval (Fig.2 A3 and A3₂); these features increase upward in the section, becoming very common in the second limestone layer of the UA34. This level marks the CN and BF disappearance at the optical microscope investigation, and it represents the inception of the taphonomic interval B, which continues up to the PLG3.

Interval B

The second limestone layer at the top of cycle UA34 hosts a wide variety of framboid pyrite moulds after PB and BF (Fig. 2, B1, B1₂, B1₃, supplementary material Fig.4). In some case, the calcitic shell of foraminifera is either completely dissolved or replaced by fine-grained calcitic mineral (Fig.2 B1₂). Foraminifers with secondary calcite infill with dissolved/altered shell were present (Fig.2 B1₃). This layers is overlain by a blue/grey clay bed characterised by the very low abundance of Ca²⁺ (supplementary material, Fig.5) as revealed by the elemental compositional analysis (EDS).

Subspherical Si-rich grains with a circular cross section (300 to 800 μm in diameter) surrounded by a siliciclastic matrix were commonly observed in this level. Rounded cavities with oxidised pyrite infill with honeycomb shape were also observed (Fig.2 B2₂). Laminated marls belonging to the PLG unit overlays the clay level and record the presence of pyrite and oxidised pyrite as aggregates resembling foraminifer shape. Elongated aggregate of pyrite and oxidised pyrite frequently resemble normal size and dwarfed BF (Fig.2 B3).

Interval C

This interval is marked by the reappearance of poorly preserved calcitic fossils (CN and foraminifer assemblages) (Figs. 1 and 3 B, C, D, E and F; supplementary material Fig. 7 A, B, C, D, E and F) from cycle PLG3 upward, although some cycles (i.e. PLG5 and PLG8) were completely barren.

2.3.1 The laminated marls of the PLG4 and PLG7

The marly hemicycles of cycles PLG4 and PLG7 hosts laminated silty marls typified by the alternation of sub-mm brown and white laminae. The brown laminae are characterised by the presence of terrigenous material (Fig. 5); elemental compositional maps revealed an enhanced presence of elements usually related to terrigenous input of clay and detrital minerals (Mg, Si, Al and K; Fig.5; Bulian et al., 2021). Calcareous nannofossils, aragonite (as revealed by the XRD analysis), calcite and small size pyrite grains are also present in these laminae as a minor component. Based on the XRD results, the white laminae are almost exclusively composed of aragonite (supplementary material, Fig.6) (about 70% – 90% based on SEM inspection), with CN and pyrite as minor components; celestite and barite were sporadically observed. Two common aragonite morphologies were detected: aragonite with bladed crystals, about 10 μm long and acicular needles usually < 6 μm . Bladed crystals sometimes show locally radial orientation. The aragonitic laminae displays 1 – 5 μm large longitudinal cracks (Figs. 4 and 5). Aragonite aggregate (i.e. peloids) with different size and shape from the surrounding matrix were detected (supplementary material Fig. 6 C and F).

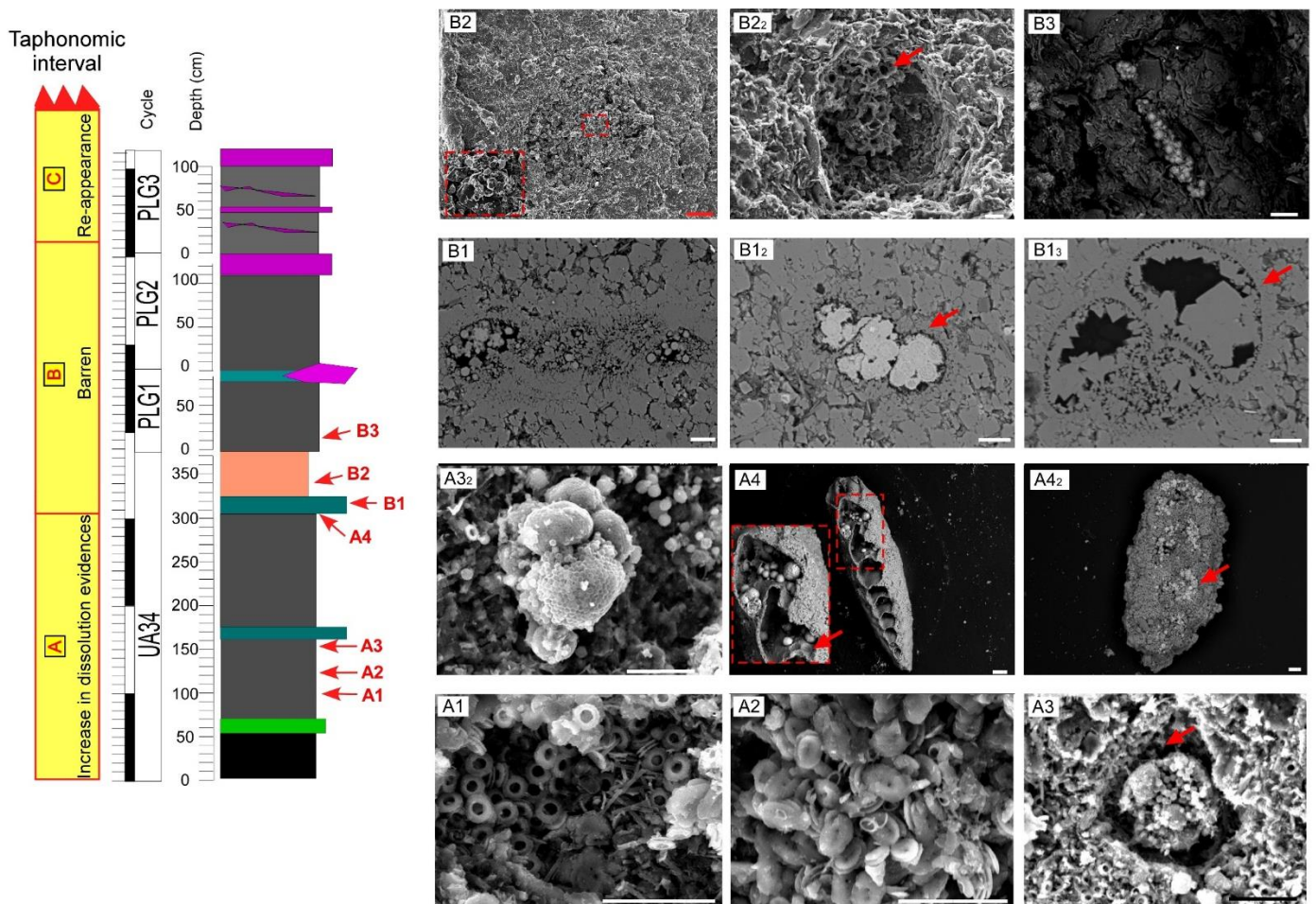


Fig. 2: Left: stratigraphic column of the interval encompassing the MSC onset in the Perales section with the main recorded taphonomic interval numbered from A to C. On the right there are SEM images performed on freshly broken surface or thin sections and on hand picked foraminifers. The red numbered letter refers to the exact location of the samples. A1: High abundance of *U. rotula* recorded during the MSC onset bioevent. A2: High abundance of *H. carteri* recorded during the MSC onset bioevent. A3: Hole with pyrite infills, putative foraminifer internal mold. The red arrow indicates the empty space between the pyrite and the surrounding sedimentary matrix, interpreted as a dwarf foraminifer internal mold. A3₂: Pyrite mold of putative dwarf foraminifer, probably a Turborotalid. A4: Hand-picked benthic foraminifers belonging to the genus *Bolivina*. The specimens show dissolution feature on the shell margin. Red arrows indicate oxidised pyrite that leave dissolution footprint on the internal calcitic wall. A4₂: Hand-picked benthic foraminifers showing large calcitic encrustation and oxidised pyrite infills. Red arrow shows the boundary between the oxidised pyrite and the calcitic wall, the latter is highly altered and/or dissolved. B1: Thin section showing dissolved and altered phosphatic fish remain with oxidised pyrite infills. B1₂: Thin section showing pyrite mold of a foraminifer. Red arrow shows the replacement of the original calcitic wall with fine grained calcite. B1₃: Thin section showing a foraminifer with large calcitic cristals growing near the wall. Red arrow indicate the highly altered foraminifer wall. B2: Freshly broken sediment surface of the blue/gray clay interval showing rounded hole with quartz cristal infill surrounded by a siliciclastic matrix. The calcium content of this layer is nearly

absent (see also supplementary material, Fig. 5). B2₂: Hole with oxidised pyrite with honeycomb structure. B3: Oxidised pyrite resembling dwarf benthic foraminifer. Scale bar is 20 µm, except in the C1 in which is 100 µm

2.4 C and O stable isotope analyses

The stable isotope results were plotted and compared with the stable isotope composition of the aragonite performed in different setting and sources (Fig.6). The aragonite laminae show positive $\delta^{13}\text{C}$ values ranging from +2.49 to +3.56 ‰ whereas the $\delta^{18}\text{O}$ values are slightly negative (from -2.28 to -0.25 ‰) (Fig.6). The $\delta^{18}\text{O}$ and $\delta^{13}\text{C}$ values of the limestone strongly fluctuating from -4.75 to -0.40 ‰ and from +0.93 to +3.63 ‰, respectively. Lower $\delta^{18}\text{O}$ were recorded in PLG9 and PLG11 (-3.73 and -4.75 ‰, respectively; Fig. 6), while PLG6 and PLG7 showed heavier values (4.73 and -0.36 ‰, respectively).

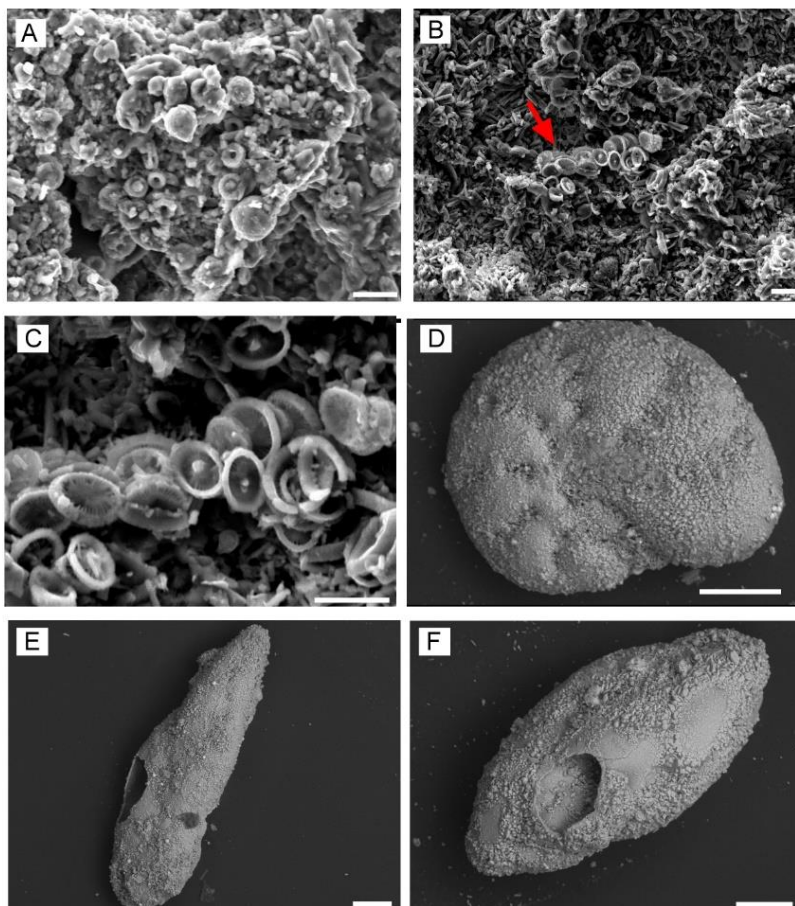


Fig.3: SEM images of freshly broken sediment surface and hand-picked foraminifers of the Los Molinos samples. A: Fecal pellet mostly composed by CN (PLG4). B: Red arrow shows a disrupted coccosphere of *Syracosphaera pulchra* surrounded by aragonitic matrix (PLG7). C: enlargement of B; cluster of *Syracosphaera pulchra* showing dissolution and fracturing

features. D: Benthic foraminifer showing calcite encrustation (PLG7). Oxidised pyrite is also present as a minor component of the encrustation E, F: Benthic foraminifers showing dissolution of the external wall and calcitic/pyritic encrustations (PLG7).

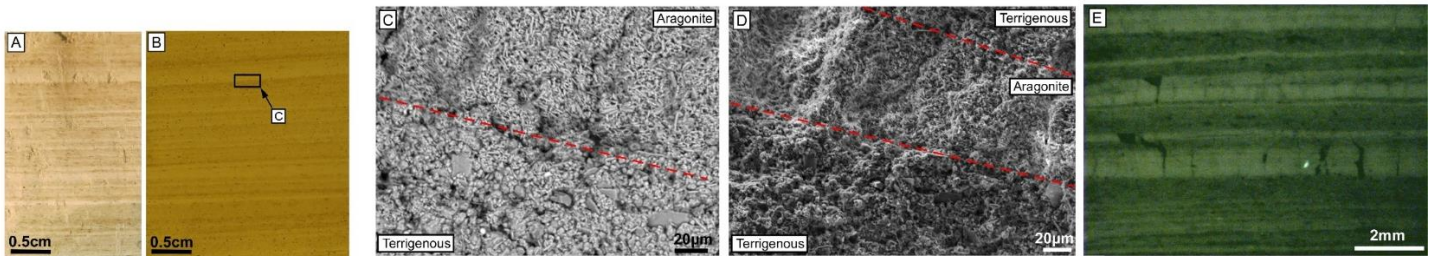


Fig.4: Photographs of the laminated marls characterizing the PLG4 and PLG7. A: Polished slab of the freshly broken sediment. B: Thin section of the same sample as in A; the dark square is enlarged in C. C: SEM photograph of the thin section showing the alternance of the brown terrigenous laminae and the white aragonitic laminae. Note that longitudinal cracks characterise the white aragonitic lamina. D: SEM photograph of freshly broken sediment showing the alternance of the brown terrigenous laminae and the white aragonitic laminae. E: Fluorescence analysis in false colour; note that the aragonitic laminae show stronger fluorescence.

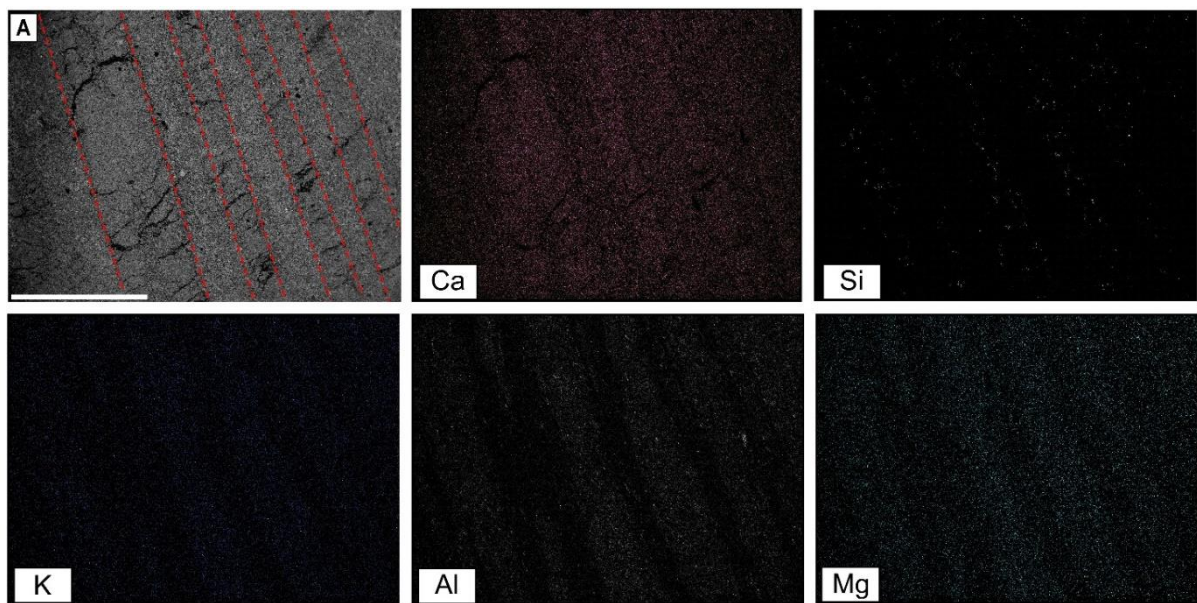


Fig.5: Representative SEM photograph and elemental map (Ca, Si, K, Al and Mg) of the laminated marls of PLG4 and PLG7. A is the reference image; the white laminae with distinct longitudinal cracks are underlined by the red dashed lines. Scale bar is 1 mm

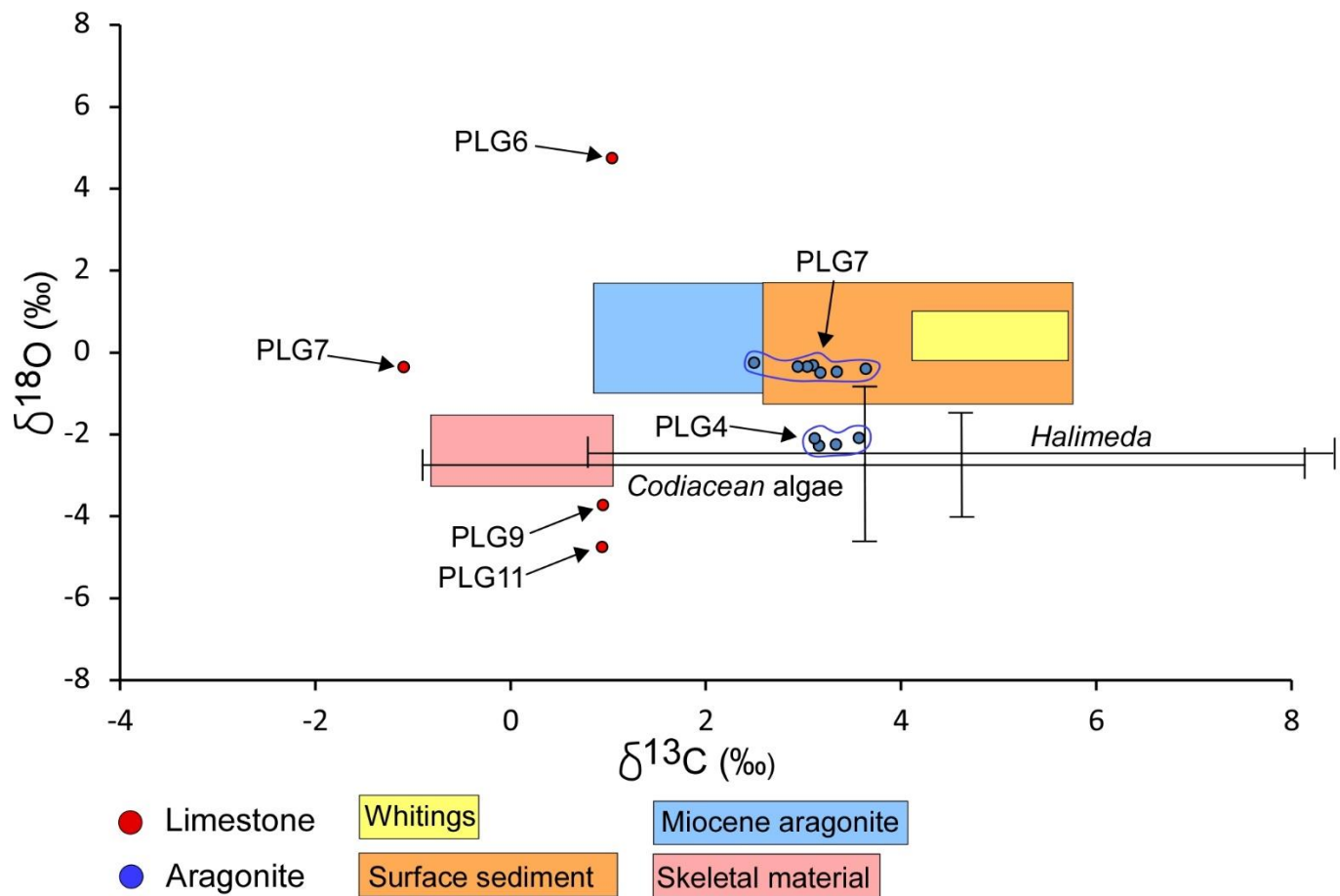


Fig.6: Oxygen and Carbon stable isotope results. The results are compared with the stable isotope composition obtained from different aragonitic materials at the Great Bahamas Bank. Data from Shinn et al., 1989 (yellow rectangle; suspended materials); Swart et al., 2009 (orange rectangle, surface sediment); Turpin et al., 2011 (light blue rectangle; Miocene); Weber, 1965; Milliman, 1974; Swart, 1983; Land, 1989 (pink rectangle; skeletal materials of scleractinian corals, echinoids); Lee and Carpenter, 2001 (*Halimeda* and *Codiacean algae*; dark lines).

3- Discussion

3.1 Paleoenvironmental changes at the MSC onset: a taphonomic perspective

The disappearance of calcareous marine microfossils has long been used as the biostratigraphic marker that best approximates the MSC onset (e.g. Sprovieri et al. 1996, Blanc-Valleron et al. 2002; Manzi et al. 2007, Gennari et al., 2013; Violanti et al., 2013; Gennari et al., 2018; Manzi et al., 2016; Manzi et al., 2018). However, the diachronous nature of the CN and foraminifers

disappearance is demonstrated in sections belonging to the Piedmont and Sicily basins (Violanti et al., 2013; Dela Pierre et al., 2014; Catalano et al., 2016; Sabino et al., 2020a; Gennari et al., 2020). Interestingly, in several sections across the Mediterranean the CN disappearance approximating the MSC onset also involves reworked specimens (i.e. of older stratigraphic intervals), although the terrigenous inputs of older sediments were still abundant above the onset of the MSC (e.g. Natalicchio et al., 2019; Sabino et al., 2020). The disappearance of marine calcareous fossils was previously interpreted as the result of increasing salinity in the water column (Blanc-Valleron et al., 2001). However, we suggest that the disappearance of calcitic fossils could reflect a severe taphonomic bias that is unrelated to changing salinity conditions. The influence of taphonomic processes will be discussed below according to the three intervals (A, B, C) described in paragraph 3.3).

3.1.1 Taphonomic interval A

Approximately from the cycle UA27 upward, the PF showed a substantial deterioration in the preservation state, with an increase in abundance of the specimens affected by encrustation of external wall, sediment/mineral infills and the break-up of the calcitic wall (Fig.2; Reghizzi et al., 2017; Mancini et al., 2020). Similar features, including dissolution of biogenic calcite, were also observed and accurately detailed in the East Mediterranean from the Tortonian/Messinian boundary where they increase toward the MSC onset (Antonarakou et al., 2018).

In the uppermost pre-evaporitic cycles of the Perales section peculiar taphonomic events can be recognised in succession from the bottom to the top of the interval (Fig.2). These events are:

1-Planktic foraminifers disappearance was accompanied by the presence of foraminifer internal moulds made up of pyrite or oxidised pyrite (Fig.2, A3, A3₂); the calcitic wall of foraminifers was partially or, in some cases, completely dissolved, leaving an empty cavity between the pyrite infill (moulds) and the surrounding sedimentary matrix (Fig.2, A3). These features suggest that the PF disappearance was related to dissolution process which occurred during diagenesis. The pyrite

foraminifer moulds progressively increase their abundance upward, becoming widely diffuse in the second limestone layer of UA34, which marks the CN and foraminifer disappearance (base of the taphonomic interval B, Fig.2; supplementary material Fig.4).

2- Benthic foraminifers were generally well preserved up to the cycle UA34 (supplementary material Fig.1); from this cycle upward, they showed a marked decrease in the preservation state (increasing dissolution features) up to their disappearance in the second limestone layer of UA34 (Fig.2 A, A₄ supplementary material Fig.2).

3-Increase in relative abundance of dissolution-resistant CN taxa (i.e. *C. pelagicus* and *R. pseudoumbilicus*; supplementary material Fig.3) toward the MSC onset and CN disappearance at the second limestone layer of UA34. These two taxa were reported to be among the most dissolution-resistant taxa (Roth et al., 1975; Roth and Coulbourn, 1982; Roth, 1994; Gibbs et al., 2004), thus their predominant presence concomitant with the absence of dissolution prone specimens could suggest that dissolution, other than paleoecological preferences, resulted in the observed micropaleontological assemblage.

Such succession of events agrees with the fact that, among the investigated calcifying microfossils, PF are the most susceptible to dissolution, followed by CN and BF (Steinsund and Hald, 1994; Peterson and Prell, 1985; Chiu and Broecker, 2008; Subhas et al., 2018). In the taphonomic interval A we did not record any evidence of an increase in salinity, either gradual or sharp; rather the *S. abies* and *H. carteri* peaks during the MSC onset bioevent suggest a decrease in salinity, since these taxa were reported to tolerate environment characterized by freshwater influence (Mancini et al., 2020). Such observation agrees with other independent geochemical data (C, O, Sr isotopes and gypsum fluid inclusion) suggesting that the paleoenvironmental changes at the pre-evaporitic/evaporitic transition were mostly related to increasing runoff influence (Natalicchio et al., 2014; Reghizzi et al., 2017; Gennari et al., 2018). Summarizing, we suggest that the calcitic fossil disappearance characterising the interval B was related to a taphonomic bias rather than the instauration of a hostile environment for the proliferation of CN, PF and BF.

3.1.2 Taphonomic interval B

The taphonomic interval B starts from the second limestone layer of UA34 and it is characterized by abundant pyritized internal moulds of foraminifers, showing different shapes (Fig.2 B1, B1₂, B1₃, supplementary material Fig.4 a, b, c, d, e, f and h). In some cases, the pyrite moulds are surrounded by a rim of calcite microspar (Fig.2 B1₂), interpreted as the replacement of the foraminifer calcitic wall during diagenesis. Highly dissolved phosphatic fish remain filled with pyrite framboids were also documented in this layer (Fig.2 B1), further suggesting that the original paleontological signal suffered obliteration by biostratinomic and/or taphonomic processes.

Different sized holes (100 - 1500 μm), partially filled with oxidised pyrite forming a honeycomb shape, were observed (Fig.2 B2 and B2₂). Another peculiar feature of the taphonomic interval B is the presence of Si-rich subspherical grains (300 to 800 μm in diameter) (Fig. 2 C; supplementary material Fig.5) within the grey/blue clay interval overlaying the second limestone layer of UA34. These grains could represent former frustules of centric diatoms which suffered dissolution and re-precipitation of quartz crystals. Moreover, the nearly absence of calcium in the grey/blue clay level (supplementary material, Fig.5) suggests that the absence of calcitic fossil could be related to a taphonomic bias.

The marly hemicycles of PLG1 and PLG2 are barren of micropaleontological content at the optical microscope investigation. However, the SEM analyses revealed taphonomic features similar to interval A, such as aggregates of pyrite crystals that mimic microfossil morphologies. Most of them resemble pyrite mould of dwarfed benthic foraminifers (Fig.2 B3), which are very common in some levels of the PLG1 and PLG2 marls. Although not straightforwardly reconciled to any microfossil groups, these features could represent foraminifer moulds and in conclusion, we suggest that the absence of calcareous and siliceous fossils in the taphonomic interval B could be related to a taphonomic bias.

3.1.3 Taphonomic interval C

As introduced in the previous paragraph, calcareous microfossils are scarce and discontinuously present (and/or preserved) throughout this interval, showing variable preservation. Generally, the assemblage is dominated by dissolution resistant taxa, such as reticulofenestrid, the *Sphenolithus* gr. and *C. pelagicus* (Gibbs et al., 2004). However, dissolution-prone taxa are also present (e.g.: *S. pulchra* and *Pontosphaera multipora*) although showing high etching degree indicating dissolution in some samples.

Where present, BF often show fracturing, etching or loss of the chamber walls (Fig.3 E and F), while PF are only present in few layers (Fig.1).

Our results show a substantial difference between the fossil assemblage recorded in the Los Molinos and the coeval PLG7 cycle of the Rio de Aguas sections. The PLG7 cycle of the Los Molinos section host common CN, rare BF, some scattered small-sized PF, as well as common fish remain (this study; Krijgsman et al., 2001). The same stratigraphic level in the more marginal Rio Aguas section turn out to be barren of micro and nannofossils, including the reworked one; this further supports a taphonomic bias rather than the instauration of hostile conditions as the cause for the absence of the marine calcifiers.

The generally low abundance of foraminifera and CN in the PLG unit interval can be interpreted as the result of either cyclically hostile condition in the water column and/or of a variable dissolution phenomenon. The two explanations are not mutually exclusive and, since we record a fossil assemblage indicative of an unstable environment (see 4.4 paragraph), we can infer that both the presence of an unstable environment and taphonomic processes played a role controlling the composition of the recorded fossil assemblages.

3.2 The aragonitic laminae

Today, aragonitic needles can precipitate directly from the water column forming the so called “whiting events” in several marine settings; the most famous area is the Great Bahamas Bank

(Shinn et al., 1989; Robbins and Blackwelder, 1992; Milliman et al., 1993; Robbins et al., 1997); but they were also documented in karst marine lakes of the Mediterranean region (Mljet Lakes, Croatia; Sondi and Juračić., 2010). Several evidences indicates that aragonite needle precipitation in seawater could be biologically-induced by algae bloom (Robbins and Blackwelder, 1992; Obst et al., 2009; Swart et al., 2009; Swart et al., 2014; Sondi and Juračić., 2010) decreasing the local $p\text{CO}_2$, increasing the alkalinity content of the seawater and thus favouring the precipitation of calcium carbonate (calcite and aragonite) (Larson and Mylroie, 2014). Virus-induced rupturing of cyanobacteria is also capable of releasing intracellular bicarbonate and inducing the homogeneous nucleation of aragonite (Xu et al., 2019). Localised aragonite precipitation can also take place within Extracellular Polymer Substance (i.e. EPS) (Thompson, 2000; Obst et al., 2009) produced by picoplankton, phytoplankton and green algae (Yates and Robbins, 1998). Aragonite can be also bio-produced by different algae and corals taxa, but in different shape with respect to the aragonite crystals found in the sediment deposited during withing events (Loreau, 1982; McIntyre and Reid, 1991; Shinn et al., 1989; McIntyre and Reid, 1995). Aragonitic algal (e.g. *Halimeda*) needle usually are from 3 to 10 μm long with sharp-faced crystal and blunt termination, but the majority of aragonite crystal produced by these organisms are in the form of nanograins ($\approx 1 \mu\text{m}$; McIntyre and Reid, 1991). Although a large variety of aragonite shapes exist, in our samples we observed 2 dominant shapes: bladed crystal habits about 10 μm long with pointed terminations, sometimes with radial orientation, and acicular needles usually $< 6 \mu\text{m}$ with blunt termination. A possible producer of the aragonite needle could be the green alga *Halimeda*, widely diffused in the more marginal carbonate platform surrounding the Sorbas Basin at the time of PLG deposition (Roveri et al., 2009; Roveri et al., 2020). We excluded that our aragonitic laminae were formed through erosion and transport of *Halimeda*, because the shape of the aragonite produced by these organisms differs (for detail, see McIntyre and Reid, 1991; McIntyre and Reid, 1995) from the aragonite crystals that we recorded. Visual comparison with previous works rather suggests that the aragonite crystals of cycles PLG display shape and size similar to the Bahamas aragonite (Loreau, 1982, page 39 Fig. d; Shinn et al.,

1989, Fig.9 a, b, c and d; McIntyre and Reid, 1991, Fig.1 a and b; Milliman et al., 1993, Fig.2 a, b and c).

The slight negative $\delta^{18}\text{O}$ values (from -2.28 to -0.25 ‰) of the aragonitic laminae suggest that aragonite did not precipitate from evaporated sea water: in this case positive values (up to 9‰) should be expected (Zieglenblag et al., 2010). The studied aragonite is ^{13}C -enriched ($\delta^{13}\text{C}$ values from +2.49 to +3.56 ‰) compared to today Mediterranean surface water ($\delta^{13}\text{C}$ +0.96 to +1.52 ‰; Pierre, 1999) and Tortonian calcite from Lorca Basin, S-E Spain ($\delta^{13}\text{C}$ -1.8 to +0.2 ‰ Pierre and Rouchy, 2004). Such ^{13}C enrichment could indicate that aragonite nucleated in the photic zone was triggered by intense activity of photoautotrophs, since photosynthesis preferentially remove the ^{12}C causing the water to become enriched in the heavier C isotope (Robbins and Blackwelder, 1992; Swart et al., 2005; Swart et al., 2009). Moreover, it follows that the aragonite was precipitated in the photic zone. The possible photosynthetic organisms are unknown since calcareous phytoplankton fossils were very scarce in this sediment. It could be speculated that some not-fossilized cyanobacteria were responsible for the aragonite precipitation through enhanced photosynthetic activity and/or EPS exudation. Indeed, cyanobacteria can replace calcareous plankton after the impact of extreme event, becoming the major (bio-mediated) carbonate producers, as in the case of the K/Pg aftermath (Bralower et al., 2020). Our interpretation regarding the bio-mediated origin of the aragonite is further supported by 2 additional lines of evidence:

1- The bright autofluorescence of the aragonite laminae, which reflect high contents of organic matter. This organic matter could have been associated with autotrophic activity during intense bloom episode.

2- The longitudinal cracks characterizing the aragonite laminae could be derived from the degradation of EPS, which may have worked as a microenvironment for the aragonite precipitation.

Interestingly, aragonite laminae contain small size pyrite grains < 10 μm (supplementary material, Fig. 6F), which suggest anoxic condition in the water column (Wilkin et al., 1997; Bond and Wignall, 2010; Tagliavento et al., 2020). Such feature argues for stratified water column at this time

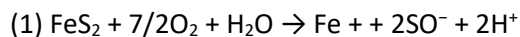
(and the formation of a well-developed chemocline), typified by an oxygenated superficial layer with enhanced photosynthesis separated by a chemocline above an euxinic layer (Wilkin et al., 1997). Stratification is further supported by the planktic and benthic assemblage (see 4.4 paragraph).

3.3 Dissolution of biogenic calcite: The possible mechanisms

Three mechanisms promoting the dissolution of biogenic calcite are here proposed for each taphonomic interval: pyrite and organic matter oxidation and increase in SO₄ content.

Pyrite oxidation (taphonomic interval A and B)

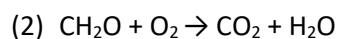
Although diffuse small-sized pyrite (< 10 µm) in marine sediment is indicative of anoxic environment (Bond and Wignall, 2010; Tagliavento et al., 2020), the pyrite infill of foraminifer shells may reflect the reduction of organic matter (i.e. foraminifer cell) through bacterial sulphate reduction in the microenvironment created inside the foraminifer shell (Buckman et al., 2020). However, pyrite precipitation within the foraminifer chambers can occur both in the water column and after burial (Buzas-Stephens and Buzas, 2005; Buckman et al., 2020). The oxidation of pyrite is a process that increase local acidity (Buzas-Stephens and Buzas, 2005; Liu et al., 2018) according to the chemical reaction:



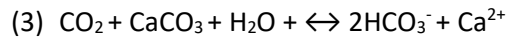
As consequence, this process when occurring within the internal foraminifer shells can promote the dissolution of the calcitic wall (McNeil, 1997). This process is well figured in the studied sediments of interval A and B, in which there are evidences that the oxidised pyritic foraminifer moulds leaves dissolution pits on the internal wall of the formaminifer shells (Fig.2 B2). We thus suggest that this mechanism could have promoted BF and PF dissolution

Organic matter oxidation (taphonomic interval A+B)

Another mechanism that can promote dissolution of biogenic calcite is the aerobic degradation of organic matter according to the reaction



The degradation of organic matter in marine oxygenated pore water led to a decrease in pH due to the production of CO₂ (Archer, 1991), promoting dissolution of biogenic calcite (Archer and Maier-Reimer, 1994; Jahnke et al., 1996; Archer et al., 2003) according to the reaction



This mechanism could have promoted both the CN and foraminifers dissolution

The SO₄ and Mg role (taphonomic interval C)

From a taphonomic point of view, the aragonite preservation and biogenic calcite dissolution evidences (see 4.1 paragraph) could be the two sides of the same coin: aragonite precipitation is favored with respect to calcite at certain Mg/Ca ratio of seawater (at > ~ 0.6–0.7, aragonite becomes the dominant phase; at ~1.7 only aragonite precipitates) (Moerse et al., 1997; Bots et al., 2015). Mg substitution in the calcite crystal lattice is in function of the Mg/Ca content and temperature (Burton and Walter, 1991), which ultimately control the thermodynamic stability of calcite (Davis et al., 2000). Bots et al. (2015) showed that an increase in dissolved SO₄ decreases the Mg/Ca ratio at which calcite is destabilized and aragonite becomes the dominant CaCO₃ polymorph. We thus suggest that the aragonite preservation and the poorly preserved biogenic calcite recorded in the taphonomic interval C mirrored an increase in Mg and SO₄ content.

3.4. The fossils content of the PLG and their paleoenvironmental indications

The common presence of intact coccosphere in the PLG unit and the low abundance of reworked CN is an indication of a generally autochthonous assemblage (Fig.1). Overall, little paleoenvironmental information can be obtained by the CN assemblage recorded in the PLG unit, because the variation in the assemblage diversity vary mostly according to preservation (see 4.1.3 paragraph).

However, the presence of some peculiar feature, such as the presence of intact coccosphere, fecal pellet and fish remains, undoubtedly point to the presence of marine water during the PLG interval. Marine fossils (fish, echinoids, bivalve, bryozoan and gastropods) were

widely recorded in this interval in the nearby shallower equivalent section (Los Yesos, Montenat et al., 1990; Saint Martin et al., 2001; Goubert et al., 2001; Néraudeau et al., 2002) and basins (Carboneras-Nijar Basin, Van de Poel, 1992). In some case, fish remains constitute the dominant fraction of the residue (Van de Poel, 1992).

The marl intervals of cycles PLG1 and PLG2 sampled in the Perales section are devoid of calcareous microfossils, which are instead observed from cycle PLG3 of upward (Los Molinos), corresponding to the inception of the taphonomic interval C. In the PLG4 the BF > 125 µm were mostly absents, except in 2 samples in which Bolivinids and *Ammonia* were recorded. The presence of fish remain in this level suggests a well-developed marine food web at this time. In the middle part of the marly PLG6 hemicycle, *Fursenkoina fusiformis* specimens are common, though often fragmented. *Fursenkoina fusiformis* is an opportunistic shallow infaunal species which is associated to high organic carbon supply to the sea floor, even though it can be susceptible to oxygen deficiency (Barmawidjaja et al., 1992; Alve, 1994). Its depth preference can be variable and probably rely on the organic carbon content of the sea floor (e.g it was found living at less than 40 m depth in the North Adriatic Sea in front of the Po delta; Barmawidjaja et al. 1992); this genus is further associated to the Oxygen Minimum Zone in the Northern Indian Ocean (Mazumder et al., 2014). Among its ecological features, it is worth noting the ability to recolonize previously anoxic sea floor on the shelf (Alve, 1994).

Upward in the section, in cycle PLG7, BFs became less frequent and often only present in the < 125 µm. The assemblage composition still indicates a high organic carbon content in the sediment (bolivinids, bulimind, uvigerinids and *Globobulimina*), although the few observed specimens could suggest a strong dissolution bias or reworking from pre-evaporitic deposits.

Worth noting is also the occurrence of *Criboelphidium* and *Ammonia* individuals that could indicate a shallowing of the water column (Fig.1). From the PLG9 upward we recorded an increase in carbonate content expressed by the presence of several limestone layer intercalated to laminated marls. The progressive transition from predominant marly intercalation to limestone is interpreted

as a shallowing of the basin (Roveri et al., 2020) leading to a more proximal position with respect to the adjacent carbonate platforms (i.e. TCC) . These limestone layers are sandwiched between the gypsum and are considered to be the proximal lateral equivalent of the distal laminated marls (Lugli et al., 2010).

The shallowing upward trend is confirmed by the rather common occurrence of miliolids, probably representative of the *Quinqueloculina* genus, intercalated with levels yielding valves of the shallow water ostracod *Cyprideis* in the marly interval of cycle PLG9 (Fig.1). *Quinqueloculina* is an epifaunal taxa often associated with hypersaline lagoons, marine marsh or inner shelf setting (Murray, 2006); together with the presence of *Cyprideis* valves it suggests the instauration of euryhaline conditions and the generalized decline of the organic matter content of the sea floor with respect to the lower PLG cycles. Previous studies indicated a paleodepth spanning from 150-240 meters depth at the Abad/Yesares transition (Dronkert, 1976; Troelstra et al., 1980; van de Poel, 1992; Riding et al., 1998; Baggley, 2000; Clauzon et al., 2015; Modestou et al., 2017), and to 75-100 meters at the Yesares/Sorbas transition (Krijgsman et al., 2001; Roveri et al., 2020). BF assemblage composition are in agreement with the shallowing upward trend; however, the presence of miliolids, *Ammonia*, *Elphidium* and *Cyprideis* suggests a shallower water depth (less than 75 m) and compatible with a shallow lagoonal environment (see also Van de Poel, 1992), characterized by excursion from brackish to hypersaline water, thus indicating a restricted connection with the open sea.

Cycles PLG11 and 12 are prevalently barren, except the uppermost sample of cycle PLG11, where open marine PFs are mixed with *Ammonia*, *Elphidium* and miliolids, suggesting that the latter are probably reworked from pre-evaporitic sediments and transported in a shallow setting, similar to that envisaged from PLG9.

Generally, in the Los Molinos section CN indicate the presence of an upper water column strongly influenced by the continental runoff, suggested by the presence of freshwater sensitive taxa such as *H. carteri*, *Sphenolithus* gr. and *C. pelagicus* (Giraudeau et al., 1992; Silva et al., 2008; Auer et

al., 2014; Mancini et al., 2020). The presence of normal marine assemblage in the upper water column and a mixed assemblage at the sea floor (i.e. indicative of both high salinity fluctuation and high organic carbon rain), suggests a vertical separation of the water mass by stratification, probably governed by the presence of a well-developed pycnocline.

Summarizing, we recorded a calcareous fossil assemblage indicative of restricted marine condition attributable to a deep lagoonal system punctuated by more open marine episodes. The generally low abundance of calcitic fossils was likely the combination of both dissolution phenomena affecting the paleontological record during (shallow) burial and the influence of an unstable environment, similar to lagoonal environment.

3.5 Paleoenvironmental processes leading to the calcitic fossil dissolution

The mechanisms that control the preservation of calcitic fossil in the sedimentary record were previously listed (pyrite and organic matter oxidation and increase in Mg and SO₄ content; see paragraph 4.3); in this paragraph we propose the causal mechanism that led to decrease in preservation of calcitic fossil in the 3 recognised taphonomic intervals (4.1 paragraph)

The empty cavities observed between the pyrite aggregate and the surrounding sediment recorded in the taphonomic interval A (Fig.2 A3) were the results of post depositional dissolution of the foraminifer calcitic wall; we can thus infer that calcite dissolution took place during diagenesis, after burial. However, it is still unclear which mechanisms promoted the increase of pyrite growth and its successive oxidation toward the MSC onset and its maximum efficiency in the second limestone layer of UA34. Similar increasing pattern were recognised also for the organic matter accumulation: the basin restriction step dated at ~ 6.7 Ma promoted the cyclical preservation of organic carbon at the precessional scale (i.e. sapropel deposition), marking the LA/UA boundary (Sierra et al., 2001; Sierra et al., 2003). Similarly, toward the MSC onset we recorded an increase in organic matter accumulation (i.e. the cycle UA34 is mostly composed by sapropel-like layers; Mancini et al, 2020) as a results of a basin restriction step marked by the MSC onset bioevent. In this

regard, we can infer that the foraminifer dissolution was related to the progressive restriction of the Mediterranean Basin: toward the MSC onset, an increase in the marginal basins susceptibility to external forces, such as (seasonal) variation in the freshwater input and temperature, occurred. The basin restriction likely resulted in a more marked climate-induced alternance between oxygenated/anoxic sea floor, promoting pyrite production and organic matter preservation during anoxic phases (Fig. 7A), and their successive oxidation during oxygenated conditions (Fig.7B). This mechanism could explain the progressive foraminifer and CN dissolution toward the MSC onset (taphonomic interval A and B, Fig.7A and Fig.7B). Similar seasonal dissolution pattern affecting calcareous fossil related to the pyrite and organic matter oxidation was early reported in salt marshes sediments at Indian Neck, Connecticut (Raeves, 1986).

Differently, in the taphonomic interval C the presence of aragonite and the poor preservation of calcitic fossil could be related to an increase in the Mg and SO₄ content (paragraph 4.3).

Although the exact sources of Mg and SO₄ is not clear, it could be inferred that an increase in the Mg and SO₄ during the PLG deposition occurred as a result of the basin restrictions, which increased the continental run-off influence in the receiving basin, promoting the concentration of these elements (Fig. 8). The CN assemblage recorded in the taphonomic interval C could supports the hypothesis that the SO₄ and the Mg were river-delivered, since fresh water sensitive taxa (*H. carteri*, *Sphenolithus* gr. and *C. pelagicus*, according to Giraudeau et al., 1992; Silva et al., 2008; Auer et al., 2014; Mancini et al., 2020) were common in certain levels (Fig.1). This mechanism finally favoured the precipitation of aragonite, biogenic calcite dissolution, and/or cessation of biocalcification.

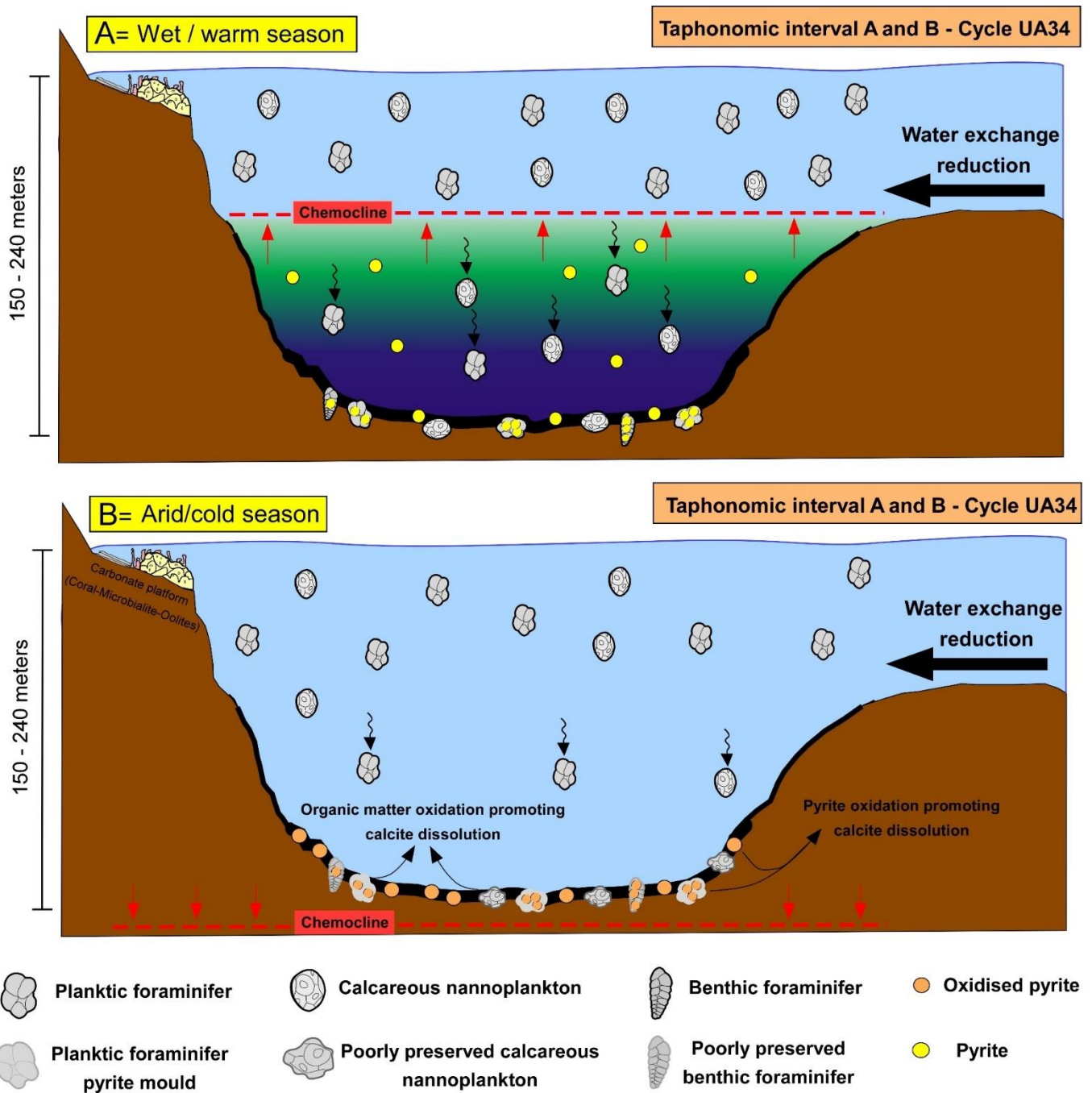


Fig.7: Schematic representation of the main mechanisms that promoted the observed dissolution pattern and the consequent disappearance of calcareous fossils.

A: During the wet/warm season, the enhanced freshwater input caused density stratification of the water mass. The sinking organic matter promoted the instauration of bottom anoxic condition and the establishment of a chemocline that separated oxygenated water at the top and anoxic/euxinic bottom water. Below the chemocline, abundant pyrite precipitated and sunk to the bottom. Pyrite was also formed in the microenvironment produced within the foraminifer shell as a by-product of the microbial sulphate reduction.

B: During the arid/cold season, the decrease in temperature and the reduced freshwater input caused a vigorous mixing in the water column, resulting in a down-ward migration of the chemocline below the sea floor. This mechanism promoted the oxidation of both organic matter and pyrite, which ultimately promoted the dissolution of the previously deposited biogenic calcite.

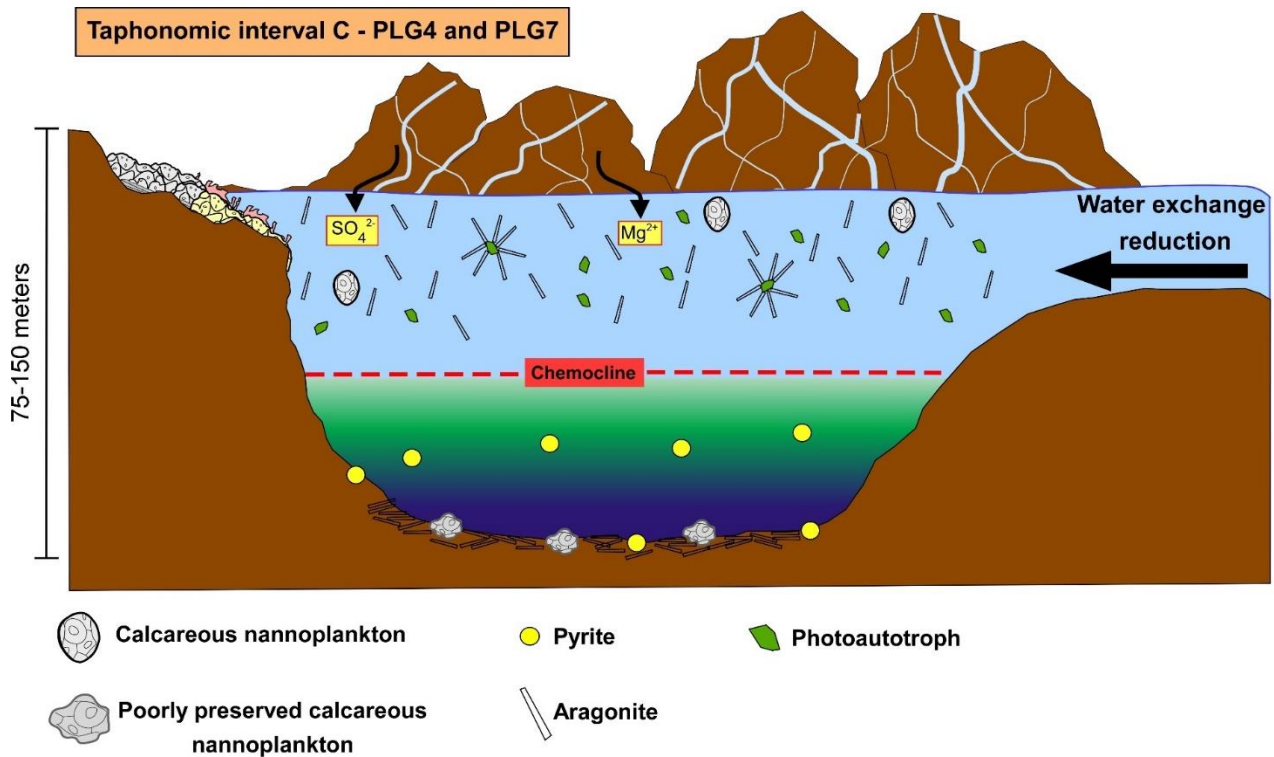


Fig.8: Schematic representation of the main mechanisms that promoted the aragonite deposition and dissolution pattern affecting the biogenic calcite. The ongoing basin restriction resulted in an increased concentration of river-delivered Mg and SO_4 ions. The increase in Mg and SO_4 favoured the precipitation of aragonite and destabilised the biogenic calcite.

Conclusion

Micropaleontological, mineralogical, and isotopic characterization of the sediment spanning the MSC onset and its first phase were performed in order to describe the main paleoceanographic and paleoenvironmental processes occurred at this time. Specifically, our goal was to shed light on the causes that led to the calcareous fossils disappearance, commonly used as a marker approximating the MSC onset and usually inferred to be the result of hypersaline condition in the water column. By comparing micropaleontological and petrographic results, 3 taphonomic interval

were detected in our studied section. The pre-evaporitic interval A corresponds to the time before the calcitic fossil disappearance and it is characterised by a increasing upward dissolution pattern that affects in sequence PF, CN, and BF in order of decreasing dissolution susceptibility. This dissolution pattern agrees with the sensitivity to the dissolution of the different taxa reported in literature. In this interval we did not record any evidence of a salinity increase, rather the abundant presence of *Sphenolithus gr.* and *H. carteri* during the MSC onset bioevent records a decrease in the water salinity. The taphonomic interval B was characterised by the disappearance of calcitic fossils at the optical microscope investigation; this also involves the specimens reworked from older stratigraphic intervals. However, some peculiar features, such as pyrite aggregate resembling foraminifer shape, were recognized through SEM inspection. This feature indicates that bio-calcifiers thrived at this time and their “disappearance” at the optical microscope investigation (both of the residue and smear slide) was related to a taphonomic bias. The taphonomic interval C marks the re-appearance of calcitic fossils and was characterised (excluding some cases) by the presence of a poorly preserved and low abundant fossil assemblage. In this interval, laminated sediments mostly composed of aragonite needle were recorded and interpreted as the results of bio-mediated precipitation by autotrophic organisms, as supported by isotopic, compositional, petrographic and morphological evidence. The poorly preserved and scarce calcitic fossils content could be related to both the unstable condition characterizing the environment in which the PLG deposited and with an increase in (river-delivered) Mg and SO₄ content. The presence of fecal pellets, intact coccospheres and sharp compositional changes in the assemblage (e.g. Miliolids appearance in the PLG9) indicated that the fossil content was mostly autochthonous and indicative of restricted marine conditions. Overall, the fossil assemblage of the PLG records a shallowing upward trend from PLG9 upward with the instauration of a lagoon-like environment, characterised by strong environmental fluctuation modulated by freshwater input. Comparing the benthic assemblage characterised by the presence of euryhaline taxa (i.e. *Cyprideis*, *Ammonia*, Miliolids and *Elphidium*) and planktic assemblage characterised by possibly low salinity taxa (*Sphenolithus gr.*, *H. carteri* and *C. pelagicus*), suggests the

presence of a stratification in the water column at this time. We conclude that approaching and during the first phase of the MSC the micropaleontological content is affected by a severe taphonomic bias related to the ongoing restriction of the basin.

Supplementary material

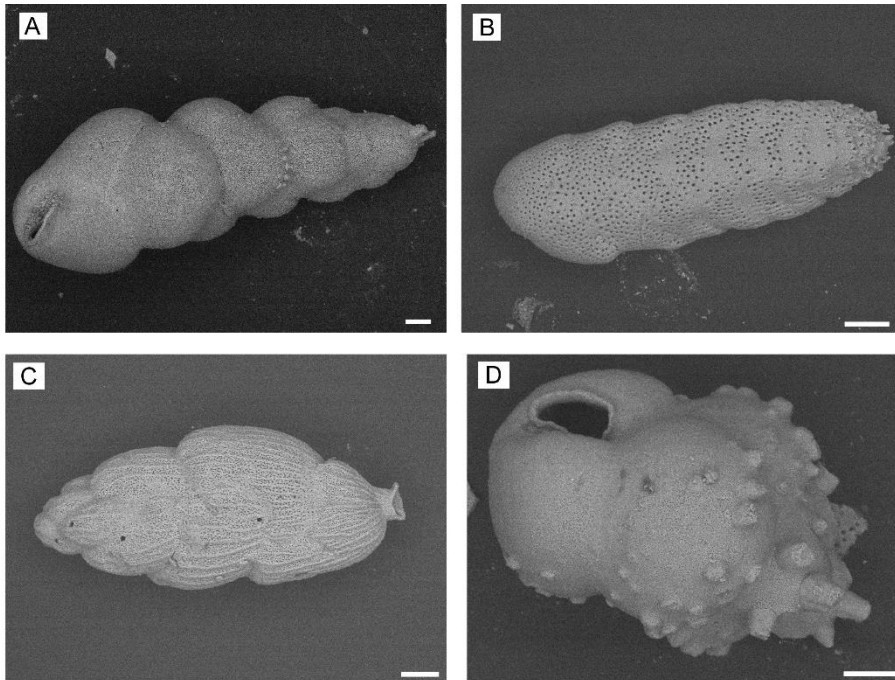


Fig.1: Different hand-picked foraminifers belong to the UA (from UA23 to UA31) showing good preservation of the calcite wall. The foraminifer preservation in this interval is generally good. Scale bar is 50 μm

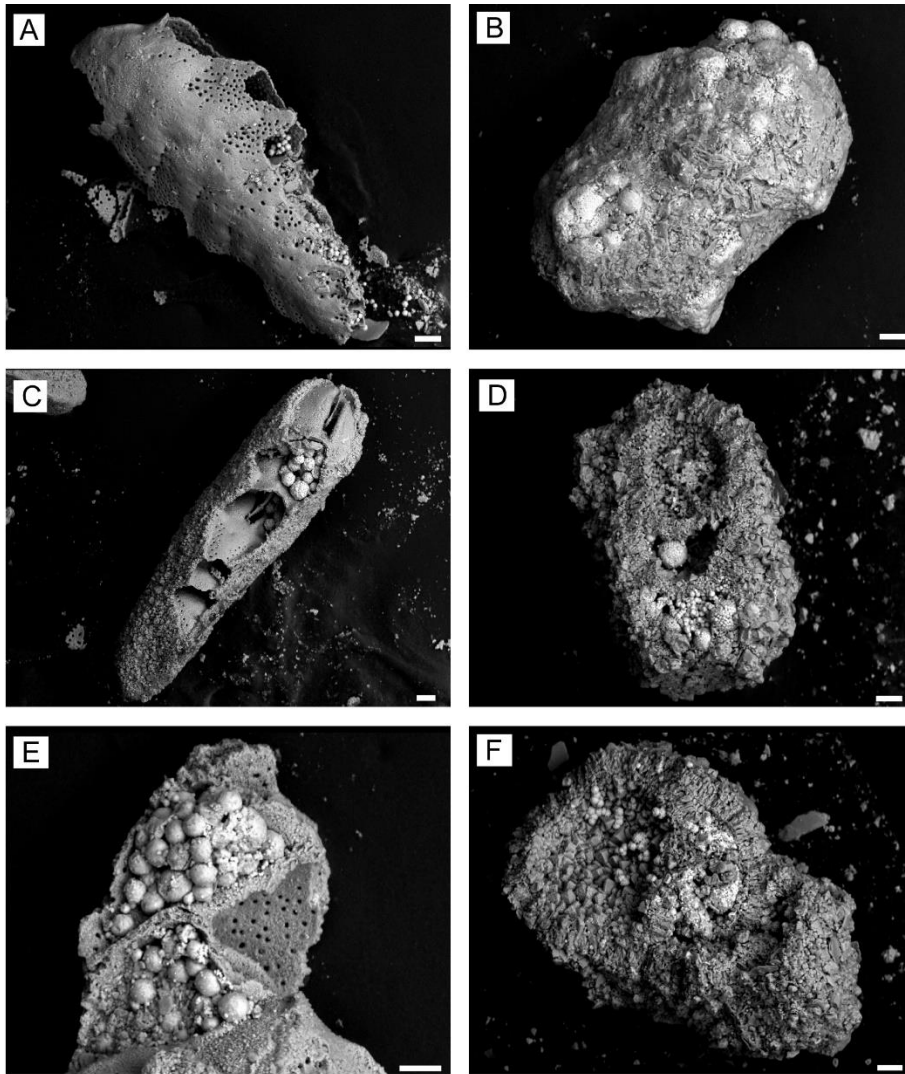


Fig.2: SEM images of hand-picked benthic foraminifers belonging to the taphonomic interval A (sample A2). These foraminifers show high dissolution features related to the pyrite growth inside the foraminifers chambre and its successive oxidation. Encrustations features by caclitic mineral are also recognizable (B, C, D, E and F). Calcite mineral infill associated with pyrite are present in D, E and F. Scale bar is 20 μ m

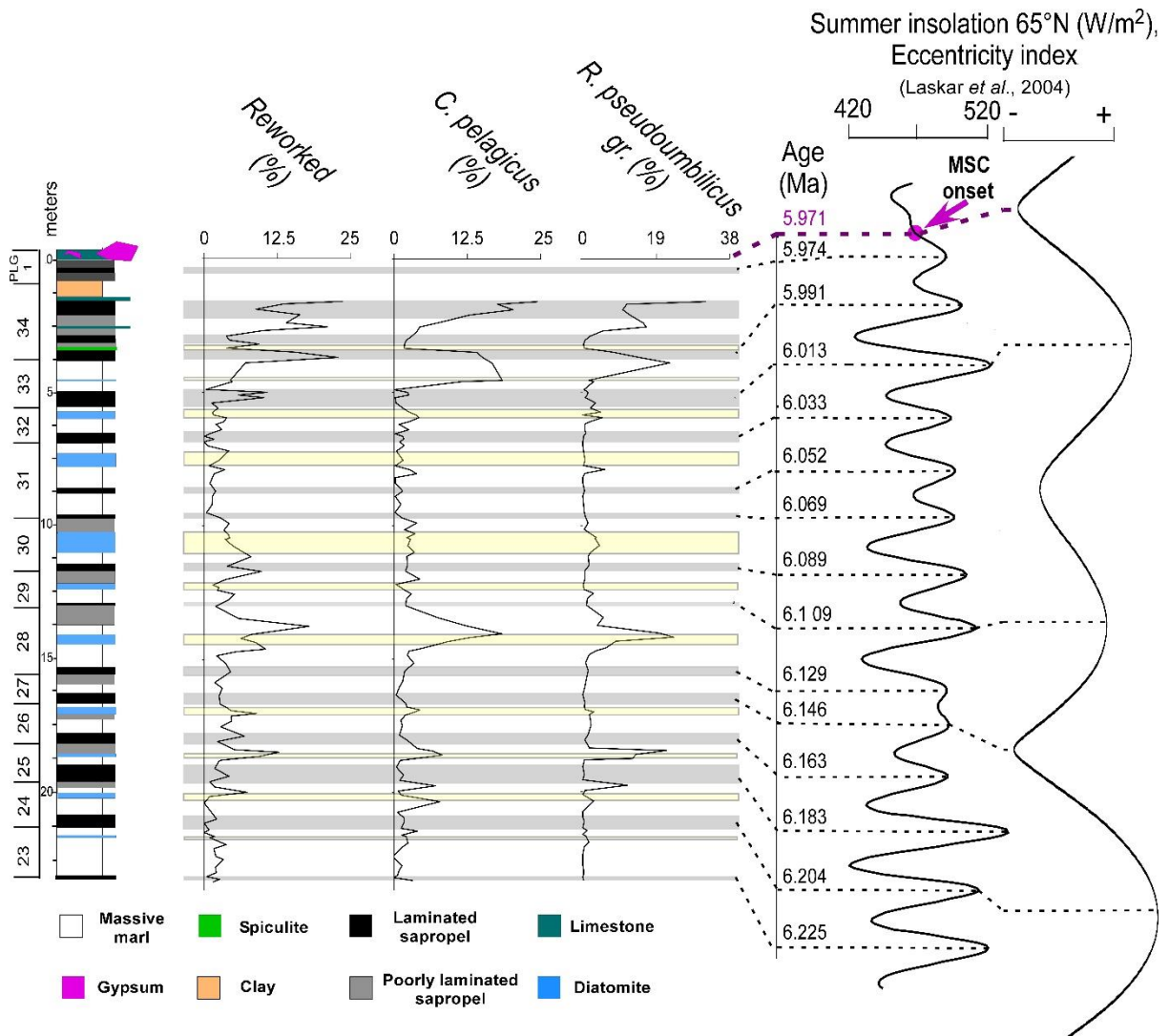


Fig.3: Calcareous nanofossil relative abundance recorded in the upper Perales section (Mancini *et al.*, 2020). Note that the dissolution resistant taxa *C. pelagicus* and *R. pseudumbilicus* gr. (Gibbs *et al.*, 2004) reached the maximum abundance at the top of the cycle UA34.

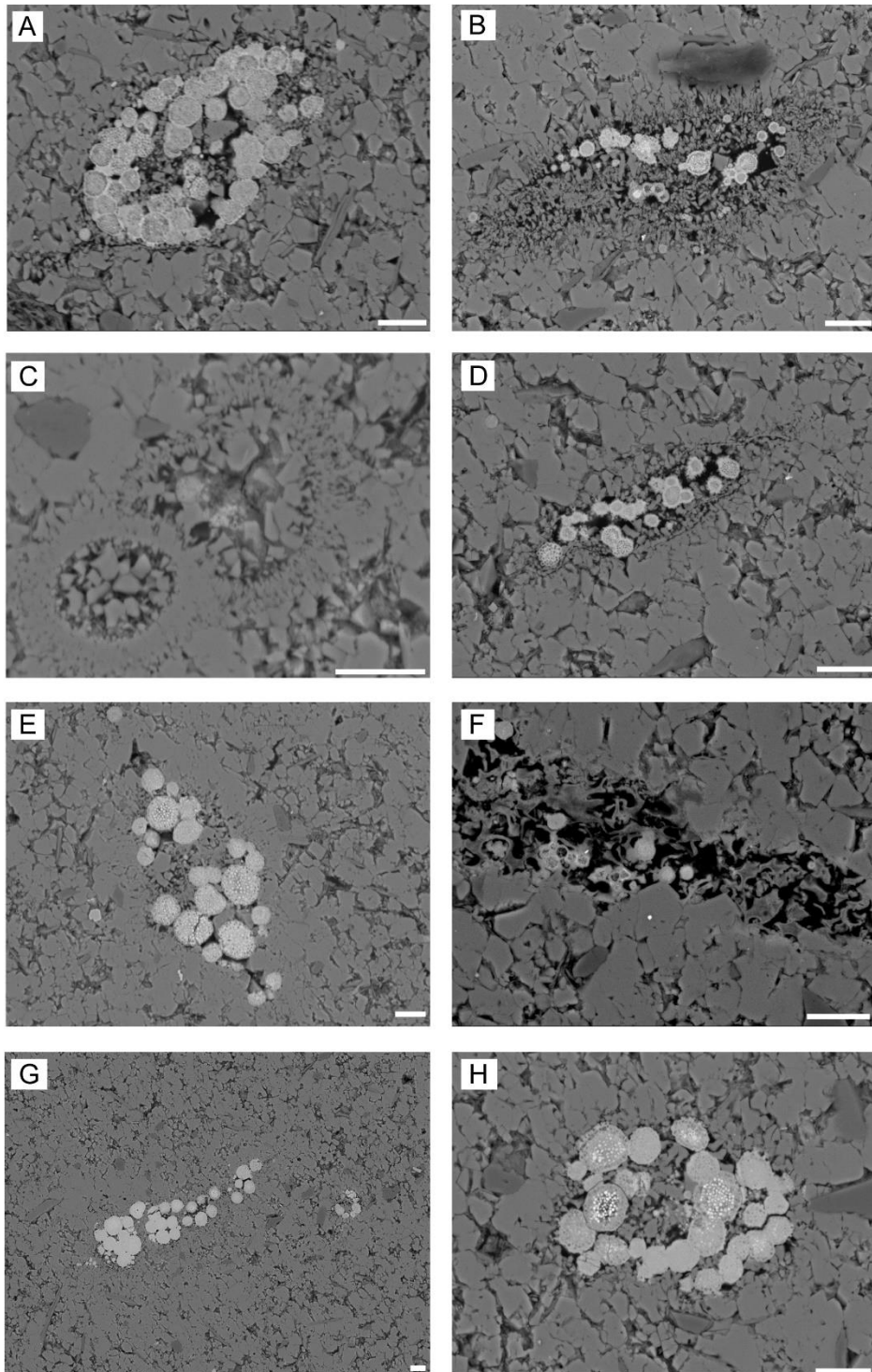


Fig.4: SEM images of thin section belonging to the taphonomic interval B (sample B3, in the text referred as the second limestone layer of UA34). Aggregate of pyrite associated with calcite (A, B, C D, E, G and H) or phosphatic mineral (F) resembling biological shape. Scale bar is 20 μm

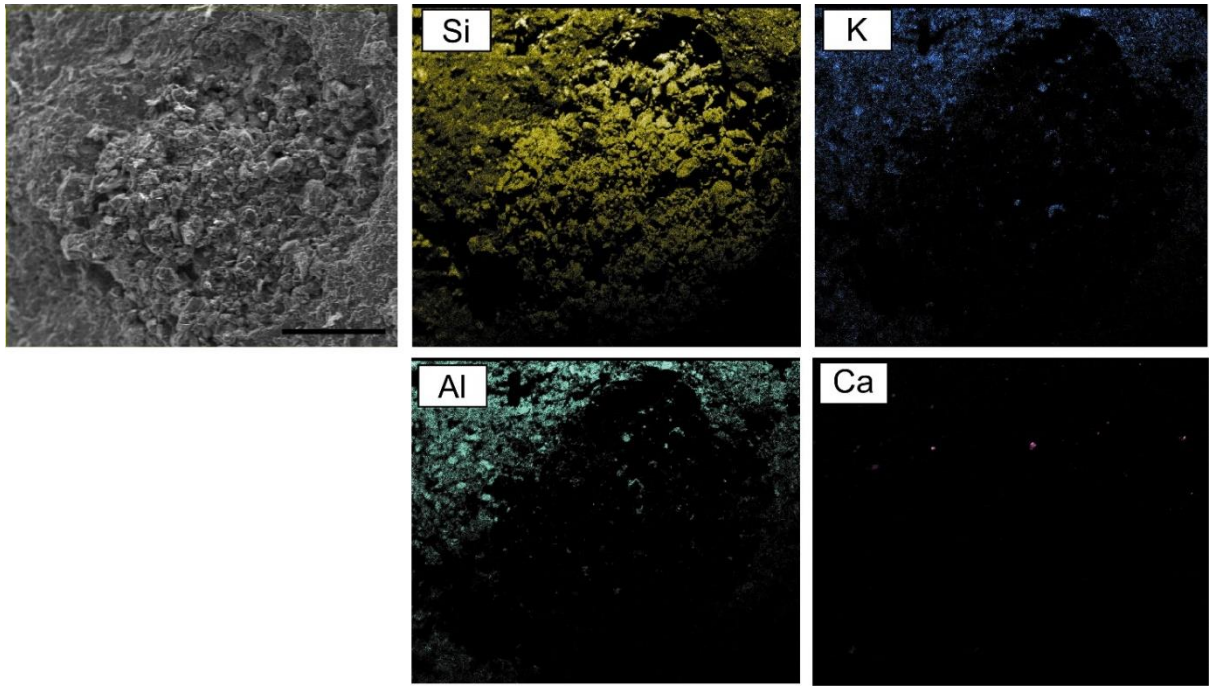


Fig.5: Elemental composition performed with the SEM of the blue/grey level marking the inception of the taphonomic interval C. The first image is the reference picture. Hole filled with quartz mineral in a siliciclastic matrix; note that the Ca content is nearly absent. The scale bar is 300 μm

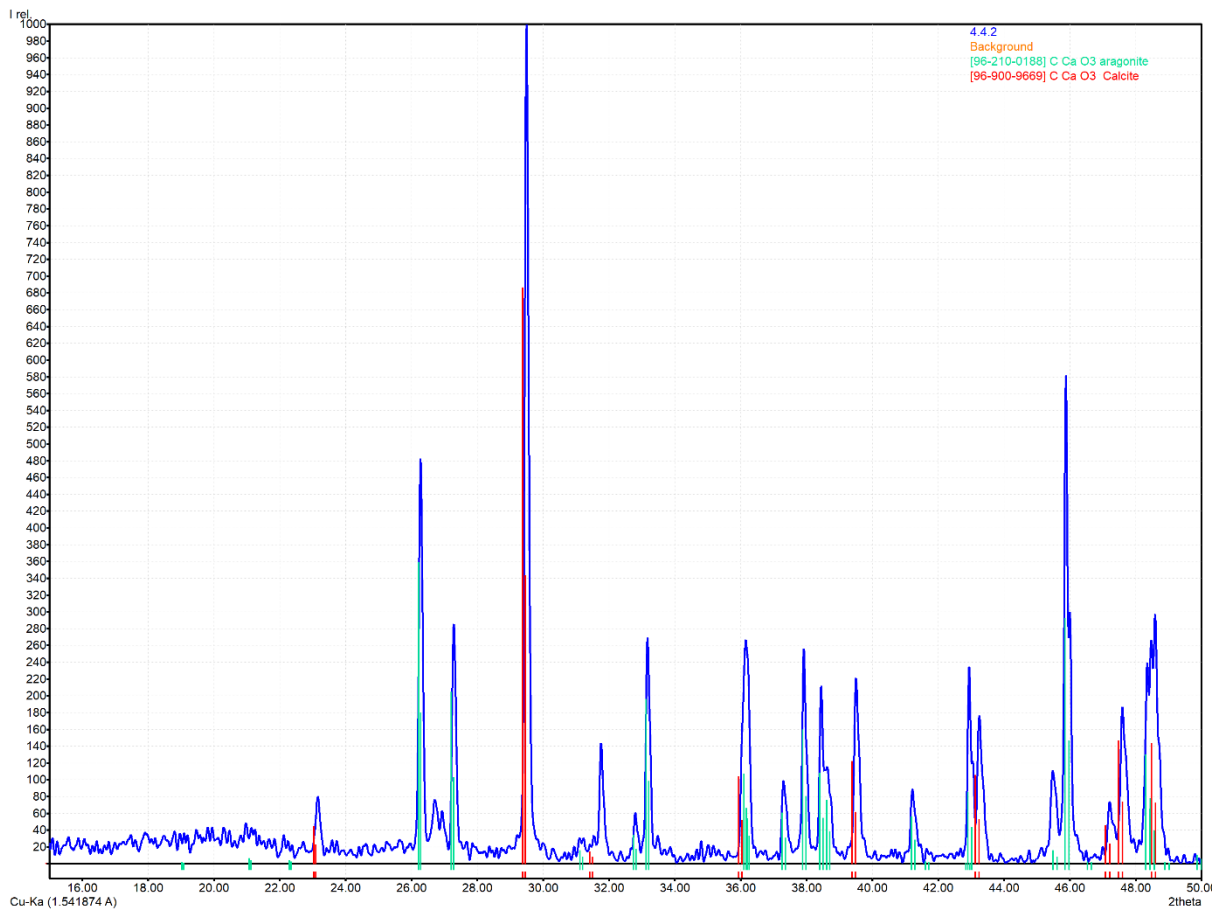


Fig.6: XRPD pattern of the sample PLG4 demonstrating the presence of aragonite (green markers) associated with calcite (red markers).

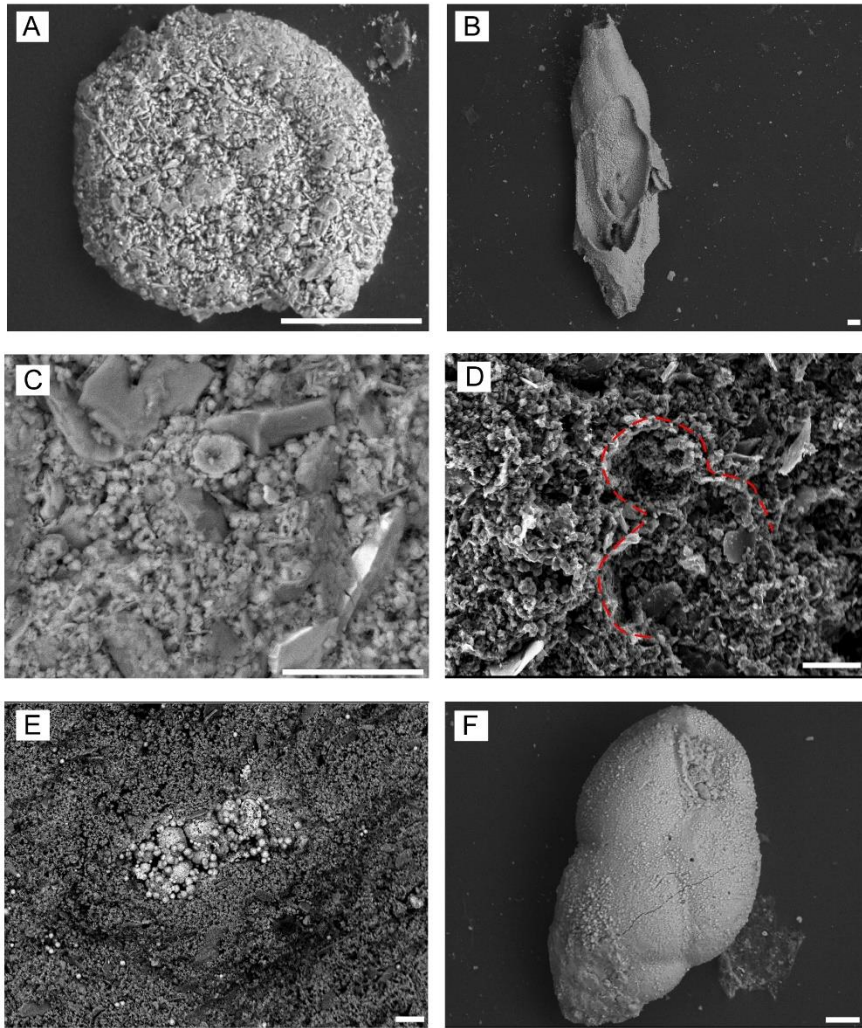


Fig.7: SEM images of freshly broken surface sediment (C, D, and E) and hand-picked foraminifers (A, B and F) belonging from the taphonomic interval C (Los Molinos section). Encrustation (A), dissolution and fractures (B) and cracks (F) features are discernible on hand-picked foraminifers. C: Calcareous nanofossil showing poor preservation state. E: Pyrite aggregate and diffuse in the sediment matrix. Scale bar is 20 μ m

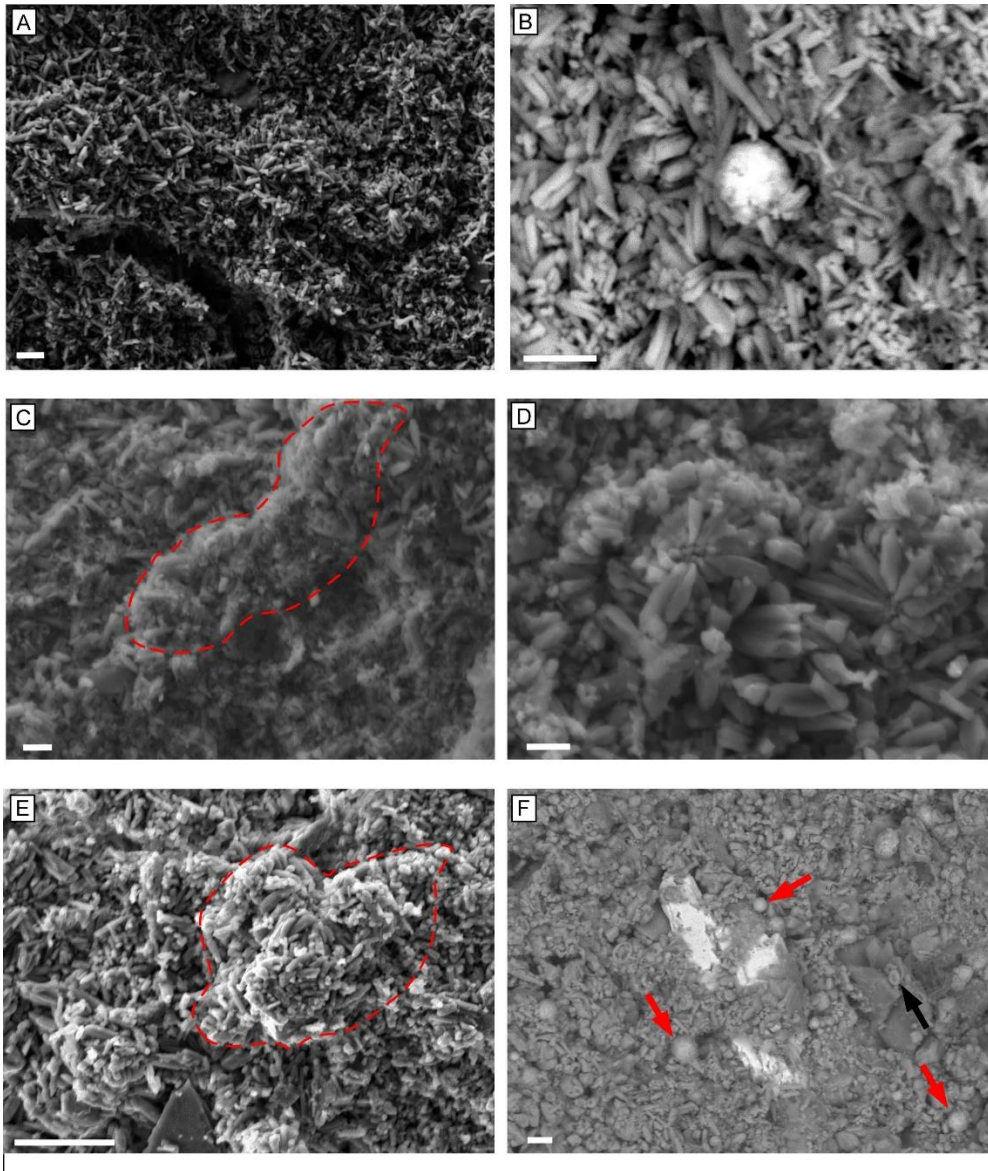


Fig.8: Electron microscope photographs of some representative sample of PLG4 and PLG7. A: Overview of an aragonitic laminae; note that this lamina is mostly composed by aragonite. B: Small size pyrite embedded in aragonitic matrix; note that on the left, aragonite with bladed crystal habit with pointed termination prevail, on the right acicular needles prevail. C and E: Aragonite peleoid. D: Radial bladed aragonite. F: Celestite mineral is discernible in the centre; red arrow indicates small size pyrite. Note sparse coccoliths (dark arrow). Scale bar is 5 μm

Future research and perspective

The achieved conclusion regarding the triggering mechanism of the Messinian sapropels opens new perspective on the possible future impact on the Mediterranean ecosystem under the current warming; in this section I suggest how the current knowledge about the sapropel deposition can be used to eventually predict future impact scenario at the Mediterranean Basin scale.

Some important differences emerged by comparing the Messinian sapropel of the Sorbas Basin with the most recent Holocene-Pleistocene sapropel. These differences are:

- 1- The Messinian sapropel deposited also in the West Mediterranean. The Messinian sapropel of the Sorbas Basin were deposited at shallow depth (the depocenter of the pre MSC Sorbas Basin was estimated at ≈ 150 -200 m depth); their deposition was triggered by an increase in marine productivity in a relatively cold context. In the upper part of the sapropel, the environmental condition progressively shifted to more humid/warmer and the bottom anoxic condition were maintained by the organic matter rain sinking from a well developed DCM.
- 2- The Holocene-Pleistocene sapropels deposited only in the Eastern Mediterranean and they have been found at water depth > 300 -400 m (Rohling et al., 2015 and reference therein), except in one case in the Aegean Sea where S1 was found at 120 m depth (Perissoratis and Piper, 1992). The Holocene-Pleistocene sapropel were deposited after a “preconditioning” period (for the younger sapropel S1 it lasted 1000 yrs; Rohling et al., 2015) of the Eastern Mediterranean water masses due to African Monsoon intensification, which resulted in an increase in the Nile rivers runoff in the Mediterranean Basin (Rohling et al., 2015). This enhanced runoff weakened or stopped the thermohaline circulation of the deepwater masses which became stagnant and anoxic (Rohling et al., 2015).

Basically, the Sorbas Basin sapropel were deposited as a result of enhanced productivity which formed an Oxygen Minimum Zone, similar to what is observed in modern setting such as the coast of Perù (Brodie and Kemp, 1994), California (Schimmelmann and Lange, 1987) and along the Northeastern Arabian Sea (Lückge et al., 2002); the Holocene-Pleistocene sapropel were deposited

due to a weakening/stopping of the thermohaline circulation, responsible for providing oxygen delivery to the sea bottom. These two mechanisms that finally result in anoxic bottom condition, may represent a keystone for better constrain the causes and the effects of one of the major anthropogenic alteration that we are observing nowadays: the Ocean deoxygenation. Indeed, the Ocean deoxygenation is mainly related to an increase in both river-sourced fertilisation (eutrophication) and (rising) temperature, these conditions can be compared to the Sorbas Basin sapropel (eutrophication) and to the more recent sapropel S1 (increase in temperature and river runoff).

The alkenones-based sea surface temperature record on the latest pre MSC onset precessional cycle reveals a temperature range either of $\approx 20\text{-}25^\circ\text{C}$ (Kalamaki section, Greece; Vasiliev et al., 2019) or $24\text{-}28^\circ\text{C}$ (Monte dei Corvi, central Italy; Tzanova et al., 2015). Differently, in the Sorbas Basin the Mg/Ca performed on foraminifer tests (this thesis) showed a sea surface temperature spanning $9\text{--}19^\circ\text{C}$; this inconsistency most likely arose because different sites were analysed with different proxies. Indeed, one methodology rely on organic molecules produced by Haptophytes algae (i.e. alkenones; Herbert et al., 2003), thus reflecting the temperature change of the photic zone; the other rely on the premise that the seawater temperature is the primary control on Mg^{2+} incorporation in the foraminiferal calcite shell during the calcification process (Lea et al., 1999; Elderfield and Ganssen, 2000; Erez, 2003; Barker et al., 2005), that can occur well below the photic zone (Herbert, 2003). Therefore, the temperature values obtained from the Mg/Ca are affected by enhanced variability compared to the alkenone (Herbert, 2003). Furthermore, the temperature obtained from the Mg/Ca method were consistently cooler then the alkenone during the last 270 Kyr in the Atlantic (Nürnberg et al., 2000; Herbert, 2003). Finally, assuming for the Messinian period a similar sea surface temperature pattern of the today Mediterranean, the northwestern Mediterranean is more affected by seasonal temperature contrast (from 10 to 21°C) compared to the southeastern basin (15 to 26°C) (Rohling et al., 2015; Naval Oceanography

Command, 1987). This could explain the discrepancies between the Messinian sea surface temperature obtained from Mg/Ca and from the alkenone at different sites.

In the Mediterranean, the spatial distribution of 30-years (1986 – 2015) average SST span from 16 to 22°C with an increasing trend about 0.4°C per decade (Sakalli, 2017). This warming trend impacted the oceanic realm through multiple and complex dynamics, among these the decrease in the oxygen solubility in water, the increase in stratification episodes and the reduced thermohaline circulation ultimately resulted in the deoxygenation of the Mediterranean water (Somot et al., 2006; Coppola et al., 2018; Limburg et al., 2020). Black box model estimated a temperature increase of about 5.8°C from modern values during the time period 2071 – 2100 (Sakalli, 2017). The SST predicted for the 2100 in the Mediterranean could fit with the SST obtained for the Messinian (Tzanova et al., 2015; Vasiliev et al., 2018; Mancini et al., 2020), making the cyclical Messinian (precession-driven) warming phases a plausible analogue scenario for the near future Mediterranean warming. Despite the rate of warming is clearly not comparable between the natural precession-driven (extremely slow) and the anthropogenic one (extremely fast), important information regarding the ecosystem response could be achieved and extrapolated for predicting future impact scenarios. When the rate of changing environmental condition is relatively low (Messinian case), the ecosystem could respond and adapt to the newly established condition. In this case, the biodiversity loss is reduced, and the ecosystem resources are not significantly affected. On the opposite, fast changing environmental conditions can finally result in a loss of both biodiversity and ecosystem function. In the Sorbas Basin, during precession-driven warming phases, a progressive loss of benthic bioturbation feature was recorded (Pilade et al., in progress); this situation exacerbates along with the increase in temperature and freshwater input and culminates with the complete disappearance of benthic organisms (inferred either from the absence of bioturbation or of their fossil remains) as a result of severe oxygen deficiency conditions. Extrapolating this information and applying them in the modern Mediterranean context, a major crisis affecting benthic organisms as a consequence of the warming-driven oxygen deficiency should

be expected. The shift toward oxygen loss in some Mediterranean sub basin was already recorded (Coppola et al., 2018; Breitburg et al., 2018) and proved to impact also the plankton community (Batziakas et al., 2020) through reduced growth and reproduction rates, reduced activity levels, increased mortality (both natural and through predation), constrained vertical migration to the oxygenated part of the water column (habitat reduction), shifts in size structure and community composition in favour of smaller individuals and egg-carrying species and altered predator–prey dynamics (Roman et al., 2019). Despite the rate of warming during the Messinian was relatively slow compared to what is observed in modern setting, the impact on the benthic community was quite catastrophic, with possible negative repercussion on the trophic web similar to what is observed in modern ocean in areas affected by deoxygenation (Nixon and Buckley, 2002; Breitburg et al., 2018; Macias et al., 2018; Limburg et al., 2020; Batziakas et al., 2020). Considering the rate of the current anthropogenic warming, the impact on the marine ecosystem will be likely more severe.

Another factor that plays a key role in governing the oxygen availability in the water column is river-sourced fertilisation (Nixon and Buckley, 2002; Viaroli et al., 2015; Breitburg et al., 2018; Batziakas et al., 2020; Limburg et al., 2020). Unfortunately, the river runoff is known to be very difficult to reproduce by models (Douve et al. 2002), even with a 50 km resolution (Hagemann et al. 2004). However, change in river runoff were well recorded in the Messinian marginal basin, and the effect of this change can be reconstructed from the geological record.

Part of my future research will be addressing the potential of the sapropel theme in the geological record for predicting possible future impact scenario at the Mediterranean scale. For this purpose, the complex environmental dynamics that characterised the Messinian precessional cycle need to be explored with an improved sampling resolution and analysed for its micropaleontological, geochemical, petrographic and isotopic content.

References

- Allredge, A. L., Gotschalk, C. C., 1988. Direct observations of the mass flocculation of diatom blooms: characteristics, settling velocities and formation of diatom aggregates. *Deep Sea Res.*, 36, 159-171.
- Aloisi, G., 2015. Covariation of metabolic rates and cell size in coccolithophores. *Biogeosciences*, 12, 4665–4692.
- Alve, E., & Murray, J. W., 1994. Ecology and taphonomy of benthic foraminifera in a temperate mesotidal inlet. *The Journal of Foraminiferal Research*, 24(1), 18-27.
- Alves, T.D., Cooper, M.K.E, Rios-Netto, A.M., 2016. Paleogene-Neogene calcareous nannofossil biostratigraphy and paleoecological inferences from northern Campos Basin, Brazil (well Campos-01). *Journal of South American Earth Sciences*, 71, 143-160.
- Anand, P., Elderfield, H., Conte, M.H., 2003. Calibration of Mg/Ca thermometry in planktonic foraminifera 736 from a sediment trap time series. *Paleoceanography*, 18, 1050.
- Antonarakou, A., Kontakiotis, G., Vasilatos, C., Besiou, E., Zarkogiannis, S., Drinia, H., Mortyn, G. P., Tsaparas, N., Makri, P., Karakitsios, V., 2018. Evaluating the effect of marine diagenesis on Late Miocene pre-evaporitic sedimentary successions of eastern Mediterranean Sea. *Grande-Bretagne: IOP: Earth & Environmental Sciences*
- Archer, D., Maier-Reimer, E., 1994. Effect of deep-sea sedimentary calcite preservation on atmospheric CO₂ concentration. *Nature*, 367(6460), 260-263.
- Archer, D., 1991. Modeling the calcite lysocline. *Journal of Geophysical Research: Oceans*, 96 (C9), 17037-17050.
- Archer, D., 2003. Biological Fluxes in the Ocean and Atmospheric p CO₂. *Treatise on Geochemistry*, 6, 625.
- Athanasίου, M., Triantaphyllou, M.V., Dimiza, M. D., Gogou, A., Theodorou, G., 2015. Zanclean/Piacenzian transition on Cyprus (SE Mediterranean): calcareous nannofossil evidence of sapropel formation. *Geo-Mar Lett.*, 35, 367–385.

- Aubry, M.-P., 1992. Late Paleogene calcareous nannoplankton evolution: a tale of climatic deterioration. In: Prothero, D.R., Berggren, W.A. (Eds.), *Eocene–Oligocene Climatic and Biotic Evolution*. Princeton University Press, New Jersey, 272-208.
- Auer, G., Piller, W.E., Mathias Harzhauser, M., 2014. High-resolution calcareous nannoplankton 747 palaeoecology as a proxy for small-scale environmental changes in the Early Miocene. *Marine 748 Micropaleontology*, 111, 53-65.
- Baggley, K. A. 2000. The late Tortonian-early Messinian foraminiferal record of the Abad Member (Turre formation), Sorbas Basin, Almería, south-east Spain, *Palaeontology*, 43, 1069-111.
- Barker, S., Cacho, I., Benway, H., Tachikawa, K., 2005. Planktonic foraminiferal Mg/Ca as a proxy for past oceanic temperatures: a methodological overview and data compilation for the Last Glacial Maximum. *Quat. Sci. Rev.*, 24, 821-834.
- Barker, S., Greaves, M., Elderfield, H., 2003. A study of cleaning procedures used for foraminiferal Mg/Ca paleothermometry. *Geochem. Geophys. Geosyst.*, 4, 8407.
- Barmawidjaja, D. M., Jorissen, F. J., Puskaric, S. V., & Van der Zwaan, G. J., 1992. Microhabitat selection by benthic foraminifera in the northern Adriatic Sea. *The Journal of Foraminiferal Research*, 22(4), 297-317.
- Batziakas, S., Frangoulis, C., Tsiola, A., Nikolioudakis, N., Tsagaraki, T. M., & Somarakis, S. (2020). Hypoxia changes the shape of the biomass size spectrum of planktonic communities: a case study in the eastern Mediterranean (Elefsina Bay). *Journal of Plankton Research*, 42(6), 752-766.
- Beaufort, L., Barbarin, N., and Gally, Y., 2014. Optical measurements to determine the thickness of calcite crystals and the mass of thin carbonate particles such as coccoliths. *Nature protocols*, 9, 633–42.
- Beaufort, L., Probert, I., de Garidel-Thoron, T., Bendif, E. M., Ruiz-Pino, D., Metzl, N., Goyet, N., Buchet, P., Coupel, Grelaud, M., Rost, B., Rickaby, R. E. M., de Vargas, C. and Rost, B., 2011. Sensitivity of coccolithophores to carbonate chemistry and ocean acidification. *Nature*, 476 (7358), 80-83.

- Bellanca, A., Caruso, A., Ferruzza, G., Neri, R., Rouchy, J.M., Sprovieri, M., 2001. Transition from marine to hypersaline conditions in the Messinian Tripoli Formation from the marginal areas of the central Sicilian Basin. *Sedimentary Geology*, 140, 87-105.
- Blanc, P.-L., 2006. Improved modelling of the Messinian Salinity Crisis and conceptual implication. *Palaeogeography, Palaeoclimatology, Palaeoecology* 238, 349–372.
- Blanc-Valleron, M.M., Pierre, C., Caulet, J.P., Caruso, A., Rouchy, J.M., Cespuglio, G., Sprovieri, R., Pestrea, S., Di Stefano, E., 2002. Sedimentary, stable isotope and micropaleontological records of paleoceanographic change in the Messinian Tripoli Formation (Sicily, Italy). *Palaeogeogr. Palaeoclimatol. Palaeoecol.* 185, 255–286
- Bollmann, J., Herrle, H.O., 2007. Morphological variation of *Emiliana huxleyi* and sea surface salinity. *Earth Planetary Science Letter*, 255 (3–4), 273–288.
- Bolton, C. T. and Stoll, H. M., 2013. Late Miocene threshold response of marine algae to carbon dioxide limitation. *Nature* 500, 558–562.
- Bolton, C. T., Hernández-Sánchez, M. T., Fuertes, M. A., González-Lemos, S., Abrevaya, L., Mendez-Vicente, A., Flores, J.A., Probert, I., Giosan, L., Johnson, J., Stoll, H. and Stoll, H. M., 2016. Decrease in coccolithophore calcification and CO₂ since the middle Miocene. *Nature communications*, 7 (1), 1-13.
- Boltovskoy, E., Scott, D. B., & Medioli, F. S., 1991. Morphological variations of benthic foraminiferal tests in response to changes in ecological parameters: a review. *Journal of Paleontology*, 175-185.
- Bourillot, R., Vennin, E., Rouchy, J.M., Durlet, C., Rommevaux, V., Kolodka, C., Knap, F., 2009. Structure and evolution of a Messinian mixed carbonate-siliciclastic platform: the role of evaporites (Sorbas Basin, South-east Spain). *Sedimentology* 57, 477–512.
- Bown, P.R. and Young, J.R. (1998) Techniques. In: Bown, P.R., Ed., *Calcareous nannofossil biostratigraphy*, Chapman and Hall, London, 16-28.

- Boyle, E.A., Keigwin, L.D., 1985. Comparison of Atlantic and Pacific paleochemical records for the last 215,000 years: changes in deep ocean circulation and chemical inventories. *Earth Planet. Sci. Lett.*, 76, 135-150.
- Braga, J.C., Martín, J.M., Riding, R., Aguirre, J., Sanchez-Almazo, I.M., Dinares-Turell, J., 2006. Testing models for the Messinian salinity crisis: the Messinian record in Almería, SE Spain. *Sedimentary Geology*, 188-189, 131-154.
- Bralower, T.J., Cosmidis, J., Heaney, P.J., Kump, L.R., Morgan, J.V., Harper, D.T., Lyons, S.L., Freeman, K.H., Grice, K., Wendler, J.E., 2020. Origin of a global carbonate layer deposited in the aftermath of the Cretaceous-Paleogene boundary impact. *Earth Planet. Sci. Lett.* 548, 116476.
- Brand, L.E., 1994. Physiological ecology of marine coccolithophores. In: Winter, A., Siesser, A. (Eds.), *Coccolithophores*. Cambridge University Press, Cambridge, 39-49.
- Breitbart, D., Levin, L. A., Oschlies, A., Grégoire, M., Chavez, F. P., Conley, D. J., ... & Zhang, J. (2018). Declining oxygen in the global ocean and coastal waters. *Science*, 359(6371).
- Browning, E. L., & Watkins, D. K., 2008. Elevated primary productivity of calcareous nannoplankton associated with ocean anoxic event 1b during the Aptian/Albian transition (Early Cretaceous). *Paleoceanography*, 23(2).
- Buckman, J., Mahoney, C., März, C., Wagner, T., 2020. The Secret 'After Life' of Foraminifera: Big Things Out of Small. *Minerals*, 10(6), 550.
- Bulian, F., Sierro, F. J., Ledesma, S., Jiménez-Espejo, F. J., & Bassetti, M. A., 2021. Messinian West Alboran Sea record in the proximity of Gibraltar: Early signs of Atlantic-Mediterranean gateway restriction. *Marine Geology*, 434, 106430.
- Burdige DJ. 2007. Preservation of organic matter in marine sediments: controls, mechanisms, and an imbalance in sediment organic carbon budgets? *Chem. Rev.*, 107, 467-85.
- Buzas-Stephens, P., & Buzas, M. A., 2005. Population dynamics and dissolution of foraminifera in Nueces Bay, Texas. *The Journal of Foraminiferal Research*, 35(3), 248-258.

- Cachão, M., Drago, T., Silva, A.D., Moita, T., Oliveira, A., Naughton, F., 2002. The secret (estuarine?) life of *Helicosphaera carteri*: preliminary results. *Journal of Nanoplankton Research*, 24, 76-77.
- Cachão, M., Moita, M.T., 2000. *Coccolithus pelagicus*, a productivity proxy related to moderate fronts off Western Iberia. *Marine Micropaleontology*, 39, 131-155.
- Capella, W., Flecker, R., Hernández-Molina, F. J., Simon, D., Meijer, P. T., Rogerson, M., ... Krijgsman, W., 2019. Mediterranean isolation preconditioning the earth system for late miocene climate cooling. *Scientific Reports*. 9, 3795.
- Carnevale G., Caputo D. & Landini W., 2008. A leerfish (Teleostei, Carangidae) from the Messinian evaporites of the Vena del Gesso basin (Romagna Apennines, Italy): Paleogeographical and paleoecological implications. *Bollettino della Società Paleontologica Italiana*, 47: 169-176.
- Carnevale G., Dela Pierre F., Natalicchio M., Landini W., 2018. Fossil marine fishes and the 'Lago Mare' event: Has the Mediterranean ever transformed into a brackish lake? *Newsletters on Stratigraphy*, 51: 57-72.
- Carnevale, G., Gennari, R., Lozar, F., Natalicchio, M., Pellegrino, L., Dela Pierre, F., 2019. Living in a deep desiccated Mediterranean Sea: an overview of the Italian fossil record of the Messinian salinity crisis. *Boll. Soc. Paleontol. Ital.* 58, 109–140
- Caruso, A., Pierre, C., Blanc-Valleron, M.-M., Rouchy, J.M., 2015. Carbonate deposition and diagenesis in evaporitic environments: the evaporative and sulphurbearing limestones during the settlement of the Messinian salinity crisis in Sicily and Calabria. *Palaeogeogr. Palaeoclimatol. Palaeoecol.* 429, 136-162
- Castradori, D., 1993. Calcareous nannofossils and the origin of eastern Mediterranean sapropels. *Paleoceanography*, 8, 459-471.
- Castradori, D., 1998. Calcareous nannofossils in the basal Zanclean of the eastern Mediterranean Sea: remarks on paleoceanography and sapropel formation. *Proc. Ocean Drill. Program Sci. Results*, 160, 113-123.

- Catalano R., Di Stefano E., Sprovieri R., Lena G. & Valenti V. 2016. The barren Messinian Tripoli in Sicily and its palaeoenvironmental evolution: suggestions on the exploration potential. *Petroleum Geosciences*, 22: 322-332
- Chiu, T. C., & Broecker, W. S., 2008. Toward better paleocarbonate ion reconstructions: New insights regarding the CaCO₃ size index. *Paleoceanography*, 23(2).
- Cita, M.B., Wright, R.C., Ryan, W.B.F., Longinelli, A., 1978. Messinian paleoenvironments. In: Hsü, K.J., Montadert, L., et al. (Eds.), *Initial Reports Deep Sea Drilling Project*, 42, 1003–1035.
- Clauzon, G., Suc, J.P., Do Couto, D., Jouannic, G., Melinte-Dobrinescu, M.C., Jolivet, L., Martinell, J., 2015. New insights on the Sorbas Basin (SE Spain): the onshore reference of the Messinian salinity crisis.
- Coppola, L., Legendre, L., Lefevre, D., Prieur, L., Taillandier, V., & Riquier, E. D. (2018). Seasonal and inter-annual variations of dissolved oxygen in the northwestern Mediterranean Sea (DYFAMED site). *Progress in Oceanography*, 162, 187-201.
- Corbí, H., & Soria, J. M., 2016. Late Miocene–early Pliocene planktonic foraminifer event-stratigraphy of the Bajo Segura basin: A complete record of the western Mediterranean. *Marine and Petroleum Geology*, 77, 1010-1027.
- Corbí, H., Soria, J. M., Lancis, C., Giannetti, A., Tent-Manclús, J. E., & Dinares-Turell, J., 2016. Sedimentological and paleoenvironmental scenario before, during, and after the Messinian Salinity Crisis: The San Miguel de Salinas composite section (western Mediterranean). *Marine Geology*, 379, 246-266.
- Corbí, H., Soria, J.M., Giannetti, A. Yébenes, A., 2020. The step-by-step restriction of the Mediterranean (Start, Amplification, and Consolidation phases) preceding the Messinian Salinity Crisis (Climax phase) in the Bajo Segura basin. *GeoMarine Letters*.
- Corselli, C., Principato, M.S., Maffioli, P., Crudelli, D., 2002. Changes in planktonic assemblages during sapropel S5 deposition: evidence from Urania Basin area, eastern Mediterranean. *Paleoceanography*, 17.

- Crudeli, D., a, Young, J.R., Erba, E., Geisen, M., Ziveri, P., de Lange, G.J., P. Slomp, C.P., 2006. Associations from the Mediterranean (Holocene–late Pleistocene): Evaluation of carbonate diagenesis and palaeoecological–palaeoenographic implications. *Palaeogeography, Palaeoclimatology, Palaeoecology*, 237, 191-224.
- Cuevas Castell, J.M., Betzler, C., Roßler, J., Hüssner, H., Peinl, M. (2007) Integrating outcrop data and forward computer modelling to unravel the development of a Messinian carbonate platform in SE Spain (Sorbas Basin). *Sedimentology*, 54, 423-441.
- D'Amario, B., Pérez, C., Grelaud, M., Pitta, P., Krasakopoulou, E., and Ziveri, P. 2020. Coccolithophore community response to ocean acidification and warming in the Eastern Mediterranean Sea: results from a mesocosm experiment. *Scientific reports*, 10 (1), 1-14.
- D'Amario, B., Ziveri, P., Grelaud, M., Oviedo, A., 2018. *Emiliana huxleyi* coccolith calcite mass modulation by morphological changes and ecology in the Mediterranean Sea. *PLoS One*, 13 (7) 2018.
- Damsté, J. S. S., Frewin, N. L., Kenig, F., & De Leeuw, J. W., 1995. Molecular indicators for palaeoenvironmental change in a Messinian evaporitic sequence (Vena del Gesso, Italy). I: variations in extractable organic matter of ten cyclically deposited marl beds. *Organic Geochemistry*, 23(6), 471-483.
- Danovaro, R. 2018. Climate change impacts on the biota and on vulnerable habitats of the deep Mediterranean Sea. *Rendiconti Lincei. Scienze Fisiche e Naturali*, 29(3), 525-541.
- De La Rocha, C.L., Passow, U., 2007. Factors influencing the sinking of POC and the efficiency of the biological carbon pump. *Deep-Sea Res. II*, 54, 639-58.
- de Lange, G. J., & Krijgsman, W., 2010. Messinian salinity crisis: a novel unifying shallow gypsum/deep dolomite formation mechanism. *Marine Geology*, 275(1-4), 273-277.

- Dedert, M., Stoll, H., Kars, S., Young, J.R., Shimizu, N., Kroon, D., Lourens, L., Ziveri, P., 2014. Temporally variable diagenetic overgrowth on deep-sea nan-nofossil carbonates across Palaeogene hyperthermals and implications for isotopic analyses. *Marine Micropaleontology* 107, 18–31.
- Dela Pierre, F., Bernardi, E., Cavagna, S., Clari, P., Gennari, R., Irace, A., Lozar, F., Lugli, S., Manzi, V., Natalicchio, M., Roveri, M., Violanti, D., 2011. The record of the Messinian salinity crisis in the Tertiary Piedmont Basin (NW Italy): The Alba section revisited. *Palaeogeography, Palaeoclimatology, Palaeoecology* 310, 238–255.
- Dela Pierre F., Clari P., Bernardi E., Natalicchio M., Costa E., Cavagna S., Lozar F., Lugli S., Manzi V., Roveri M. & Violanti D., 2012. Messinian carbonate-rich beds of the Tertiary Piedmont Basin (NW Italy): microbially-mediated products straddling the onset of the salinity crisis. *Palaeogeography, Palaeoclimatology, Palaeoecology*, 344-345: 78-93.
- Dela Pierre, F., Clari, P., Natalicchio, M., Ferrando, S., Giustetto, R., Lozar, F., Lugli, S., Manzi, V., Roveri, M., Violanti, D., 2014. Flocculent layers and bacterial mats in the mudstone interbeds of the primary lower Gypsum unit (Tertiary Piedmont basin, NW Italy): archives of palaeoenvironmental changes during the Messinian salinity crisis. *Mar. Geol.* 355, 71–87.
- Dela Pierre F., Natalicchio M., Ferrando S., Giustetto R., Birgel D., Carnevale G., Gier S., Lozar F., Marabello D. & Peckmann J., 2015. Are the large filamentous microfossils preserved in Messinian gypsum colorless sulfide-oxidizing bacteria? *Geology*, 43: 855-858.
- Diaz, R. J., and Rosenberg, R., 2008. Spreading dead zones and consequences for marine ecosystems. *Science* 321, 926–929
- DiStefano, A., Verducci, M., Lirer, F., Ferraro, L., Iaccarino, S.M., Husing, S.K., Hilgen F.J., 2010. Paleoenvironmental conditions preceding the Messinian Salinity Crisis in the Central Mediterranean: integrated data from the Upper Miocene Trave section (Italy) *Palaeogeogr. Palaeoclimatol. Palaeoecol.*, 297, 37-53.

- Douville, H., Chauvin, F., Planton, S., Royer, J. F., Salas-Melia, D., & Tyteca, S. (2002). Sensitivity of the hydrological cycle to increasing amounts of greenhouse gases and aerosols. *Climate Dynamics*, 20(1), 45-68.
- Dronkert, H., 1976. Late Miocene evaporites in the Sorbas Basin and adjoining areas, Mem. Soc. Geol. Italy, 341-361.
- Duggen, S., Hoernie, K., van den Bogaard, P., Rupke, L., PhippsMorgan, J., 2003. Deep roots of the Messinian salinity crisis. *Nature*, 422, 602-606.
- Elderfield, H., Ganssen, G., 2000. Past temperature and $\delta^{18}\text{O}$ of surface ocean waters inferred from foraminiferal Mg/Ca ratios. *Nature*, 405, 442-44.
- Engel, A., Zondervan, I., Aerts, K., Beaufort, L., Benthien, A., Chou, L., Delille, B., Gattuso, J.-P., Harlay, J., Heemann, C., Hoffmann, L., Jacquet, S., Nejtgaard, J., Pizay, M.D., Rochelle-Newall, E., Schneider, U., Terbruggen, A., Riebesell, U., 2005. Testing the direct effect of CO₂ concentration on a bloom of the coccolithophorid *Emiliania huxleyi* in mesocosm experiments. *Limnology and Oceanography* 50 (2), 493-507.
- Eppley, R.W., 1989. New production: history, methods, problems. In Berger, W.H., Smetacek, V.S., and Wefer, G. (Eds.), *Productivity of the Ocean: Present and Past*. Dahlem Workshop Rep., 85-97.
- Erba, E., Bottini, C., Weissert, H. J., Keller, C. E. 2010. Calcareous nannoplankton response to surface-water acidification around Oceanic Anoxic Event 1a. *Science* 329, 428-432.
- Erez, J., 2003. The source of ions for biomineralization in foraminifera and their implications for paleoceanographic proxies. *Rev. Mineralog. Geochem.*, 54, 115-149.
- Faucher, G., Erba, E., Bottini, C., & Gambacorta, G., 2017b. Calcareous nannoplankton response to the latest Cenomanian Oceanic Anoxic Event 2 perturbation. *Research in Paleontology and Stratigraphy*.
- Faucher, G., Hoffmann, L. J., Bach, L. T., Bottini, C., Erba, E., Riebesell, U., 2017a. Impact of trace metal concentrations on coccolithophore growth and morphology: laboratory simulations of Cretaceous stress. *Biogeosciences* 14, 3603- 3613.

- Faucher, G., Riebesell, U., Bach, L.T., 2020. Can morphological features of coccolithophores serve as a reliable proxy to reconstruct environmental conditions of the past? *Climate of the Past*, 16, 1007–1025.
- Ferreira, J., Mattioli, E., van de Schootbrugge, B., 2017. Palaeoenvironmental vs. evolutionary control on size variation of coccoliths across the Lower-Middle Jurassic. *Palaeogeography, Palaeoclimatology, Palaeoecology*, 465, 177–192.
- Flecker, R., Krijgsman, W., Capella, W., de Castro Martins, C., Dmitrieva, E., Mayser, J. P., Marzocchi, A., Modestou, S., Ochoa, D., Simon, D., Tulbure, M., van den Berg, B., van der Schee, M., de Lange, G., Ellam, R., Govers, R., Gutjahr, M., Hilgen, F., Kouwenhoven, T., Lofi, J., Meijer, P., Sierro, F. J., Bachiri, N., Barhoun, N., Alami, A. C., Chacon, B., Flores, J. A., Gregory, J., Howard, J., Lunt, D., Ochoa, M., Pancost, R., Vincent, S., Yousfi, M. Z., 2015. Evolution of the Late Miocene Mediterranean-Atlantic gateways and their impact on regional and global environmental change. *Earth-Science Reviews*, 150, 365-392.
- Flores, J.A., Sierro, F.J., Raffi, I., 1995. Evolution of the calcareous nannofossil assemblage as a response to the paleoceanographic changes in the eastern equatorial Pacific Ocean from 4 to 2 Ma (Leg 138, Sites 849 and 852). *Proc. Ocean Drill. Program Sci. Results*, 138, 163-176.
- Flores, J. A., Sierro, F. J., Filippelli, G. M., Barcena, M. A., Pérez-Folgado, M., Vazquez, A., Utrilla, R., 2005. Surface water dynamics and phytoplankton communities during deposition of cyclic late Messinian sapropel sequences in the western Mediterranean. *Marine Micropaleontology*, 56, 50-79.
- Fortuin, A.R., Krijgsman, W., Hilgen, F.J., Sierro, F.J., 2000. Late Miocene Mediterranean desiccation: topography and significance of the “Salinity Crisis” erosion surface onland in southeast Spain: comment. *Sedimentary Geology*, 133, 167-174.
- Fortuin, A.R., Krijgsman, W., 2003. The Messinian of the Nijar Basin (SE Spain): sedimentation, depositional environments and paleogeographic evolution. *Sedimentary Geology*, 160, 213–242.

- Fourtanier E., Gaudant J. & Cavallo O., 1991. La diatomite de Castagnito (Piémont): une nouvelle preuve de l'existence d'oscillations modérées du niveau marin pendant le Messinien évaporitique. *Bollettino della Società Paleontologica Italiana*, 30: 79-95.
- Garcia-Castellanos, D., Villaseñor, A., 2011. Messinian salinity crisis regulated by competing tectonics and erosion at the Gibraltar arc. *Nature*, 480 (7377), 359-363.
- Gelin F, Sinninghe Damsté J. S., Harrison W. N., Maxwell J. R. and de Leeuw J. W., 1995 Molecular indicators of palaeoenvironmental change in a Messinian evaporitic sequence (Vena del Gesso, Italy). III: Stratigraphic changes in the molecular structure of kerogen in a single marl bed as revealed by flash pyrolysis. *Org. Geochem.* 23, 555-566.
- Gennari R., Manzi V., Angeletti L., Bertini A., Biffi U., Ceregato A., Faranda C., Gliozzi E., Lugli S., Menichetti E., Rosso A., Roveri M. & Taviani M., 2013. A shallow water record of the onset of the Messinian salinity crisis in the Adriatic foredeep (Legnagnone section, Northern Apennines). *Palaeogeography, Palaeoclimatology, Palaeoecology*, 386: 145-164.
- Gennari, R., Lozar, F., Turco, E., Dela Pierre, F., Manzi, V., Natalicchio, M., Lugli, S., Roveri, M., Schreiber, B.C., Taviani, M., 2018. Integrated stratigraphy and paleoceanographic evolution of the pre-evaporitic phase of the Messinian salinity crisis in the Eastern Mediterranean as recorded in the Tokhni section (Cyprus island). *Newsl. Stratigr.*, 51, 33-55.
- Gennari, R., Lozar, F., Natalicchio M., Zanella, E., Carnevale, G., Dela Pierre, F., 2020. Chronology of the Messinian events in the northernmost part of the Mediterranean: the Govone section (Piedmont Basin, NW Italy). *Rivista Italiana di Paleontologia e Stratigrafia* 126, 517–60.
- Gibbs, S. J., Poulton, A. J., Bown, P. R., Daniels, C. J., Hopkins, J., Young, J. R., Jones, H. L., Thiemann, G. J., O'Dea, S. A., and Newsam, C. 2013. Species-specific growth response of coccolithophores to Palaeocene-Eocene environmental change, *Nat. Geosci.*, 6, 218–222, 2013.
- Gibbs, S. J., Bralower T. J., Bown, P. R., Zachos, J. C., Bybell, L. M. 2006. Shelf and open-ocean calcareous phytoplankton assemblages across the Paleocene-Eocene Thermal Maximum: implications for global productivity gradients. *Geology*, 34, 233–236.

- Gibbs, S., Shackleton, N., Young, J. R., 2004. Orbitally forced climate signals in mid-Pliocene nannofossil assemblages. *Marine Micropaleontology*, 51, 39-56.
- Giraudeau, J., 1992. Distribution of recent nannofossils beneath the Benguela system: southwest African continental margin. *Mar. Geol.* 108, 219-237.
- Giraudeau, J., 1992. Distribution of recent nannofossils beneath the Benguela system: southwest African continental margin. *Marine Geology*, 108, 219-237.
- Grelaud, M., Rost, B., Rickaby R. E. M., de Vargas, C., 2011. Sensitivity of coccolithophores to carbonate chemistry and ocean acidification. *Nature*, 476, 80-83.
- Grelaud, M., Marino, G., Ziveri, P., and Rohling, E. J., 2012. Abrupt shoaling of the nutricline in response to massive freshwater flooding at the onset of the last interglacial sapropel event. *Paleoceanography*, 27, 3.
- Griffin, D.L., 2002. Aridity and humidity: two aspects of the late Miocene climate of North Africa and the Mediterranean. *Palaeogeogr. Palaeoclimatol. Palaeoecol.*, 182, 65-91.
- Haidar, A. T., Thierstein, H. R. (2001) Coccolithophore dynamics off Bermuda (N. Atlantic). *Deep-Sea Res. II* , 48, 1925-1956.
- Hammer, Ø., Harper, D. A., & Ryan, P. D., 2001. PAST: Paleontological statistics software package for education and data analysis. *Palaeontologia electronica*, 4 (1), 9.
- Hanor, J. S., Chan, L. H., 1977. Non-conservative behaviour of barium during mixing of Mississippi River and Gulf of Mexico waters. *Earth Planet. Sci. Lett.*, 37, 242-250.
- Haq, B.U., Lohmann, G.P., 1976. Early Cenozoic calcareous nannoplankton biogeography of the Atlantic Ocean. *Mar. Micropaleontol.*, 1, 119-194.
- Hedges JI, Keil RG., 1995. Sedimentary organic-matter preservation: an assessment and speculative synthesis. *Mar. Chem.*, 49, 81-115.
- Hemleben, Ch., Spindler, M., Anderson, O.R., 1989. *Modern Planktonic Foraminifera*. Springer, New York, 363.

- Henderiks, J., Rickaby, R. E. M. 2007. A coccolithophore concept for constraining the Cenozoic carbon cycle. *Biogeosciences*, 4, 323–329.
- Henderiks, J., Pagani, M., 2008. Coccolithophore cell size and the Paleogene decline in atmospheric CO₂. *Earth and Planetary Science Letters*. 269, 576-584
- Herbert, T. D., 2003. Alkenone paleotemperature determinations. *Treatise on geochemistry*, 6, 625.
- Herbert, T.D., Lawrence, K.T., Tzanova, A., Peterson, L. C., Caballero-Gill, R., Kelly, C.S., 2016. Late Miocene global cooling and the rise of modern ecosystems. *Nature Geoscience*, 9, 843- 847.
- Herrmann, S., Thierstein, H.R., 2012. Cenozoic coccolith size changes — evolutionary and/or ecological controls? *Palaeogeography Palaeoclimatology Palaeoecology*, 333–334, 92–106.
- Herrmann, S., Weller, A.F., Henderiks, J., Thierstein, H.R., 2012. Global coccolith size variability in Holocene deep-sea sediments. *Marine Micropaleontology*, 82–83, 1–12.
- Hilgen, F. J., Krijgsman, W., 1999. Cyclostratigraphy and astrochronology of the Tripoli diatomite formation (pre-evaporite Messinian, Sicily, Italy), *Terra Nova*, 11, 16-22.
- Hsü, K.J., Montadert, L., Bernoulli, D., Cita, M.B., Erikson, A., Garrison, R.E., Kidd, R.B., Melieres, F., Muller, C., Wright, R.H., 1978. Initial report of Deep Sea Drilling Project. Mediterranean Sea, 42. U.S. Government Printing Office, Washington, DC.
- Iaccarino, S.M., Bossio, A., 1999. Paleoenvironment of uppermost Messinian sequences in the western Mediterranean (sites 974, 975 and 978). In: Zahn, R., Comas, M.C., Klaus, A. (Eds.), *Proceedings of the Ocean Drilling Program. Scientific Results*, 161. Ocean Drilling Program, College Station, TX, 529–540.
- Iaccarino, S.M., Bertini, A., Di Stefano, A., Ferraro, L., Gennari, R., Grossi, F., Lirer, F., Manzi, V., Menichetti, E., Ricci Lucchi, M., Taviani, M., Sturiale, G., Angeletti, L., 2008. The Trave section (Monte dei Corvi, Ancona, Central Italy): an integrated paleontological study of the Messinian deposits. *Stratigraphy*, 5, 281-306.

- Iglesias-Rodriguez, M. D., P. R. Halloran, R. E. M. Rickaby, I. R. Hall, E. Colmenero-Hidalgo, J. R. Gittins, D. R. H. Green, T. Tyrrell, S. J. Gibbs, P. von Dassow, E. Rehm, E. V. Armbrust, and K. P. Boessenkool. 2008. Phytoplankton calcification in a high-CO₂ world. *Science*, 320, 336–340.
- Imai, R., Sato, T., Iryu, Y., 2013. Chronological and paleoceanographic constraint of Miocene to Pliocene ‘mud sea’ in the Ryukyu Island (southwestern Japan) based on calcareous nannofossil assemblages. *Island Arc*, 22, 522–537.
- Imai, R., Farida, M., Sato, T., Iryu, Y., 2015. Evidence for ocean eutrophication in the northwestern Pacific and eastern Indian oceans during the Miocene to Pleistocene based on the nannofossil accumulation rate, *Discoaster* abundance, and coccolith size distribution of *Reticulofenestra*. *Mar. Micropaleontol.*, 116, 15-27.
- Imai, R., Sato, T., Iryu, Y., 2017. Calcareous nannofossil assemblages of the upper Miocene to Pliocene Shimajiri Group on Okinawa-jima, Ryukyu Islands, southwestern. *Japan Journal of Asian Earth Sciences*, 135, 16-24.
- Isaji, Y., Kawahata, H., Takano, Y., Ogawa, N. O., Kuroda, J., Yoshimura, T., Lugli, S., Manzi, V., Roveri, M., Ohkouchi, N., 2019. Diazotrophy drives primary production in the organic-rich shales deposited under a stratified environment during the Messinian salinity crisis (Vena Del Gesso, Italy). *Frontiers in Earth Science* 7, article 85
- Jahnke, R. A., Craven, D. B., McCorkle, D. C., & Reimers, C. E., 1997. CaCO₃ dissolution in California continental margin sediments: The influence of organic matter remineralization. *Geochimica et Cosmochimica Acta*, 61(17), 3587-3604.
- Jannink, N.T., Zachariasse, W.J. Van der Zwaan, G.J., 1998. Living (Rose Bengal stained) benthic foraminifera from the Pakistan continental margin. (northern Arabian Sea). *Deep-Sea Research I*, 45, 1483-1513.
- Kaiho, K., Takeda, K., Petrizzo, M. R., and Zachos, J. C., 2006. Anomalous shifts in tropical Pacific planktonic and benthic foraminiferal test size during the Paleocene–Eocene thermal maximum. *Palaeogeography, Palaeoclimatology, Palaeoecology*, 237 (2-4), 456-464.

- Kallel, N., Paterne, M., Labeyrie, L.D., Duplessy, J.C. and Arnold, M., 1997. Temperature and salinity records of the Tyrrhenian sea during the last 18000 years. *Palaeogeography, Palaeoclimatology, Palaeoecology*, 135, 97-108.
- Karakitsios, V., Roveri, M., Lugli, S., Manzi, V., Gennari, G., Antonarakou, A., Triantaphyllou, M., Agiadi, K., Kontakiotis, G., Kafousia, N., de Rafelis, M., 2017. A record of the Messinian salinity crisis in the eastern Ionian tectonically active domain (Greece, eastern Mediterranean). *Basin Research* 29, 203-233.
- Keil, R., 2017. Anthropogenic Forcing of Carbonate and Organic Carbon Preservation in Marine Sediments *Annu. Rev. Mar. Sci.*, 9, 151-72.
- Keller, G., Abramovich, S., 2009. Lilliput effect in late Maastrichtian planktic foraminifera: Response to environmental stress. *Palaeogeography Palaeoclimatology Palaeoecology*, 284, 47–62.
- Kemp, A.E.S., Pike, J., Pearce, R.B., Lange, C.B., 2000. The “Fall dump” – a new perspective on the role of a “shade flora” in the annual cycle of diatom production and export flux. *Deep-Sea Res. Pt. II*, 47, 2129-2154.
- Kemp, A.E.S., Villareal, T.A., 2013. High diatom production and export in stratified waters—A potential negative feedback to global warming. *Prog. Oceanogr.*, 119, 4-23.
- Kenig, F., Sinninghe, Damsté J. S., Frewin, N. L., Hayes, J. M. De Leeuw, J. W., 1995 Molecular indicators for palaeoenvironmental change in a Messinian evaporitic sequence (Vena del Gesso, Italy). II: high-resolution variations in abundances and ^{13}C contents of free and sulphur-bound carbon skeletons in a single marl bed. *Organic Geochemistry* 23, 485–526.
- Kouwenhoven, T.J., Seidenkrantz, M.S., van der Zwaan, G.J., 1999. Deep-water changes: the near synchronous disappearance of a group of benthic foraminifera from the Late Miocene Mediterranean. *Palaeogeogr. Palaeoclimatol. Palaeoecol.* 152, 259-281.
- Kouwenhoven, T. J., Hilgen, F. J. & van der Zwaan, G. J., 2003. Late Tortonian-early Messinian stepwise disruption of the Mediterranean-Atlantic connections: constraints from benthic foraminiferal and geochemical data. *Palaeogeography, Palaeoclimatology, Palaeoecology*, 198, 303-319.

- Kouwenhoven, T.J., Morigi, C., Negri, A., Giunta, S., Krijgsman, W., Rouchy, J.M., 2006. Palaeoenvironmental evolution of the eastern Mediterranean during the Messinian: constraints from integrated microfossil data of the Pissouri Basin (Cyprus). *Mar. Micropaleontol.* 60, 17-44.
- Krijgsman, W., F. J. Hilgen, I. Raffi, Sierro F. J., 1999), Chronology, causes and progression of the Messinian salinity crisis. *Nature*, 400, 652-655.
- Krijgsman, W., Fortuin, A. R., Hilgen, F. J., & Sierro, F. J., 2001. Astrochronology for the Messinian Sorbas basin (SE Spain) and orbital (precessional) forcing for evaporite cyclicity. *Sedimentary Geology*, 140(1-2), 43-60.
- Lacour, D., Nèraudeau, D., 2000. Évolution de la diversité des Brissopsis (Echinoida, Spatangoida) en Méditerranée depuis la « crise messinienne »: application paléocéologique aux *B. lyrifera* intragypses de Sorbas (SE Espagne). *Geodiversitas* 22 (4): 509-523.
- Landini W. & Sorbini L., 1989. Ichthyofauna of the evaporitic Messinian in the Romagna and Marche regions. *Bollettino della Società Paleontologica Italiana*, 28: 287-293.
- Langer, G., Geisen, M., Baumann, K. H., Kläs, J., Riebesell, U., Thoms, S., & Young, J. R., 2006. Species-specific responses of calcifying algae to changing seawater carbonate chemistry. *Geochemistry, geophysics, geosystems*, 7(9).
- Langer, G., Nehrke, G., Probert, I., Ly, J., & Ziveri, P., 2009. Strain-specific responses of *Emiliana huxleyi* to changing seawater carbonate chemistry. *Biogeosciences*, 6 (11), 2637-2646.
- Langer, G., Probert, I., Nehrke, G., and Ziveri, P. 2011. The morphological response of *Emiliana huxleyi* to seawater carbonate chemistry changes: an inter-strain comparison. *Journal of Nanoplankton Research*, 32 (1), 29-34.
- Larson, E. B., Mylroie, J. E., 2014. A review of whiting formation in the Bahamas and new models. *Carbonates and Evaporites*, 29(4), 337-347.
- Laskar, J., Robutel, P., Joutel, F., Gastineau, M., Correia, A.C.M., Levrard, B., 2004. A long-term numerical solution for the insolation quantities of the Earth. *Astron. Astrophys.* 428, 261-285.

- Le Quéré, C., Andrew, R. M., Friedlingstein, P., Sitch, S., Hauck, J., Pongratz, J., Pickers, P., Korsbakken, J.I., Peters, G.P., Canadell, J.G., others, 2016. Global carbon budget 2016. *Earth System Science Data*, 8, 605.
- Lea, D.W., Boyle, E.A., 1991. Barium in planktonic foraminifera. *Geochimica et Cosmochimica Acta*, 55, 3321-3331.
- Lea, D.W., Mashiotta, T.A., Spero, H.J., 1999. Controls on magnesium and strontium uptake in planktonic foraminifera determined by live culturing. *Geochim. Cosmochim. Acta*, 63, 2369-2379.
- Legendre, L., and Le Fevre, J., 1989. Hydrodynamical singularities as controls of recycled versus export production in oceans. In Berger, W.H., Smetacek, V.S., and Wefer, G. (Eds.), *Productivity of the Ocean: Present and Past*: Chichester (John Wiley), 49-63.
- Limburg, K. E., Breitburg, D., Swaney, D. P., & Jacinto, G. (2020). Ocean deoxygenation: a primer. *One Earth*, 2(1), 24-29.
- Lirer, F., Foresi, L.M., Iaccarino, S.M., Salvatorini, G., Turco, E., Cosentino, C., Sierro, F.J., Caruso, A., 2019. Mediterranean Neogene planktonic foraminifer biozonation and biochronology. *Earth-Science Reviews*, 196, 102869.
- Liu, X., Li, A., Dong, J., Zhuang, G., Xu, F., Wan, S., 2018. Nonevaporative origin for gypsum in mud sediments from the East China Sea shelf. *Marine Chemistry*, 205, 90-97.
- Lohmann, G.P., Carlson, J.J., 1981. Oceanographic significance of Pacific late Miocene calcareous nannoplankton. *Mar. Micropaleontol.*, 6, 553-579.
- Loreau, J.P., 1982, *Sédiments aragonitiques et leur dévise: Mémoires du Muséum National d'Histoire Naturelle, Série C., Tome XLVI1, 300 p.*
- Lozar, F., Violanti, D., Dela Pierre, F., Bernardi, E., Cavagna, S., Clari, P., Irace, A., Martinetto, E., Trenkwalder, S., 2010. Calcareous nannofossils and foraminifers herald the Messinian salinity crisis: the Pollenzo section (Alba, Cuneo; NW Italy). *Geobios*, 43, 21-32.

- Lozar, F., Violanti, D., Bernardi, E., Dela Pierre, F., Natalicchio, M., 2018. Identifying the onset of the Messinian salinity crisis: a reassessment of the biochronostratigraphic tools (Piedmont Basin, NW Italy) *Newsletters on Stratigraphy*, 51/1, 11-31.
- Lozar, F., Negri, A., 2019. A review of basin-wide calcareous nannofossil bioevents in the Mediterranean at the onset of the Messinian salinity crisis. *Marine Micropaleontology*, 151, 101752.
- Lübke, N., Mutterlose, J., Bottini, C. 2015. Size variations of coccoliths in Cretaceous oceans, a result of preservation, genetics and ecology? *Marine Micropaleontology*, 117, 25-39.
- Lübke, N. and Mutterlose, J. 2016. The impact of OAE 1a on marine biota deciphered by size variations of coccoliths. *Cretaceous Research*, 61, 169-179.
- Lugli, S., Manzi, V., Roveri, M., Schreiber, B. C., 2010. The Primary Lower Gypsum in the Mediterranean: a new facies interpretation for the first stage of the Messinian salinity crisis. *Palaeogeography, Palaeoclimatology, Palaeoecology*, 297, 83–99.
- Macintyre I. G., Reid R.P., 1992. Comment on the origin of aragonite needle mud: a picture is worth a thousand words. *J Sediment Petrol* 62:1095–1097
- Macintyre, I. G., & Reid, R. P., 1995. Crystal alteration in a living calcareous alga (*Halimeda*); implications for studies in skeletal diagenesis. *Journal of Sedimentary Research*, 65(1a), 143-153.
- Malinverno, E., Ziveri, P., Corselli, C., 2003. Coccolithophorid distribution in the Ionian Sea and its relationship to eastern Mediterranean circulation during late fall to early winter 1997 *journal of geophysical research*, 108, 8115.
- Mancini, A. M., Gennari, R., Ziveri, P., Mortyn, P. G., Stolwijk, D. J. Lozar, F., 2020. Calcareous nannofossil and foraminiferal trace element records in the Sorbas Basin: A new piece of the Messinian Salinity Crisis onset puzzle. *Palaeogeography, Palaeoclimatology, Palaeoecology*, 554, 109796.
- Manzi, V., Roveri, M., Gennari, R., Bertini, A., Biffi, U., Giunta, S., Iaccarino, S.M., Lanci, L., Lugli, S., Negri, A., Riva, A., Rossi, M.E., Taviani, M., 2007. The deep-water counterpart of the Messinian Lower Evaporites in the Apennine foredeep: the Fananello section (Northern Apennines, Italy). *Palaeogeogr. Palaeoclimatol. Palaeoecol.* 251, 470-499.

- Manzi, V., Gennari, R., Hilgen, F., Krijgsman, W., Lugli, S., Roveri, M., Sierro, F.J., 2013. Age refinement of the Messinian salinity crisis onset in the Mediterranean. *Terra Nova*, 25, 315-322.
- Manzi, V., Gennari, R., Lugli, S., Minelli, N., Reghizzi, M., Roveri, M., & Schreiber, B. C., 2016. Comment on “Carbonate deposition and diagenesis in evaporitic environments: The evaporative and sulphur-bearing limestones during the settlement of the Messinian Salinity Crisis in Sicily and Calabria” by Caruso et al., 2015. *Palaeo3*, 429, 136–162. *Palaeogeography, Palaeoclimatology, Palaeoecology*, 459, 585-596.
- Manzi, V., Gennari, R., Lugli, S., Persico, D., Reghizzi, M., Roveri, M., Schreiber, B. C., Calvo, R., Gavrieli, I., Gvirtzman, Z., 2018. The onset of the Messinian salinity crisis in the deep Eastern Mediterranean basin. *Terra Nova*, 30 (3), 189-198.
- Margalef, R., 1978. Life-forms of phytoplankton as survival alternatives in an unstable environment. *Oceanologica Acta*, 1, 493-509.
- Martín, J. M., and Braga, J.C., 1994. Messinian events in the Sorbas Basin in southeastern Spain and their implications in the recent history of the Mediterranean. *Sediment. Geol.*, 90, 257-268.
- Martín, J.M., and Meybeck, M., 1979, Elemental mass-balance of material carried by major world rivers, *Mar. Chem.*, 7, 173-206.
- Mattioli, E., Pittet, B., Petitpierre, L., Mailliot, S., 2009. Dramatic decrease of pelagic carbonate production by nannoplankton across the Early Toarcian anoxic event (T-OAE). *Global Planetary Change*, 65, 134–145.
- Mazumder, A., Nigam, R., 2014. Bathymetric preference of four major genera of rectilinear benthic foraminifera within oxygen minimum zone in Arabian Sea off central west coast of India. *Journal of Earth System Science*, 123(3), 633-639.
- McKenzie, J.A., Jenkyns, H.C., Bennet, G.G., 1979. Stable isotope study of the cyclic diatomite-claystones from the Tripoli formation, Sicily: a prelude to the Messinian salinity crisis. *Palaeogeogr. Palaeoclimatol. Palaeoecol.* 29, 125-141

- McNeil, D. H., 1997. Diagenetic regimes and the foraminiferal record in the Beaufort-Mackenzie Basin and adjacent cratonic areas. In *Annales Societatis Geologorum Poloniae* (Vol. 67, No. 2-3, pp. 271-286).
- Meier, K.J.S., Beaufort, L., Heussner, S., Ziveri, P. 2014. The role of ocean acidification in *Emiliana huxleyi* coccolith thinning in the Mediterranean Sea. *Biogeosciences*, 11, 2857-2869
- Meilijson, Aaron, Hilgen, Frits, Sepulveda, Julio, Steinberg, Josh, Fairbank, Vanessa, Flecker, Rachel, Waldmann, Nicolas D., et al., 2019. Chronology with a pinch of salt: integrated stratigraphy of Messinian evaporites in the deep Eastern Mediterranean reveals long-lasting halite deposition during Atlantic connectivity. *Earth-Sci. Rev.* 194, 374–398.
- Mejía-Molina, A., Flores, J.-A., Torres, V., Sierro, F.J., 2010. Distribution of calcareous nannofossils in Upper Eocene-Upper Miocene deposits from Northern Colombia and the Caribbean sea *Revista Española de Micropaleontología*, 42, 279-300.
- Meyer, J. and Riebesell, U., 2015. Responses of coccolithophores to ocean acidification: a meta-analysis. *Biogeosciences*, 12, 1671–1682.
- Milliman, J.D., Freile, D., Steinen, R.P. and Wilber, R.J., 1993. Great Bahama Bank aragonitic muds: mostly inorganically precipitated, mostly exported. *J. Sed. Petrol.* 63, 589–595
- Milner S., Langer G., Grelaud M., Ziveri P. 2016. Ocean warming modulates the effects of acidification on *Emiliana huxleyi* calcification and sinking. *Limnology Oceanography*, 61, 1322–1336.
- Modestou, S., Simon, D., Gutjahr, M., Marzocchi, A., Kowenhoven, T.J., Ellam, R.M., Flecker, R., 2017. Precessional variability of $^{87}\text{Sr}/^{86}\text{Sr}$ in the late Miocene Sorbas Basin: an interdisciplinary study of drivers of interbasin exchange. *Paleoceanography* 32, 1–22.
- Moissette, P., Saint Martin, J.P., 1992. Upwelling and benthic communities in the Messinian of western Mediterranean. *Paleont. Evol.*, 24-25, 245-254
- Montenat, C., Ott d'Estevou, P., Plaziat, J. C., & Chapel, J., 1980. La signification des faunes marines contemporaines des évaporites messiniennes dans le Sud-Est de l'Espagne. Conséquences pour l'interprétation des conditions d'isolement de la Méditerranée occidentale. *Géologie méditerranéenne*, 7(1), 81-89.

- Murray J.W., 2006. Ecology and Applications of Benthic Foraminifera. Cambridge University Press, 426
- Natalicchio, M., Dela Pierre, F., Lugli S., Lowenstein, T. K., Feiner, S.J., Ferrando, S., Manzi, V., Roveri M., Clari, P., 2014 Did Late Miocene (Messinian) gypsum precipitate from evaporated marine brines? Insights from the Piedmont Basin (Italy). *Geology* 42, 179–82.
- Natalicchio, M., Dela, Pierre F., Birgel, D., Brumsack, H., Carnevale, G., Gennari, R., Gier, S., Lozar, F., Pellegrino, L., Sabino, M., Schnetger, B., Peckmann, J., 2019. Paleoenvironmental change in a precession-paced succession across the onset of the Messinian salinity crisis: Insight from element geochemistry and molecular fossils. *Palaeogeogr. Palaeoclimatol. Palaeoecol.* 518, 45–61.
- Negri, A., Capodonti, L., Keller, J., 1999a. Calcareous nannofossils, planktic foraminifers and oxygen isotope in the late Quaternary sapropels of the Ionian Sea. *Mar. Geol.*, 151, 84–89.
- Negri, A., Giunta, S., Hilgen, F.J., Krijgsman, W., Vai, G.B., 1999b. Calcareous nannofossil biostratigraphy of the M. del Casino section (northern Apennines, Italy) and paleoceanographic conditions at times of late Miocene sapropel formation. *Mar. Micropaleontol.*, 36, 13–30.
- Néraudeau D., Videt B., Courville P., Goubert E. & Rouchy J.-M., 2002. Corrélation des niveaux fossilifères marins interstratifiés dans les gypses messiniens, entre la carrière de Molinos de Aguas (bassin de Sorbas, SE Espagne). *Geodiversitas*, 24: 659–667.
- Neuer, S., Davenport, R., Freudenthal, T., Wefer, G., Llinàs, O., Rueda, M.-J., Steinberg, D.K., Karl, D.M., 2002. Differences in the biological carbon pump at three subtropical ocean sites. *Geophysical Research Letters*, 29, 1985.
- Obst, M., Dynes, J., Lawrence, J., Swerhone, G., Benzerara, K., Karunakaran, C., Kaznatcheev K., Tyliszczak, T., Hitchcock A.P., 2009. Precipitation of amorphous CaCO₃ (aragonite-like) by cyanobacteria: a STXM study of the influence of EPS on the nucleation process. *Geochim. Cosmochim. Acta* 73, 4180–4198.
- Okada, H., McIntyre, A., 1979. Seasonal distribution of modern coccolithophorids in the Western North Atlantic Ocean. *Marine Biology*, 54, 319–328.

- Oliveri, E., Neri, R., Bellanca, A., Riding, R., 2010. Carbonate stromatolites from a Messinian hypersaline setting in the Caltanissetta Basin, Sicily: petrographic evidence of microbial activity and related stable isotope and rare earth element signatures. *Sedimentology* 57, 142e161.
- Orszag-Sperber, F., Caruso, A., Blanc-Valleron, M.M., Merle, D., Rouchy, J.M., 2009. The onset of the Messinian salinity crisis: insights from Cyprus sections *Sediment. Geol.*, 217, 52-64.
- Oviedo, A., Ziveri, P., Alvarez, M., Tanhua, T., 2015. Is coccolithophore distribution in the Mediterranean sea related to seawater carbonate chemistry? *Ocean Science*, 11, 13-32
- Paasche, E., 2002. A review of the coccolithophorid *Emiliania huxleyi* (Prymnesiophyceae), with particular reference to growth, coccolith formation, and calcification-photosynthesis interactions. *Phycologia*, 40(6), 503–529.
- Pellegrino L., Dela Pierre F., Natalicchio M. & Carnevale G., 2018. The Messinian diatomite deposition in the Mediterranean and its relationships to the global silica cycle. *Earth-Science Reviews*, 178, 154-176.
- Perch-Nielsen, K., 1985. Cenozoic calcareous nanofossils. In: Bolli, H. M., Saunders, J. B., Perch-Nielsen, K. (Eds.), *Plankton Stratigraphy*. Cambridge University Press, Cambridge, 427-554.
- Pérez-Folgado, M., Sierro, F.J., Bàrcena, M.A., Flores, J.A., Vázquez, A., Utrilla, R., Hilgen, F.J., Krijgsman, W., Filippelli, G.M., 2003. Western versus eastern Mediterranean paleoceanographic response to astronomical forcing: a high-resolution microplankton study of precession-controlled sedimentary cycles during the Messinian. *Palaeogeogr. Palaeoclimatol. Palaeoecol.*, 190, 317-334.
- Perri, E., Gindre-Chanu, L., Caruso, A., Cefalà, M., Scopelliti, G. & Tucker, M., 2017. Microbial-mediated pre-salt carbonate deposition during the Messinian salinity crisis (Calcare di Base fm., Southern Italy). *Marine and Petroleum Geology*, 88: 235-250.
- Peterson, L. C., & Prell, W. L., 1985. Carbonate dissolution in recent sediments of the eastern equatorial Indian Ocean: preservation patterns and carbonate loss above the lysocline. *Marine Geology*, 64(3-4), 259-290.
- Pierre, C., 1999. The oxygen and carbon isotope distribution in the Mediterranean water masses. *Marine geology*, 153(1-4), 41-55.

- Pierre, C., & Rouchy, J. M., 2004. Isotopic compositions of diagenetic dolomites in the Tortonian marls of the western Mediterranean margins: evidence of past gas hydrate formation and dissociation. *Chemical Geology*, 205(3-4), 469-484.
- Poot-Delgado, C. A., Okolodkov, Y. B., Aké-Castillo, J. A., Rendón-von Osten, J., 2015. Annual cycle of phytoplankton with emphasis on potentially harmful species in oyster beds of Términos Lagoon, southeastern Gulf of Mexico. *Revista de Biología Marina y Oceanografía*. 50, 465-477.
- Quinn, P., Saez, A.G., Baumann, K.-H., Steel, B.A., Sprengel, C., and Medlin, L.K., 2004. Coccolithophorid biodiversity: Evidence from the cosmopolitan species *Calcidiscus leptoporus*. In: H.R. Thierstein and J.R. Young, Eds., *Coccolithophores - From molecular processes to global impact*. Springer, 299-326.
- Ragueneau, O., Tréguer, P., Leynaert, A., Anderson, R.F., Brzezinski, M.A., DeMaster, D.J., Dugdale, R.C., Dymond, J., François, R., Heinze, C., Maier-Reimer, E., Martin-Jézéquel, V., Nelson, D.M., Quéguiner, B., 2000. A review of the Si cycle in the modern ocean: recent progress and missing gaps in the application of biogenic opal as a paleoproductivity proxy. *Glob. Planet. Change*, 26 (4), 317-365.
- Reghizzi, M., Gennari, R., Douville, E., Lugli, S., Manzi, V., Montagna, P., Roveri, M., Sierro, F.J., Taviani, M., 2017. Isotope stratigraphy ($^{87}\text{Sr}/^{86}\text{Sr}$, $\delta^{18}\text{O}$, $\delta^{13}\text{C}$) of the Sorbas basin (Betic Cordillera, Spain): Paleooceanographic evolution across the onset of the Messinian salinity crisis. *Palaeogeogr. Palaeoclimatol. Palaeoecol.* 469, 60-73.
- Reghizzi, M., Lugli, S., Manzi, V., Rossi, F. P., Roveri, M., 2018. Orbitally forced hydrological balance during the messinian salinity crisis: insights from strontium isotopes ($^{87}\text{Sr}/^{86}\text{Sr}$) in the Vena del Gesso Basin (Northern Apennines, Italy). *Paleoceanography and Paleoclimatology*, 33(7), 716-731.
- Riding, R., Braga, J.C., Martin, J.M., Sanchez-Almazo, I.M., 1998. Mediterranean Messinian salinity crisis: constraints from a coeval marginal basin, Sorbas, southeastern Spain. *Mar. Geol.* 146, 1-20.
- Riebesell, U., Zondervan I., Rost, B., Tortell, P.D., Zeebe, R.E., Morel, F.M.M., 2000 Reduced calcification of marine plankton in response to increased atmospheric CO₂. *Nature*, 407, 2-5.

- Riebesell, U., Bach, L. T., Richard G. J., Bellerby, R. G. J., Bermúdez Monsalve, R. J., Boxhammer, T., Czerny, J., Larsen, A., Ludwig, A., Schulz, K. G., 2016. Competitive fitness of a predominant pelagic calcifier impaired by ocean acidification. *Nature geoscience*. 1 (1), 19-23.
- Robbins, L.L. and Blackwelder, P.L. 1992 Biochemical and ultrastructural evidence for the origin of whittings: a biologically induced calcium carbonate precipitation mechanism. *Geology* 20, 464–468.
- Robbins, L.L., Tao, Y. and Evans, C.A. 1997 Temporal and spatial distribution of whittings on Great Bahama Bank and a new lime mud budget. *Geology* 25, 947–950.
- Rodríguez-Tovar, F.J., Sánchez-Almazo, I., Pardo-Igúzquiza, E., Braga, J.C., Martín, J.M., 2013. Incidence of obliquity and precessionforced Milankovitch cycles in the western Mediterranean: early Messinian sedimentation in the Sorbas Basin (Almería, southern Spain). *Int. J. Earth Sci.*, 102, 1735-1755.
- Roep, T. B., Dabrio, C. J., Fortuin, A. R., & Polo, M. D. 1998. Late highstand patterns of shifting and stepping coastal barriers and washover - fans (late Messinian, Sorbas Basin, SE Spain). *Sedimentary Geology*, 116, 27–56.
- Rohling, E.J., Gieskes, W.W.C., 1989. Late Quaternary changes in Mediterranean Intermediate Water density and formation rate. *Paleoceanography*, 4, 531-545.
- Rohling, E.J., 1994. Review and new aspects concerning the formation of Mediterranean sapropels. *Mar. Geol.*, 122, 1-28.
- Rohling, E. J., G. Marino, and K. M. Grant (2015), Mediterranean climate and oceanography, and the periodic development of anoxic events (sapropels), *Earth-Sci. Rev.*, 143, 62-97.
- Rosenthal, Y., et al. (2004), Interlaboratory comparison study of Mg/Ca and Sr/Ca measurements in planktonic foraminifera for paleoceanographic research, *Geochem. Geophys. Geosyst.*, 5, Q04D09.
- Rost B, Riebesell U. 2004 Coccolithophores and the biological pump: responses to environmental changes. In *Coccolithophores: from molecular processes to global impact* (eds HR Thierstein, JR Young), pp. 99–125. Berlin, Germany: Springer.

- Roth, P. H., Berger, W. H., 1975, Distribution and dissolution of coccoliths in the South and central Pacific, *Foraminiferal Res., Spec. Publ.*, 13, 87–113.
- Roth, P. H., Coulbourn, W. T., 1982. Floral and solution patterns of coccoliths in surface sediments of the North Pacific, *Mar. Micropaleontol.*, 7, 1– 52.
- Rouchy, J. M., & Caruso, A., 2006. The Messinian salinity crisis in the Mediterranean basin: a reassessment of the data and an integrated scenario. *Sedimentary Geology*, 188, 35-67.
- Roveri, M., Gennari, R., Lugli, S., Manzi, V., 2009. The Terminal Carbonate Complex: the record of sea-level changes during the Messinian salinity crisis. *GeoActa* 8, 57-71.
- Roveri, M., Flecker, R., Krijgsman, W., Lofi, J., Lugli, S., Manzi, V., Sierro, F.J., Bertini, A., Camerlenghi, A., De Lange, G., Govers, R., Hilgen, F.J., Hubscher, C., Meijer, P.T., Stoica, M., 2014. The Messinian Salinity Crisis: past and future of a great challenge for marine sciences. *Mar. Geol.* 352, 25-58.
- Roveri, M., Gennari, R., Persico, D., Rossi, F.P., Lugli, S., Manzi, V., Reghizzi, M., Taviani, M., 2018. A new chronostratigraphic and palaeoenvironmental framework for the end of the Messinian salinity crisis in the Sorbas Basin (Betic Cordillera, southern Spain). *Geol. J.* 54, 1617–1637
- Roveri, M., Lugli, S., Manzi, V., Reghizzi, M., Rossi, F. P. 2020. Stratigraphic relationships between shallow-water carbonates and primary gypsum: insights from the Messinian succession of the Sorbas Basin (Betic Cordillera, Southern Spain). *Sedimentary Geology*, 404, 105678.
- Ruegg, G.J.H., 1964. Geologische onderzoeken in het bekken van Sorbas. SE Spanje. Internal Report Geol. Inst. Univ. Amsterdam, 67 pp.
- Ryan, W. B. F., 2009. Decoding the Mediterranean salinity crisis. *Sedimentology*, 56, 95–136.
- Sabino, M., Pierre, F. D., Natalicchio, M., Birgel, D., Gier, S., & Peckmann, J., 2020. The response of water column and sedimentary environments to the advent of the Messinian salinity crisis: insights from an onshore deep-water section (Govone, NW Italy). *Geological Magazine*, 1-17.

- Sabino, M., Schefuß, E., Natalicchio, M., Dela Pierre, F., Birgel, D., Bortels, D., Schnetger, B., Peckmann, J., 2020. Climatic and hydrologic variability in the northern Mediterranean across the onset of the Messinian salinity crisis. *Palaeogeography, Palaeoclimatology, Palaeoecology* 545, article 109632
- Sabino, M., Pierre, F. D., Natalicchio, M., Birgel, D., Gier, S., & Peckmann, J., 2020. The response of water column and sedimentary environments to the advent of the Messinian salinity crisis: insights from an onshore deep-water section (Govone, NW Italy). *Geological Magazine*, 1-17.
- Saint-Martin J.-P., Néraudeau D., Lauriat-Rage A., Goubert E., Secrétan S., Babinot J.-F., Boukli-Hacene S., Pouyet S., Lacour D., Pestrea S. & Conesa G. 2000. La faune interstratifiée dans les gypses messiniens de Los Yesos (Bassin de Sorbas, SE Espagne): implications. *Geobios* 33 (5).
- Sakalli, A. 2017. Sea surface temperature change in the Mediterranean Sea under climate change: a linear model for simulation of the sea surface temperature up to 2100
- Sakka, A., Legendre, L., Gosselin, M., LeBlanc, B., Delesalle, B., & Price, N. M., 1999. Nitrate, phosphate, and iron limitation of the phytoplankton assemblage in the lagoon of Takapoto Atoll (Tuamotu Archipelago, French Polynesia). *Aquatic Microbial Ecology*, 19(2), 149-161.
- Salaviale, C., Gollain, B., Mattioli E., 2018. Calcareous nannofossil fluxes and size fluctuations in the middle Eocene (48-39 Ma) from Ocean Drilling Program (ODP) Site 1209 in the tropical Pacific Ocean. *Palaeogeography, Palaeoclimatology, Palaeoecology* ,490, 240-251.
- Salter, I., Schiebel, R., Ziveri, P., Movellan, A., Lampitt, R., and Wolff, G. A., 2014. Carbonate counter pump stimulated by natural iron fertilization in the Polar Frontal Zone. *Nature Geoscience*, 7(12), 885-889.
- Sanchez-Almazo, I.M., Braga, J.C., Dinares-Turell, J., 2007. Palaeoceanographic controls on reef deposition: the Messinian Cariatiz reef (Sorbas Basin, Almeria, SE Spain). *Sedimentology*, 54, 637-660.
- Schimmelmann, A., Lange, C.B, Schieber, J., Francus, P., Ojala, A.E.K., Zolitschk, B., 2016. Varves in marine sediments: A review. *Earth-Science Reviews*, 159, 215-246.
- Seidenkrantz, M.-S., Kouwehoven, T.J., Jorissen, F.J., Shackleton N.J., van der Zwaan G.J., 2000. Benthic foraminifera as indicators of changing Mediterranean-Atlantic water exchange in the late Miocene. *Mar. Geol.*, 163, 387-407.

- Sheward RM, Poulton AJ, Gibbs SJ, Daniels CJ, Bown PR. 2017 Physiology regulates the relationship between coccosphere geometry and growth phase in coccolithophores. *Biogeosciences*, 14, 1493–1509.
- Shinn, E.A., Steinen, R.P., Lidz, B.H. Swart, P.K., 1989 Whitings, a sedimentologic dilemma. *J. Sed. Petrol.* 59, 147– 161.
- Sierro, F.J., Hilgen, F.J., Krijgsman, W., Flores, J.A., 2001. The Abad composite (SE Spain): a Mediterranean and global reference section for the Messinian. *Palaeogeogr. Palaeoclimatol. Palaeoecol.*, 168, 141–169.
- Sierro, F.J., Flores, J.A., Barcena, M.A., Vazquez, A., Utrilla, R., Zamarreno, I., 2003. Orbitally-controlled oscillations in the planktic communities and cyclical changes in western Mediterranean hydrography during the Messinian. *Palaeogeography Palaeoclimatology Palaeoecology*, 190, 289–316.
- Silva, A., Palma, S., Moita, M.T., 2008. Coccolithophores in the upwelling waters of Portugal: Four years of weekly distribution in Lisbon bay. *Continental Shelf Research*, 28, 2601-2613.
- Somot, S., Sevault, F., Déqué, M., 2006. Transient climate change scenario simulation of the Mediterranean Sea for the twenty-first century using a high-resolution ocean circulation model. *Clim. Dyn.* 27, 851–879.
- Sondi, I., Juračić, M., 2010. Whiting events and the formation of aragonite in Mediterranean Karstic Marine Lakes: new evidence on its biologically induced inorganic origin. *Sedimentology*, 57(1), 85-95.
- Sprovieri, M.B.R.A., Manta, D.S., Bellanca, N., R., Lirer, F., Taberner, C., Pueyo, J.J., Sammartino, S., 2008. Ba/Ca evolution in water masses of the Mediterranean late Neogene paleoceanography, 23, 3205.
- Sprovieri, R., Di Stefano, E., Sprovieri, M., 1996. High resolution chronology for Late Miocene Mediterranean stratigraphic events. *Riv. Ital. Paleontol. Stratigr.* 102, 77–104.
- Steinsund, P. I., Hald, M., 1994. Recent calcium carbonate dissolution in the Barents Sea: Paleoceanographic applications. *Marine Geology*, 117(1-4), 303-316.
- Stoll H. M., Guitian J., Hernandez-Almeida I., Mejia L. M., Phelps S., Polissar P., Rosenthal Y., Zhang H. and Ziveri P., 2019. Upregulation of phytoplankton carbon concentrating mechanisms during low CO₂

- glacial periods and implications for the phytoplankton pCO₂ proxy. *Quaternary Science Review*, 208, 1-20.
- Subhas, A. V., Rollins, N. E., Berelson, W. M., Erez, J., Ziveri, P., Langer, G., Adkins, J. F., 2018. The dissolution behavior of biogenic calcites in seawater and a possible role for magnesium and organic carbon. *Marine Chemistry*, 205, 100-112.
- Suchéras-Marx, B., Mattioli, E., Pittet, B., Escarguel, G., Suan, G., 2010. Astronomically-paced coccolith size variations during the early Pliensbachian (Early Jurassic), *Palaeogeography, Palaeoclimatology, Palaeoecology*, 295, 281-292.
- Šupraha, L., Gerecht, A. C., Probert, I., & Henderiks, J. (2015). Eco-physiological adaptation shapes the response of calcifying algae to nutrient limitation. *Scientific reports*, 5 (1), 1-8.
- Swart, P.K. Eberli, G.P., 2005. The nature of the d13C of periplatform sediments: implications for stratigraphy and the global carbon cycle. *Sed. Geol.*, 175, 115–130.
- Swart, P.K., Oehlert, A.M., Mackenzie, G.J., Eberli, G.P., Reijmer, J.J.G., 2014. The Fertilization of the Bahamas by Saharan Dust: a trigger for carbonate precipitation? *Geology*, 42, 671–674.
- Swart, P.K., Reijmer, J.J. and Otto, R., 2009. A re-evaluation of facies on Great Bahama Bank II: variations in the d13C, d18O and mineralogy of surface sediments. In: *Perspectives in Carbonate Geology: A Tribute to the Career of Robert Nathan Ginsburg*, IAS Special Publication (Eds P.K. Swart,
- Tagliavento M., Lauridsen, B. W., Stemmerik, L., 2020. Episodic dysoxia during Late Cretaceous cyclic chalk-marl deposition – Evidence from framboidal pyrite distribution in the upper Maastrichtian Rørdal Mb., Danish Basin. *Cretaceous Research* 106, article 104223
- Takahashi, K., Okada, H., 2000. The paleoceanography for the last 30,000 years in the southeastern Indian Ocean by means of calcareous nannofossils *Marine Micropaleontology*, 40, 83-103.
- tectonics and erosion at the Gibraltar arc. *Nature*, 480 (7377), 359-363.
- Thompson J. B., 2000. Microbial whittings. In: Riding RE, Awramik SM (eds) *Microbial sediments*. Springer, Berlin, pp 250–260
- Tréguer, P., De La Rocha, 2013. The World Ocean Silica Cycle. *Ann. Rev. Mar. Sci.*, 5, 477-501.

- Tremolada, F., De Bernardi, B., Erba, E. 2008. Size variations of the calcareous nannofossil taxon *Discoaster multiradiatus* (Incertae sedis) across the Paleocene–Eocene thermal maximum in ocean drilling program holes 690B and 1209B. *Marine Micropaleontology*, 67, 239-254.
- Trenkwalder S., Violanti D., d’Atri A., Lozar F., Dela Pierre F., Irace A., (2008). The Miocene/Pliocene boundary and the Early Pliocene micropaleontological record: new data from the Tertiary Piedmont Basin (Moncucco quarry, Turin Hill, Northwestern Italy). *Bollettino della Società Paleontologica Italiana*, 47 (2): 87-103.
- Triantaphyllou, M.V., Ziveri, P., Gogou, A., Marino, G., Lykousis, V., Bouloubassi, I., Emeis, K.C., Kouli, K., Dimiza, M., Rosell-Mele, A., Papanikolaou, M., Katsouras, & G., Nunez, N., 2009. Late Glacial-Holocene climate variability at the south-eastern margin of the Aegean Sea. *Marine Geology*, 266, 182-197.
- Triantaphyllou, M.V., Dimiza et al., 2010. Seasonal control on *Emiliana huxleyi* coccolith morphology and calcification in the Aegean Sea (Eastern Mediterranean). *Geobios* 43: 99-110.
- Triantaphyllou, M. V., Baumann, K. H., Karatsolis, B. T., Dimiza, M. D., Psarra, S., Skampa, E., Patoucheas, P., Vollmar, N.M., Koukousioura O., Katsigera, A., Krasakopoulou, E., Nomikou, P., 2018. Coccolithophore community response along a natural CO₂ gradient off Methana (SW Saronikos Gulf, Greece, NE Mediterranean). *PLoS One*, 13, 1-21,
- Troelstra, S.R., Van der Poel, H.M., Huisman, C.H.A., Geerlings, L.P.A., Dronkert, H., 1980. Paleocological changes in the latest Miocene of the Sorbas Basin, S.E. Spain. *Geol. Mediterr.*, 8, 115-126.
- Tzanova, A., Herbert, T. D., & Peterson, L. (2015). Cooling Mediterranean Sea surface temperatures during the Late Miocene provide a climate context for evolutionary transitions in Africa and Eurasia. *Earth and Planetary Science Letters*, 419, 71-80.
- Urbanek, A., 1993. Biotic crises in the history of Upper Silurian graptoloids: a palaeobiological model. *Historical Biology*, 7, 29–50.
- van de Poel, H.M., 1992. Foraminiferal biostratigraphy of the Carboneras-Nijar Basin. *Scripta Geologica*, 102, 1-32.

- Van der Laan, E., Gaboardi, S., Hilgen, F.J., Lourens, L.J., 2005. Regional climate and glacial control on high-resolution oxygen isotope records from Ain El Beida (latest Miocene, NW Morocco): a cyclostratigraphic analysis in the depth and time domain. *Paleoceanography*, 20, PA1001.
- Van der Zwaan, G.J., Duijnste, I.A.P., den Dalk, M., Ernst, S.R., Jannink, N.T., Kouwenhoven, T.J., 1999. Benthic foraminifers: proxies or problems? A review of paleoecological concepts. *Earth Sci. Rev.*, 46, 213-236.
- Viaroli, P., Nizzoli, D., Pinardi, M., Soana, E., & Bartoli, M. (2015). Eutrophication of the Mediterranean Sea: a watershed—cascading aquatic filter approach. *Rendiconti Lincei*, 26(1), 13-23
- Violanti, D., Lozar, F., Dela Pierre, F., Natalicchio, M., Bernardi, E., Clari, P., Cavagna, S., 2013. Stress tolerant microfossils of a Messinian succession from the northern Mediterranean basin (Pollenzo section, Piedmont, Northwestern Italy). *Bollettino della Società Paleontologica Italiana*. 52 (1), 45–54.
- Voèlk, H.R., Rondeel, H.E., 1964. Zur gliederung des Jungtertiärs in becken von Vera, Südost Spanien. *Geol.Mijnbouw* 43, 310±315.
- Wade, B. S., Bown, P. R., 2006. Calcareous nannofossils in extreme environment: the Messinian Salinity Crisis, Polemi Basin, Cyprus. *Palaeogeography, Palaeoclimatology, Palaeoecology*, 233, 271-286.
- Wade, B.S., Twitchett, R.J., 2009. Extinction, dwarfing and the Lilliput effect. *Palaeogeography, Palaeoclimatology, Palaeoecology*, 284, 1-3
- Watabe N. and Wilbur K.M., 1966. Effects of temperature on growth, calcification, and coccolith form in *Coccolithus huxleyi* (Coccolithineae). *Limnology and Oceanography*. 11, 567-575.
- Wilkin, R. T., Arthur, M. A., & Dean, W. E., 1997. History of water-column anoxia in the Black Sea indicated by pyrite framboid size distributions. *Earth and Planetary Science Letters*, 148(3-4), 517-525.
- Yáñez-Arancibia A and JW Day. 2005. Ecosystem functioning: the basis for sustainable management of Terminos Lagoon, Campeche, México, 77 pp. Institute of Ecology A.C., Jalapa.
- Yates K. K., Robbins, L. L., 1998. Production of carbonate sediments by unicellular green alga. *Am Miner* 83:1503–1509

- Young, J. R., Ziveri, P., 2000. Calculation of coccolith volume and its use in calibration of carbonate flux estimates. *Deep sea research Part II: Topical studies in oceanography*, 47(9-11), 1679-1700.
- Young, J.R., Bown P.R., Lees J.A., 2017. Nannotax3 website. International Nannoplankton Association.
- Yu, J., J. Day, M. Greaves, Elderfield, H., (2005). Determination of multiple element/calcium ratios in foraminiferal calcite by quadrupole ICP - MS, *Geochem. Geophys. Geosyst.*, 6, Q08P01.
- Zeebe, R. E., Ridgwell, A., and Zachos, J. C., 2016. Anthropogenic carbon release rate unprecedented during the past 66 million years. *Nature Geoscience*, 9 (4), 325-329.
- Ziegenbalg, S.B., Brunner, B., Rouchy, J.M., Birgel, D., Pierre, C., Böttcher, M.E., Caruso, A., Immenhauser, A., Peckmann, J., 2010. Formation of secondary carbonates and native sulphur in sulphate-rich Messinian strata, Sicily. *Sediment. Geol.* 227, 37e50.
- Ziveri, P., Baumann, K.-H., Bockel, B., Bollmann, J., Young, J. R., 2004. Present day coccolithophore biogeography of the Atlantic Ocean. In: Thierstein, H. R., Young, J. R. (Eds.), *Coccolithophores: From Molecular Processes to Global Impact*. Springer Verlag., 529–562.
- Ziveri, P., B. De Bernardi, K.-H. Baumann, H. M. Stoll, and P. G. Mortyn., 2007. Sinking of coccolith carbonate and potential contribution to organic carbon ballasting in the deep ocean. *Deep-Sea Research Part II: Topical studies in oceanography*, 54, 659–675.
- Ziveri, P., Passaro, M., Incarbona, A., Milazzo, M., Rodolfo-Metalpa, R., & Hall-Spencer, J. M., 2014. Decline in coccolithophore diversity and impact on coccolith morphogenesis along a natural CO₂ gradient. *The Biological Bulletin*, 226 (3), 282-290.
- Zondervan, I., 2007. The effects of light, macronutrients, trace metals and CO₂ on the production of calcium carbonate and organic carbon in coccolithophores-a review. *Deep Sea Research Part II*, 54, 521–537.